

**INFN-22-01/GE**

**31 Gennaio 2022**

**TECHNICAL DESIGN REPORT OF THE FalconD Nb<sub>3</sub>Sn  
COS-THETA DIPOLE MODEL FOR THE FCC-hh AT CERN**

Sergio Burioli<sup>1</sup>, Barbara Caiffi<sup>1</sup>, Ernesto De Matteis<sup>2</sup>, Pasquale Fabbriatore<sup>1</sup>,  
Stefania Farinon<sup>1</sup>, Friedrich Lackner<sup>3</sup>, Filippo Levi<sup>2</sup>, Samuele Mariotto<sup>2</sup>,  
Riccardo Musenich<sup>1</sup>, Alessandra Pampaloni<sup>1</sup>, Marco Prioli<sup>2</sup>, Massimo Sorbi<sup>2</sup>,  
Marco Statera<sup>2</sup>, Davide Tommasini<sup>3</sup>, Riccardo Umberto Valente<sup>2</sup>

<sup>1</sup>INFN, Sezione di Genova, Via Dodecaneso 33, I-16146 Genova, Italy

<sup>2</sup>INFN LASA, Viale F.lli Cervi 201, I-20054 Segrate (MI), Italy

<sup>3</sup>CERN, CH-1211 Geneva 23, Switzerland

**Abstract**

Within the European Project EuroCirCol, INFN developed the design of a twin aperture 16 T 4-layer Nb<sub>3</sub>Sn cos-theta dipole for the Future Circular Collider, which was finally chosen as the baseline for the Conceptual Design Report (CDR). In this framework, the Genoa and Milan groups of INFN, in collaboration with CERN under the Addendum No. KE4102/FCC to FCC Memorandum of Understanding FCC-GOV-0004/17.10.2014, are developing a short model which targets a bore field of 12 T, with the possibility of reaching an ultimate field of 14 T, named Falcon Dipole (Future Accelerator post-Lhc Cos $\theta$  Optimized Nb<sub>3</sub>Sn Dipole). As peculiar aspect of the program, already foreseen by the INFN - CERN agreement, the construction of the magnet involves from the beginning industrial partners. INFN has selected ASG Superconductors for this contract, which is now responsible for the construction of the coils. The integration of the magnet in the mechanical structure with the “bladders and keys” technique instead will be carried out at the LASA laboratory in Milan, where a functional test at 4.5 K and 12 T will also be performed. This document, which is the first deliverable of the INFN/CERN collaboration, outlines the main features of the magnet, showing in details the electromagnetic and mechanical design and the quench protection analysis.

*Published by*

*Laboratori Nazionali di Frascati*

## Contents

<b>1</b>	<b>INTRODUCTION</b>	<b>9</b>
<b>2</b>	<b>THE CONDUCTOR</b>	<b>11</b>
2.1	Wire Properties . . . . .	11
2.2	Rutherford Cable . . . . .	13
<b>3</b>	<b>MAGNETIC DESIGN</b>	<b>15</b>
3.1	2D Design . . . . .	15
3.1.1	Coil Geometry . . . . .	15
3.1.2	Iron Yoke . . . . .	16
3.1.3	Magnet Performance at Nominal . . . . .	19
3.1.4	Field Quality . . . . .	24
3.1.5	Field Perturbation: Persistent Current . . . . .	27
3.1.6	Field Perturbation: Random Geometric Errors . . . . .	29
3.2	3D Design . . . . .	34
3.2.1	Coil Ends Geometry Mechanical Optimization . . . . .	34
3.2.2	Return Ends . . . . .	36
3.2.3	Exit Ends . . . . .	37
3.2.4	Layer Jump . . . . .	40
3.2.5	Peak Field . . . . .	42
3.2.6	3D Field Quality . . . . .	44
<b>4</b>	<b>QUENCH PROTECTION ANALYSIS</b>	<b>48</b>
4.1	Simulation Software and Adopted Assumptions . . . . .	49
4.1.1	LEDET . . . . .	49
4.1.2	QLASA . . . . .	50
4.1.3	Comparison between QLASA and LEDET . . . . .	50
4.2	Energy Extraction System . . . . .	53
4.2.1	Parametric Studies of the Dump Resistor and the Activation Time . . . . .	54
4.2.2	Results of the Energy Extraction System Optimization . . . . .	57
<b>5</b>	<b>MECHANICAL DESIGN</b>	<b>58</b>
5.1	2D Finite Element Analysis . . . . .	60
5.2	3D Finite Element Analysis . . . . .	70
5.2.1	Coil material properties . . . . .	74
5.2.2	Magnetic forces . . . . .	75

5.2.3	Longitudinal preloading system . . . . .	77
5.2.4	Results of the 3D mechanical analysis . . . . .	79
<b>6</b>	<b>MAGNET MAIN FEATURES</b>	<b>86</b>
6.1	Turn distribution . . . . .	86
6.2	End spacers . . . . .	89
6.3	Winding . . . . .	89
6.4	Curing . . . . .	89
6.5	Heat treatment . . . . .	89
6.6	Impregnation . . . . .	90
6.7	Assembly of the mechanical structure . . . . .	90
6.7.1	Pad . . . . .	90
6.7.2	Yoke lamination . . . . .	90
6.7.3	Outer shell . . . . .	90
6.7.4	Axial pre-loading system . . . . .	91
<b>7</b>	<b>MOCK-UP ACTIVITY</b>	<b>91</b>
<b>8</b>	<b>References</b>	<b>93</b>

## List of Figures

1	Wire cross-section. . . . .	11
2	Typical sketch of the heat treatment cycle for the reaction of Nb <sub>3</sub> Sn. . . . .	12
3	Definition of the ROXIE parameters for the conductor position. . . . .	16
4	Iron BH-curve used in ROXIE. . . . .	16
5	Relative magnetic permeability at nominal current. . . . .	17
6	2D magnet cross-section. . . . .	18
7	Iron yoke scheme. . . . .	18
8	Iron yoke forces. . . . .	19
9	Falcon Dipole peak field load-line. . . . .	21
10	Parametric study $J_c$ -fit vs. load-line margin. . . . .	22
11	Falcon Dipole 2D field map on coils at nominal. . . . .	22
12	Falcon Dipole 2D field map on coils at ultimate. . . . .	23
13	Fringe field. . . . .	24
14	2D field quality. . . . .	25
15	Correction of the high $b_7$ value. . . . .	27
16	Superconducting magnetization in Falcon Dipole conductors. . . . .	27
17	Harmonics with persistent current. . . . .	28
18	Results of the random geometric error analysis on field quality. . . . .	30
19	Power law fit of the random multipoles. . . . .	33
20	Definition of ROXIE 3D conductor parameters. . . . .	34
21	The inter-turn wedges. . . . .	35
22	Return ends top view. . . . .	36
23	Return ends top yz-section. . . . .	37
24	Exit ends top view. . . . .	39
25	Exit ends yz-section. . . . .	39
26	Layer jump. . . . .	40
27	Hard-way bend conductor in ROXIE. . . . .	41
28	Peak field location in pole turn. . . . .	42
29	Peak field on layer jump. . . . .	43
30	Magnet lengths. . . . .	44
31	3D field quality. . . . .	46
32	Falcon Dipole inductances. . . . .	49
33	LEDET vs QLASA current decay and voltage drop. . . . .	51
34	LEDET vs QLASA Hot-spot temperature and MIITs. . . . .	52
35	NIST, MATPRO and CryoComp comparison. . . . .	53

36	Quench location and energy extraction circuit. . . . .	53
37	Peak inter-filament coupling loss per unit volume during the transient (dump resistor 25 mΩ, nominal current 20930 A). There is no power loss deposited in the block where the quench starts because it is at the resistive state and IFCC cannot occur. . . . .	55
38	Current decay after energy extraction system activation. . . . .	55
39	Hot-spot temperature and voltage to ground after quench. . . . .	56
40	Parametric analysis on maximum activation time. . . . .	57
41	Lorentz forces sketch of FalconD magnet. . . . .	58
42	Layout of the 2D mechanical structure. . . . .	59
43	Scheme of the contacts definition. . . . .	60
44	Finite element model for the 2D analysis. . . . .	61
45	Contact pressure at 12 T. . . . .	62
46	Nodes' Von Mises stress distribution at 12 T. . . . .	63
47	Contact pressure at 14 T. . . . .	63
48	Nodes' Von Mises stress distribution at 14 T. . . . .	64
49	Elements' Von Mises stress distribution at 12 T. . . . .	64
50	Elements' Von Mises stress distribution at 14 T. . . . .	65
51	Displacements in the x direction at 12 T. . . . .	65
52	Displacements in the y direction at 12 T. . . . .	66
53	Displacements in the x direction at 14 T. . . . .	66
54	Displacements in the y direction at 14 T. . . . .	66
55	Root sum square of the displacements at 14 T. . . . .	67
56	Von Mises stress distribution on the wedges at 14 T. . . . .	67
57	Von Mises stress distribution on the pole at 14 T. . . . .	68
58	Von Mises stress distribution on the pad at 14 T. . . . .	68
59	Von Mises stress distribution on the yoke at 14 T. . . . .	69
60	Von Mises stress distribution on the shell at 14 T. . . . .	69
61	Von Mises stress distribution in the cross section at 14 T. . . . .	70
62	Layout of the 3D mechanical structure. . . . .	71
63	Exploded view of the 3D finite element mesh. . . . .	72
64	Views of the 3D finite element model. . . . .	73
65	Schematic representation of the $L_{\perp r}$ , $L_{\perp \theta}$ and $A_{\perp z}$ parameters. . . . .	74
66	Comparison between the Von Mises stress distribution in the 2D and 3D models at 12 T, at assembly. . . . .	81
67	Comparison between the Von Mises stress distribution in the 2D and 3D models at 14 T, at assembly. . . . .	82

68	Comparison between the Von Mises stress distribution in the 2D and 3D models at 12 T, at cool down. . . . .	82
69	Comparison between the Von Mises stress distribution in the 2D and 3D models at 14 T, at cool down. . . . .	83
70	Comparison between the Von Mises stress distribution in the 2D and 3D models at 12 T, at energization. . . . .	83
71	Comparison between the Von Mises stress distribution in the 2D and 3D models at 14 T, at energization. . . . .	84
72	Von Mises stress distribution in the tie-rods at 14 T. . . . .	84
73	Von Mises stress distribution in the flange at 14 T. . . . .	85
74	Von Mises stress distribution in the end plate at 14 T. . . . .	85
75	Von Mises stress distribution in the bullet gauges at 14 T. . . . .	85
76	Turn distribution and conductor details. . . . .	87
77	Coil overall dimensions. . . . .	88
78	Conceptual design of the end spacers. . . . .	89
79	Design of the mock-up of the FalconD bladder&key mechanical system. .	92

## List of Tables

1	Specs of the wire. . . . .	11
2	Expected Rutherford Cable Parameters. . . . .	13
3	Coil parameters. . . . .	15
4	Coil geometry per quadrant with reacted cable. . . . .	16
5	Iron yoke forces. . . . .	19
6	Magnet performance. . . . .	20
7	$J_c$ -fit coefficients. . . . .	20
8	Operational values (from ROXIE output). . . . .	23
9	2D field quality at operation. . . . .	26
10	Field quality at operation with persistent current effect. . . . .	29
11	Random geometric error analysis: definition of random displacement. . . . .	29
12	Results of the random geometric error analysis on field quality. . . . .	32
13	Fitting constants of random multipoles. . . . .	33
14	Inter-turn wedge parameters. . . . .	35
15	Parameters of the return end 3D geometry. . . . .	36
16	Parameters of the exit end 3D geometry: first layer lead side. . . . .	37
17	Parameters of the exit end 3D geometry: first layer opposite to lead. . . . .	38
18	Parameters of the exit end 3D geometry: second layer lead side. . . . .	38
19	Parameters of the exit end 3D geometry: second layer opposite to lead. . . . .	38
20	Hard-way bend conductor parameters used for the layer jump. . . . .	41
21	Peak field in 3D ROXIE model. . . . .	42
22	Falcon Dipole 3D model parameters. . . . .	44
23	3D Field quality at operation. . . . .	45
24	Comparison between QLASA and LEDET computation. . . . .	52
25	Detection system time window. . . . .	54
26	Results of energy extraction system analysis. . . . .	57
27	Mechanical properties of the materials. . . . .	61
28	Average Young and shear moduli of coil's straight part. . . . .	75
29	Average thermal expansion coefficient of coil's straight part. . . . .	75
30	Average Young and thermal expansion coefficient of the coil ends. . . . .	75
31	The Lorentz forces per unit length in the straight part at 12 and 14 T. . . . .	76
32	The Lorentz forces in the straight part and in the coil end at 12 T and 14 T. . . . .	77
33	Comparison between the Lorentz forces computed with OPERA and AN-SYS at 12 T and 14 T. . . . .	77
34	Absolute coil end elongations at 12 T. . . . .	78

35	Absolute coil end elongations at 14 T. . . . .	78
36	Longitudinal reaction forces in magnet components at 12 T. . . . .	79
37	Longitudinal reaction forces in magnet components at 14 T. . . . .	79
38	Average stress in the cross section at 12 T and 14 T at assembly. . . . .	80
39	Average stress in the cross section at 12 T and 14 T at cool down. . . . .	80
40	Average stress in the cross section at 12 T and 14 T at energization. . . . .	80

## 1 INTRODUCTION

The discovery of the Higgs boson at the LHC closes the chapter of the Standard Model and poses new, more puzzling questions that call for building energy- and intensity-frontier colliders. The Future Circular Collider (FCC) study lays the foundations for a new research infrastructure that can succeed the HL-LHC and serve the world-wide physics community for the rest of the 21st century. In January 2019 Conceptual Design Reports (CDR) were issued [1]-[4], describing tantalizingly more powerful particle colliders that can inaugurate the post-LHC era in high-energy physics. Responding to a request from the 2013 Update of the European Strategy for Particle Physics, the Future Circular Collider (FCC) study explores the feasibility of high-performance colliders housed in a new 100 km circumference tunnel.

In the CDR dedicate to FCC hadron Collider, the INFN design of a 16 T Nb<sub>3</sub>Sn superconducting dipole was presented [3]. This magnet is composed by a 4-layers, cosine-theta, double-aperture dipole, responding to the very demanding requirements and challenging aspects for such a high field, high-current density magnet.

To cover the technological gap between actual consolidated Nb<sub>3</sub>Sn superconducting magnet for accelerator, whose bore peak field is in the range of 11 T, and requests for the operation of FCC hadron collider, INFN and CERN have launched a collaboration for developing a model magnet composed by a single aperture, 2-layers, cosine-theta, Nb<sub>3</sub>Sn superconducting dipole, with a operating bore field of 12 T. This project, named FalconD (Future Accelerator post-Lhc Cos $\theta$  Optimized Nb<sub>3</sub>Sn Dipole), is based on four pillars:

- single aperture, 2-layer dipole, with the highest performances allowed by the conductor characteristics
- mechanical structure based on bladder&key system, never attempted in cos-theta dipole magnets
- construction of a significant number of coils (1 dummy coil + 5 Nb<sub>3</sub>Sn coils, to get 1 aperture)
- involvement of the industry since the beginning of the project (ASG Superconductor was selected by INFN through an European tender)

In this document, the Technical Design Report, we are reporting the electromagnetic and mechanical designs, as well as the quench and protection analyses of the FalconD dipole magnet. In particular the sections of the documents are organized as follows:

- Section 2 is dedicated to the description of the Nb<sub>3</sub>Sn conductor and the Rutherford Cable design used for the Falcon Dipole coils;

- Section 3 is dedicated to 2D and 3D magnetic analyses. Several issues are included: magnetic field distribution, geometrical harmonics, harmonics due to persistent currents and coil ends effects on field quality;
- Section 4 deals with quench and protection issues;
- Section 5 deals with the mechanical aspects. Both 2D and 3D finite element analyses have been performed to evaluate stresses and deformations coming out during assembly, cool down and energization.
- Section 6 and 7 shortly reports the cold mass main features and the planned mock-up activity, respectively.

## 2 THE CONDUCTOR

In this section the properties of the conductor used for the Falcon Dipole are described in detail. The first paragraph is dedicated to the wire characteristics and the second one to the Rutherford cable features. The wire is provided by CERN as in-kind contribution and the cable manufacturing will be realized at CERN.

### 2.1 Wire Properties

Table 1: Specs of the RRP Ti-doped Nb<sub>3</sub>Sn wire: ERM-C-1 (162/169) [5].

material	Nb <sub>3</sub> Sn
strand diameter	1 mm
Cu/non-Cu ratio	0.885 ± 0.022
filament diameter	58 μm
filament twist pitch	19 ± 3 mm
RRR, rolled	159 ± 51
heat treatment temperature (50 h)	665°C
$I_c$ at 16 T and 4.22 K	560 ± 14 A

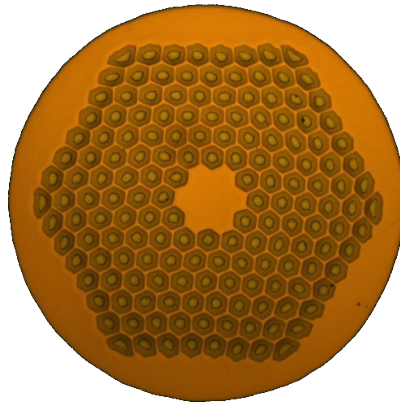


Figure 1: RRP Ti-doped Nb<sub>3</sub>Sn wire: ERM-C-1 (162/169).

The conductor is a RRP Ti-doped Nb<sub>3</sub>Sn wire of 1 mm in diameter with a filament size of 58 μm, which may have important consequences for persistent currents and flux jump instabilities. The Cu/non-Cu ratio of 0.9 is quite low, therefore the RRR of the copper matrix needs to be higher than 150 to prevent thermal instabilities. Preliminary critical current measurements on short samples show high conductive performances,  $I_c = 560$  A at 16 T and 4.22 K which corresponds to  $J_c = 1355$  A/mm<sup>2</sup>. The detailed wire parameters

are reported in Table 1 [5] and in Figure 1 is shown a metallographic image of the strand cross-section.

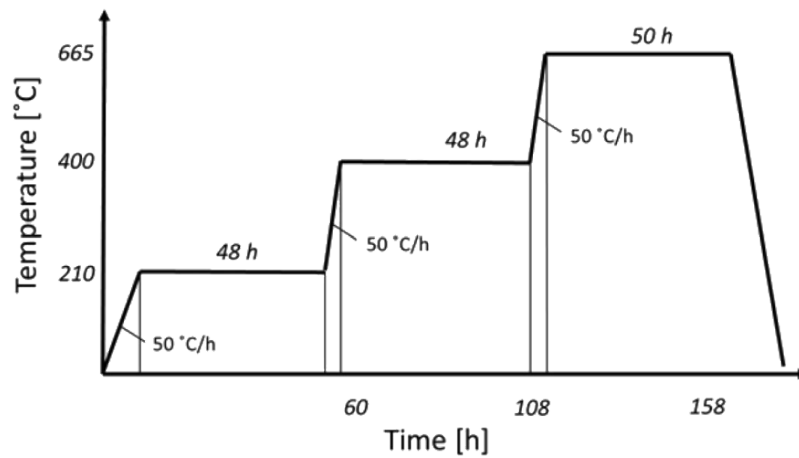


Figure 2: Typical sketch of the heat treatment cycle for the reaction of Nb<sub>3</sub>Sn [6].

It is expected that the conductor will be subject to the isothermal plateau temperature of 665°C during the reaction of the heat treatment cycle. The typical thermal cycle of the heat treatment to form the superconductor is shown in Figure 2, and typically the temperature homogeneity required is within  $\pm 3^\circ\text{C}$  to achieve the required homogeneous performance during the formation of the superconducting phase [6]. The final heat treatment parameters will be agreed on before coil fabrication.

## 2.2 Rutherford Cable

Table 2: Expected Rutherford Cable Parameters.

Parameter	Expected Values
number of strand	40 ( $2 \times 20$ )
keystone angle	$0.5^\circ$
fiberglass insulation thickness	0.15 mm
strand twist pitch	120 mm
bare width (unreacted/reacted)	21.000 mm / 21.420 mm
bare thin edge (unreacted/reacted)	1.720 mm / 1.797 mm
bare mid-thick edge (unreacted/reacted)	1.812 mm / 1.893 mm
bare thick edge (unreacted/reacted)	1.903 mm / 1.989 mm
Nb <sub>3</sub> Sn area	16.53 mm <sup>2</sup> (34.7766%)
Cu area	14.88 mm <sup>2</sup> (33.1516%)
fiberglass insulation area	6.844 mm <sup>2</sup> (15.2461%)
void area	6.629 mm <sup>2</sup> (14.7671%)
tot. area of cable	44.89 mm <sup>2</sup> (100%)
$\theta_{pitch}$ , strand twist pitch angle	$19.29^\circ$
$PF$ , packing factor	0.747
$c_t$ , deformation cable edge	-9.4%
$c_w$ , deformation cable width	-4.2%
$c$ , overall deformation	86.8%
$k_t$ , thin edge compaction (keystoned cable)	91.3%

The Rutherford cable is optimized to reach a bore field of 12 T, but also designed to achieve the ‘ultimate’ field of 14 T. The cable is in production, so the parameters shown are the expected ones. The cable has a twist pitch length of 120 mm and there is a Stainless Steel (SS) foil core of  $16 \text{ mm} \times 25 \text{ } \mu\text{m}$ , which is useful to suppress the inter-strand currents. Knowing that the strand number  $N$  is 40 (2x20), the strand diameter  $d$  is 1 mm and the keystone angle  $\theta$  is  $0.5^\circ$ , the cable dimensions can be evaluated analytically as follow [7]:

$$w = \left(1 + \frac{N}{2}\right) d \quad (1)$$

$$t_i = 2d \cdot 0.86 \quad (2)$$

$$t_o = t_i + w \tan \theta \quad (3)$$

where  $w$  is the bare width,  $t_i$  is the bare thin edge and  $t_o$  the bare thick edge. The fiberglass insulation thickness is expected to be 0.15 mm.

From the CERN, LARP and FNAL experience with the Nb<sub>3</sub>Sn HiLumi magnets [8] [9], the cable size growth due to the heat treatment reaction is taken into account in the

design, in particular for the Falcon Dipole cable the final decision is to suppose the largest size growing possible, which means the one observed in the MQXF quadrupole, i.e. width +2% and mid-thickness +4.5%.

In order to evaluate how the cabling and the winding procedure affect the cable performance, some parameters are evaluated analytically [10]. First of all the cable pitch angle  $\theta_{pitch}$ , which gives information about the mechanical stability and the critical current degradation, is defined as follow from the bare cable width  $w$  and the twist pitch length  $p_c$

$$\tan \theta_{pitch} = \frac{2w}{p_c} \quad (4)$$

and for the Nb<sub>3</sub>Sn cables should be between 12° and 16°. The packing factor (PF), that in general must be greater than  $\pi/4$ , in a range within 84-87% allows to keep under control the critical current degradation and to achieve the adequate mechanical stability that is needed for the coil winding: its definition requires the strand area  $A_{strand}$ , the area of the Stainless Steel core  $A_{core}$ , the total area of the insulated cable  $A_{cable}$  and the pitch angle  $\theta_{pitch}$ :

$$PF = \frac{N A_{strand}}{(A_{cable} - A_{core}) \cos \theta_{pitch}} \quad (5)$$

The deformation of the conductor's cross-section due to the cabling, which affects mainly the damage of the filaments and therefore the critical current limit, can be evaluated with the cable edge compaction  $c_t$  (using the mid-thickness  $t$ ) and the cable width compaction  $c_w$ , that can be combined in the overall compaction  $c$ :

$$c_t = \frac{t}{2d} - 1 \quad (6)$$

$$c_w = \frac{w}{\frac{Nd}{2 \cos \theta_{pitch}} + 0.72d} - 1 \quad (7)$$

$$c = (c_w + 1)(c_t + 1) \quad (8)$$

Moreover the thin edge compaction  $k_t$  can be defined taking into account the keystoneing in the deformation characterization:

$$k_t = \frac{\pi d}{2t_i} \quad (9)$$

Empirically, for Nb<sub>3</sub>Sn it is preferred to be in the following ranges:  $-5\% < c_t < -10\%$ ,  $-3\% < c_w < 0\%$ ,  $80\% < c < 85\%$  and  $95\% < k_t < 103\%$  [11]. See Table 2 for more detailed information.

### 3 MAGNETIC DESIGN

The electromagnetic design of the Falcon Dipole is presented both in 2D and 3D. Unless otherwise specified, the results shown are obtained with ROXIE [12].

#### 3.1 2D Design

##### 3.1.1 Coil Geometry

The Falcon Dipole is a cos-theta dipole with one aperture of 50 mm in diameter. The magnet is designed to reach a bore field of 12 T ('ultimate' field of 14 T) with two layers of keystoneed Rutherford cable wound with the double pancake technique. In each quadrant there are 3 blocks in the first layer and 2 blocks in the second one, for a total of 36 turns. The main goal of the project is to achieve the target field giving priority to the technical feasibility rather than the absolute field quality. Therefore, the minimum bending radius of the cable is set to about 10 mm and the minimum copper wedge dimension is set to 1 mm, in order to avoid cable and insulation damages due to the Nb<sub>3</sub>Sn brittleness during the winding procedure. See Table 3 for further details.

Table 3: Coil Parameters.

Parameter	Value
blocks per quadrant	5
layers	2
turns per quadrant	36
min. bending radius (block 3)	9.845 mm
min. wedge thick. between block 1-2	1.375 mm
min. wedge thick. between block 2-3	1.981 mm
min. wedge thick. between block 4-5	1.171 mm
coil surface per quadrant	1616.04 mm <sup>2</sup>
equivalent coil width (60° sector dipole)	35.92 mm
peak field / bore field	1.044

The coil layout is designed taking into account the cable expansion due to the heat treatment reaction: width +2%, mid-thick +4.5%. The position of each block is defined by the position of its first turn, which is determined by the mandrel radius, the position angle  $\phi$  and the inclination angle  $\alpha$  (see Figure 3). In Table 4 are reported all the parameters of the blocks. The insulation toward ground in the mid-plane is 2x0.15 mm and between the first and the second layer is 0.5 mm.

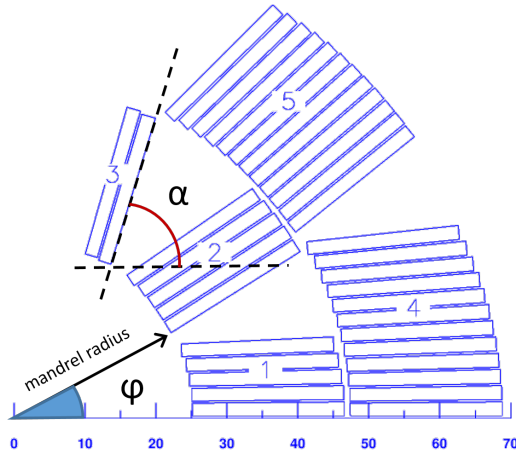


Figure 3: The block position in the cross-section is defined by the first corner of the first turn, whose polar coordinates are the mandrel radius and the positioning angle  $\phi$ . The angle  $\alpha$  defines the inclination of the first turn with respect to the mid-plane.

Table 4: Coil geometry per quadrant with reacted cable.

Block label	Turn number	Mandrel radius	Positioning angle $\phi$	Inclination angle $\alpha$
1	5	25 mm	$0.343771^\circ$	$0^\circ$
2	5	25 mm	$28.1251^\circ$	$31.9888^\circ$
3	2	25 mm	$57^\circ$	$72.9939^\circ$
4	12	47.22 mm	$0.182006^\circ$	$0^\circ$
5	12	47.22 mm	$33.1288^\circ$	$38.7382^\circ$

### 3.1.2 Iron Yoke

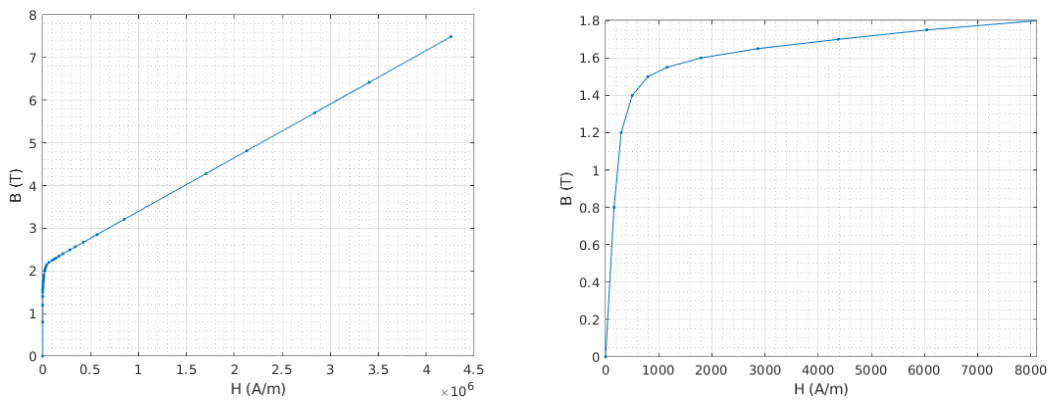


Figure 4: BH-curve used in ROXIE to model the iron yoke of the Falcon Dipole (left). The same plot is zoomed in the region before saturation (right).

The iron used in the BEM-FEM simulation of ROXIE is modelled with the High Luminosity LHC BH-curve [13] (Figure 4) and a packing factor of 0.985

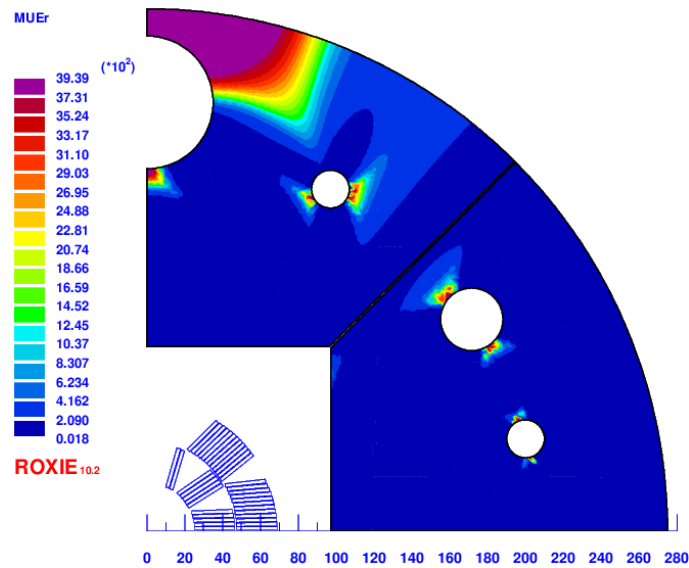


Figure 5: Relative magnetic permeability at nominal current 20991 A, bore field 12 T.

The yoke geometry is designed to make the most of the Bladder & Key technique [14], which allows to give part of the pre-stress at room temperature and the remaining part at cold, in order to keep the stress level on the coils under control. The outer diameter of the yoke is set to 550 mm, to have the possibility to accommodate the magnet (cold mass diameter 640 mm) in the cryostat of the LASA laboratory test station. The level of saturation is very high (Figure 5) and the size and the position of the holes, for the cooling system and the rods to close the magnet axially, don't change the performance significantly, but still there is room to a further refinement.

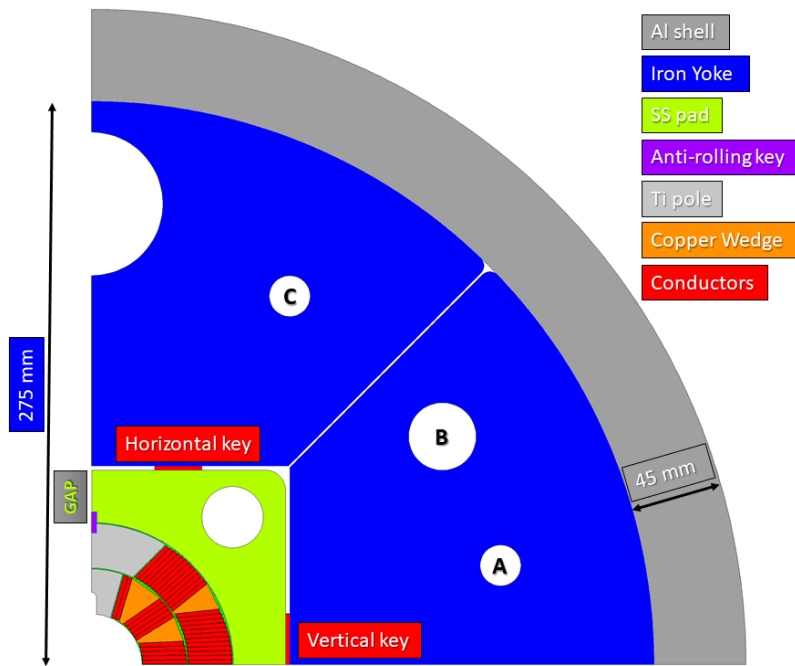


Figure 6: 2D magnet cross-section.

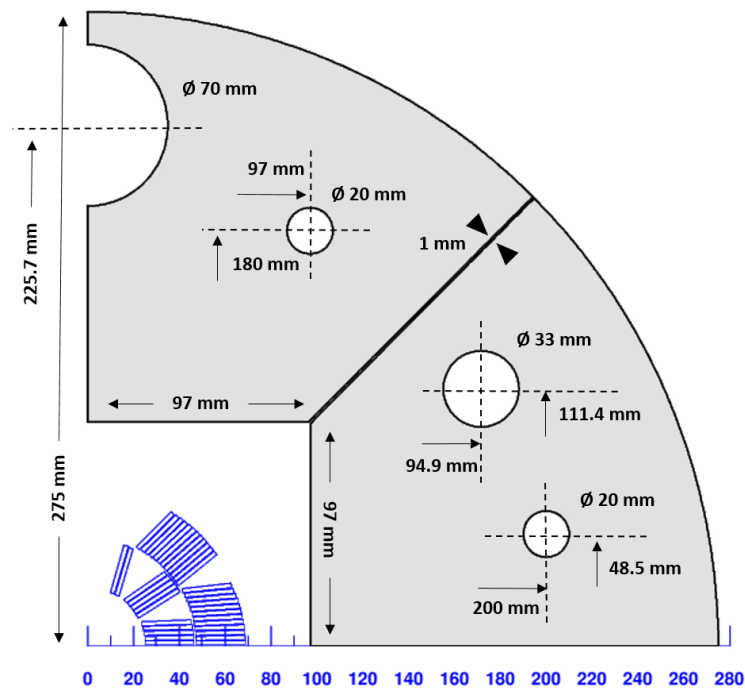


Figure 7: Iron yoke scheme (one quadrant).

The iron yoke consists of four pieces divided by a 1 mm gap inclined at  $45^\circ$ . Each of the four sectors of the iron yoke presents a square window with a side of 97 mm in

which it is host the SS pad. Thank to the 1 mm gap all of the four pieces of the yoke can push on the steel pads independently. See Fig. 6 for the 2D magnet cross section and Fig. 7 for the iron yoke scheme.

During the magnet energization, the four iron sectors are attracted to each other giving a small but not negligible contribution to the coil pre-stress. In particular, the iron sector in correspondence of the mid-plane exerts a horizontal force  $F_x$  that pushes the stainless steel pad horizontally toward the magnet bore, on the other hand the iron sector in correspondence of the pole exerts a vertical force  $F_y$  that pushes the stainless steel pad toward the magnet bore. In Figure 8 the forces scheme is sketched and in Table 5 the simulation results of the force computation are summarized.

Table 5: Iron yoke forces per unit length and per quadrant at bore field of 12 T, computed with different FEM codes [15][16][17].

Software	$F_x$	$F_y$
OPERA 2D	-462.30 N/mm	-234.84 N/mm
ANSYS	-463.11 N/mm	-235.79 N/mm
FEMM	-470.09 N/mm	-239.49 N/mm

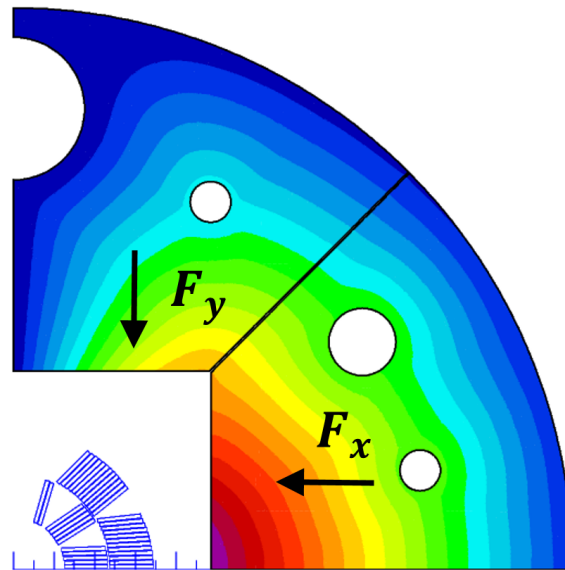


Figure 8: Iron yoke forces scheme per quadrant.

### 3.1.3 Magnet Performance at Nominal

The Falcon Dipole will be tested at CERN in liquid helium at 1.9 K, but a preliminary test at 4.2 K may be performed at the INFN Laboratory of Accelerator and Applied

Superconductivity of Milan (INFN-LASA), where the magnet will be assembled. The short sample values are reported in Table 6.

Table 6: Magnet performance.

Operational temperature	Short sample field	Short sample current
1.9 K	15.59 T	28043 A
4.22 K	14.28 T	25463 A

The operational current is 20991 A and the nominal bore field is 12 T. The load line is computed on the basis of the  $J_c$  dependence on magnetic field and temperature proposed by B. Bordini, with  $t = T/T_{c0}$  and  $b = B_p/B_{c2}(t)$  (see Table 7 for the coefficients)

$$J_c(B, T) = \frac{C(t)}{B_p} b^p (1 - b)^q \quad (10)$$

$$B_{c2}(t) = B_{c2} (1 - t^\nu) \quad (11)$$

$$C(t) = C_0 (1 - t^\nu)^\alpha (1 - t^2)^\alpha \quad (12)$$

Table 7:  $J_c$ -fit coefficients.

$C_0$	$B_{c2}$	$T_{c0}$	$\alpha$	$\nu$	$p$	$q$
$2.14276 \times 10^{11}$ T A/m <sup>2</sup>	29.38 T	16 K	0.96	1.52	0.5	2

where  $C_0 = 2.14276 \times 10^{11}$  T A/m<sup>2</sup> corresponds to  $J_c = 1200$  A/mm<sup>2</sup> at 16 T and 4.2 K, and it is after taking into account the cabling degradation. The degradation due to the cable strain sensitivity is not considered assuming that is negligible if the mechanics is designed to keep the stress on the conductor below the 150 MPa threshold. The margin on the load line is 23.58% at 20991 A and 10.51% at 24906 A (Figure 9).

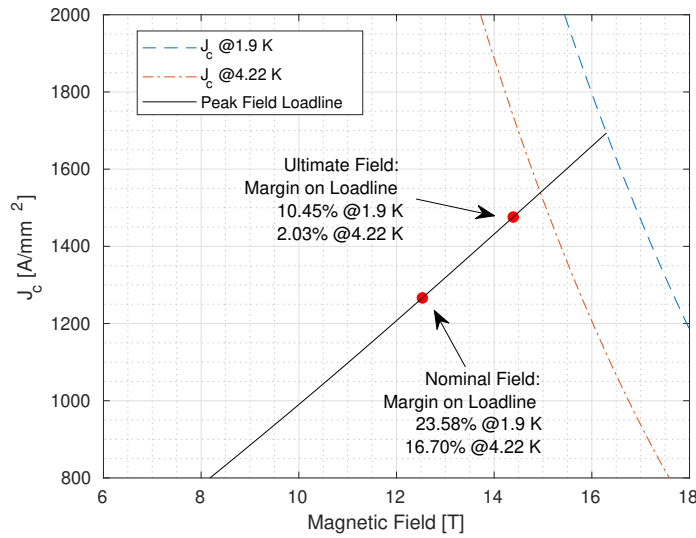


Figure 9: Falcon Dipole peak field load-line vs. the Bordini  $J_c$ -fit at 1.9 K and 4.2 K. The margin on the load-line at nominal bore field 12 T is 23.58% at 1.9 K and 16.70% at 4.2 K. When the magnet is energized at ultimate bore field 14 T, the margin on the load-line is 10.51% at 1.9 K and 2.11% at 4.2 K.

Since the actual cable degradation is unknown until the magnet is tested, a parametric study is performed in order to foresee how the margin is reduced with respect to degradation. The  $J_c$  degradation can be due to different reasons, for example strands damages during cabling, curing and/or winding procedure, but also during operation because of electromagnetic stresses. The critical current density degradation is parameterized scaling the  $C_0$  coefficient of the Bordini's fit (see Table 7) and in Figure 10 (left) the  $J_c$  is plotted with the loadlines of the magnet. The margin on the peak field loadline is reduced to 20% when the degradation is 17.45% (Figure 10, right).

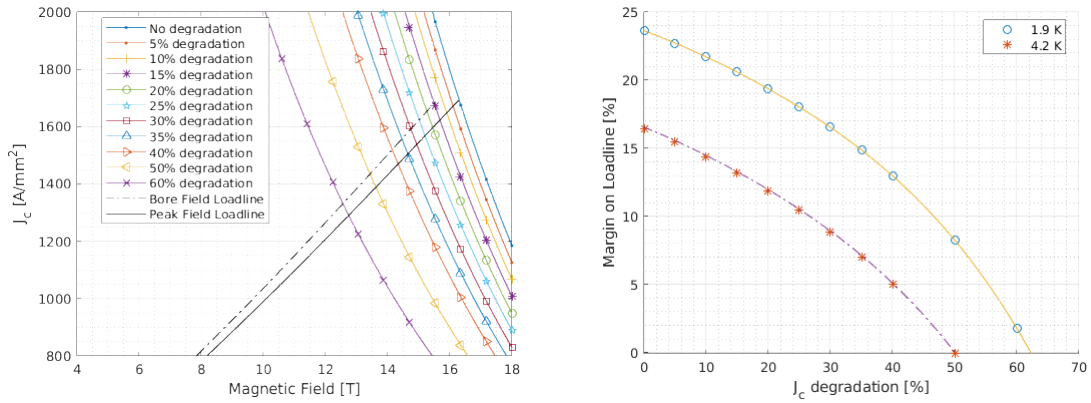


Figure 10: (Left) The critical current density is plotted for different level of degradation with the peak and bore field loadline. (Right) The margin on the peak field loadline as a function of the  $J_c$  degradation is well fitted by the following 4th-order polynomial  $y = -7.361 \times 10^{-7} x^4 + 3.231 \times 10^{-5} x^3 - 0.002531 x^2 - 0.1697 x + 23.63$  when the operational temperature is 1.9 K, on the other and at 4.22 K it is well fitted by  $y = -7.891 \times 10^{-7} x^4 + 3.462 \times 10^{-5} x^3 - 0.002715 x^2 - 0.1824 x + 23.63$ .

The margin computation is performed with ROXIE taking into account the effect of the self-field in the strand. In Figure 11 and Figure 12 are shown the field maps of one quadrant at nominal field of 12 T and ultimate field of 14 T respectively. In Table 8 are indicated all the operational parameters evaluated with ROXIE.

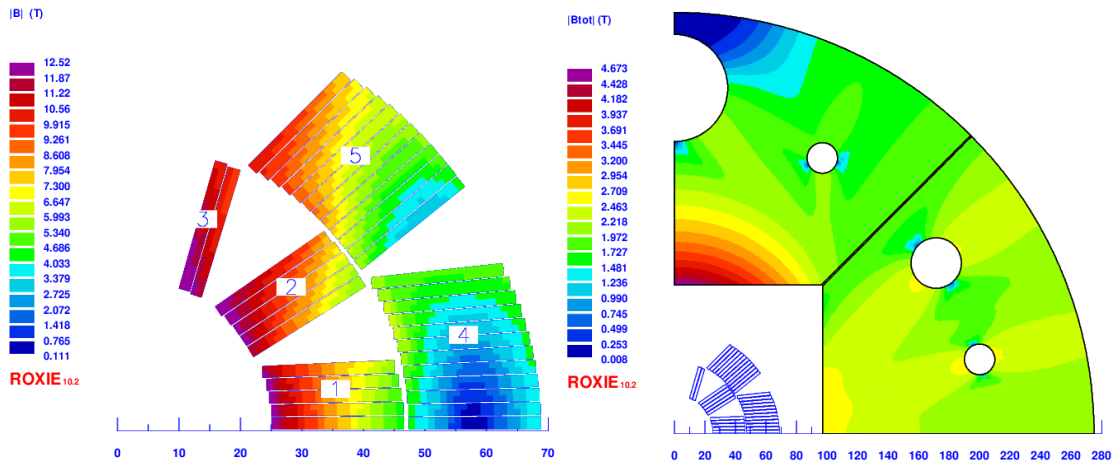


Figure 11: Falcon Dipole 2D field map at nominal current 20991 A of the coils (left) and of the iron yoke (right).

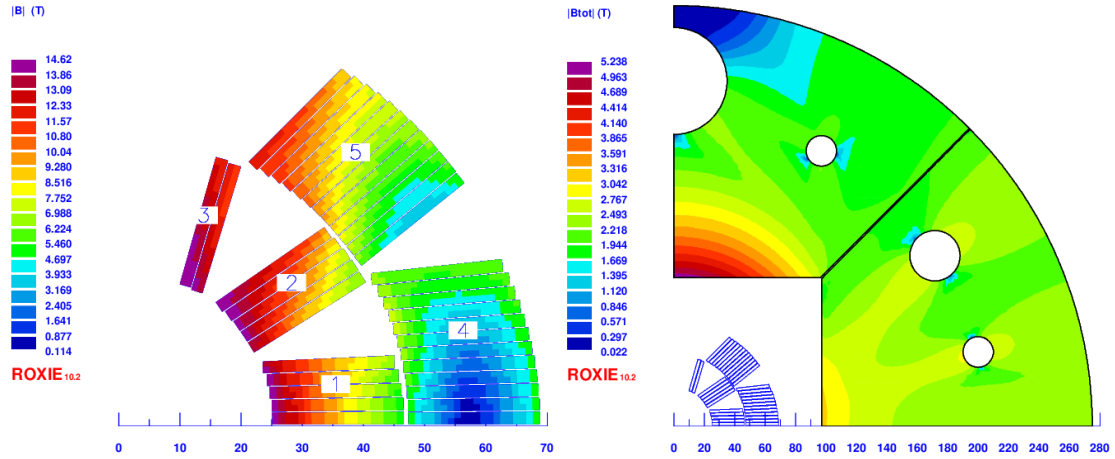


Figure 12: Falcon Dipole 2D field map at ultimate current 24906 A of the coils (left) and of the iron yoke (right).

Table 8: Operational values (from ROXIE output).

Bore field	12 T	14 T
current	20991 A	24906 A
superconductor current density	1269.5 A/mm <sup>2</sup>	1506.3 A/mm <sup>2</sup>
copper current density	1410.6 A/mm <sup>2</sup>	1673.6 A/mm <sup>2</sup>
overall current density	441.4 A/mm <sup>2</sup>	523.8 A/mm <sup>2</sup>
peak field	12.53 T	14.63 T
operating temperature	1.9 K	1.9 K
margin on loadline	23.58%	10.45%
temperature margin	5.11 K	2.72 K
enthalpy margin strand	260.3 mJ/cm <sup>3</sup>	170.3 mJ/cm <sup>3</sup>
enthalpy margin cable	230.6 mJ/cm <sup>3</sup>	156.7 mJ/cm <sup>3</sup>
stored energy	0.54 MJ/m	0.74 MJ/m
differential self inductance	2.23 mH/m	2.19 mH/m
Lorentz forces x per quadrant	3.64 MN/m	4.92 MN/m
Lorentz forces y per quadrant	-1.83 MN/m	-2.58 MN/m

In view of the preliminary test at LASA laboratory, the fringe field produced at the nominal field is evaluated at different distances from the bore with OPERA 2D, in particular just outside the magnet surface of 320 mm, the cryostat surface of 350 mm, and outside the cryostat in the test station zone at 400 mm and 500 mm (Figure 13). In order to have a fringe field below the safety threshold of 0.5 mT (D.lgs. 81/08) the minimum distance should be larger than 1 m, to which the fringe field is 11.37 mT above the bore and 0.01 mT on the mid-plane.

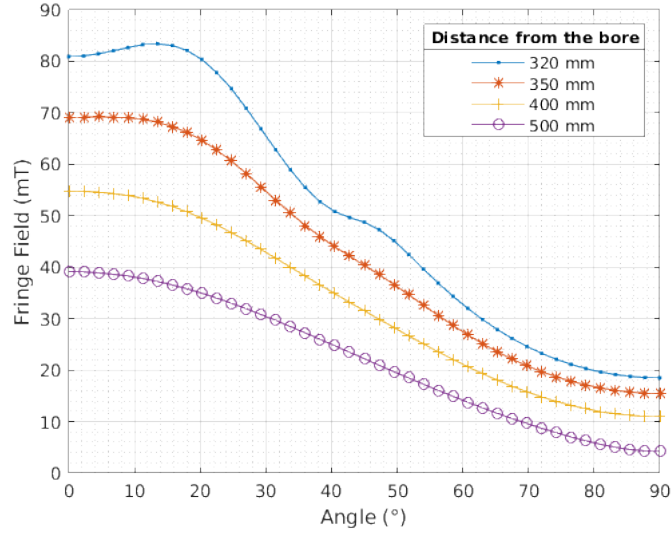


Figure 13: Fringe field evaluated at different distances from the magnet center at the nominal field of 12 T.

### 3.1.4 Field Quality

The field quality is computed with ROXIE assuming the two-dimensional multipolar expansion in European notation

$$B_y(x, y) + iB_x(x, y) = 10^{-4} B_0 \sum_{n=1}^{+\infty} (b_n + ia_n) \frac{(x + iy)^{n-1}}{R_{ref}^{n-1}} \quad (13)$$

The reference radius  $R_{ref}$  is defined to be 16.667 mm, i.e.  $2/3$  of the magnet aperture radius of 25 mm. The expansion is valid locally, i.e. in the bore field aperture, where  $B_0$  is the main harmonic component (dipole value in our case),  $b_1 = 10^4$ , and the other normal  $b_n$  and skew  $a_n$  normalized harmonics are measured in ‘units’ ( $10^{-4}B_0$ ).

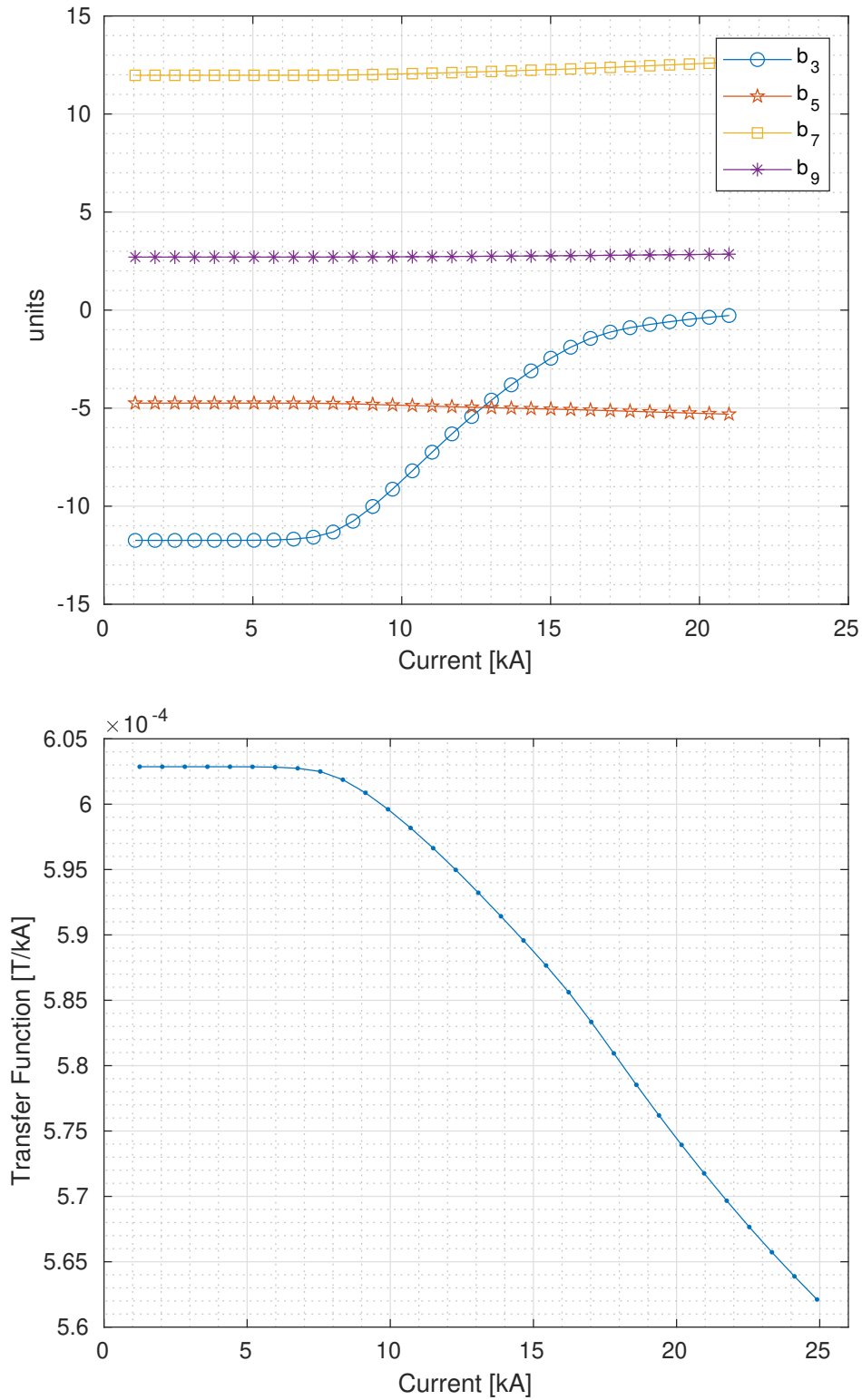


Figure 14: The analysis is performed with ROXIE assuming only the coil geometry and iron saturation effect. (top) 2D harmonics during the current ramping. (bottom) Transfer function.

Table 9: Field quality at operation.

Bore field	12 T	14 T
Operational current	20991 A	24906 A
Reference radius	16.667 mm	16.667 mm
Transfer Function (geometric)	$6.029 \times 10^{-4}$ T/kA	$6.029 \times 10^{-4}$ T/kA
Transfer Function (saturation)	-517.2 units	-676.0 units
$b_3$	-0.28	0.13
$b_5$	-5.30	-5.45
$b_7$	12.63	12.84
$b_9$	2.85	2.90
$b_{11}$	1.31	1.34
$b_{13}$	-0.78	-0.80
$b_{15}$	-0.24	-0.24

In Figure 14 is shown the field quality and the transfer function as a function of the operational current. In Table 9 the harmonic analysis parameters are summarized (the skew harmonics are all zero because of the symmetry). The requirement is not stringent for the harmonics because the field quality is a secondary target with respect to the nominal field. For this reason, not all the harmonics are close to zero at the operating current because of the manufacturing requirements that are imposed to simplify the technical feasibility. However, the field quality can be improved achieving lower performances and making the manufacturing scheme more complex. In particular, the  $b_7$  can be compensated reducing the conductor amount in the region centered at  $360^\circ/m = 360^\circ/7 = 51.7^\circ$  with amplitude  $\pm 360^\circ/4m = 12.9^\circ$ , i.e. between  $38.55^\circ$  and  $64.25^\circ$ , in which the cables give an high contribution to this harmonic (Figure 15, left). For example the  $b_7$  is suppressed dividing the second block of the first layer and re-arranging the coils' number and position, but this solution has been discarded after a feasibility study (Figure 15, right).

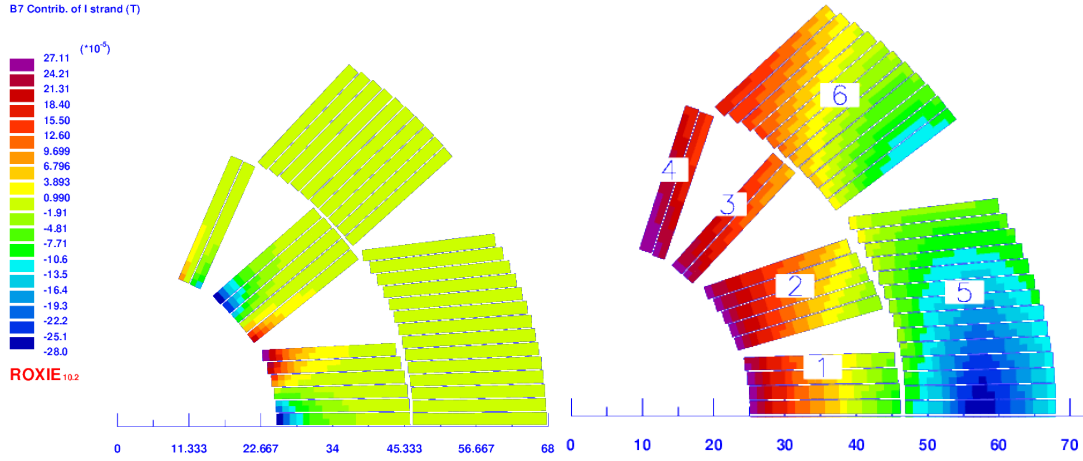


Figure 15: The  $b_7$  contribution of the line currents in the Falcon Dipole cross-section (left). A possible coil layout to suppress  $b_7$  from 12.59 units to 5.63 units, but the minimum bending radius is below 9.4 mm, all the copper wedges have a minimum thickness below 1 mm and the number of turns is increased from 36 to 38.

### 3.1.5 Field Perturbation: Persistent Current

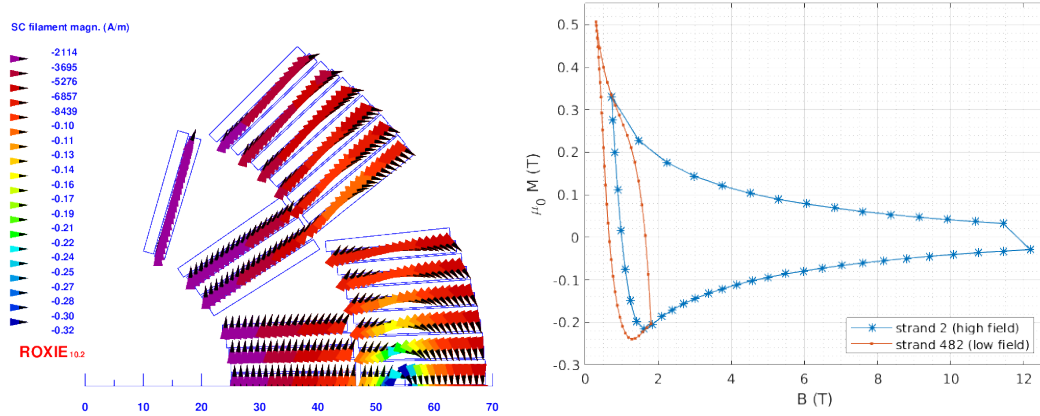


Figure 16: (Left) The distribution of the magnetic dipoles is mapped in the cross-section when the ramp-up of the current ends reaching the higher current value. (Right) The strand magnetization is plotted as a function of the magnetic field applied on the strand using the scalar model of ROXIE [18], with one current cycle ( $5\% I_{nom} \rightarrow 100\% I_{nom} \rightarrow 5\% I_{nom}$ ). The strand 2 and 482 are both in the first turn of the midplane blocks (block 1 and 4, respectively).

During the magnet energization, screening currents arise in the superconductor to oppose the field variation inside the filaments. These currents are persistent as long as the  $Nb_3Sn$  is in the superconducting state and generate magnetic dipoles inside each strand

(Figure 16, left). The strand magnetization is evaluated with the semi-analytical scalar model implemented in the ROXIE code [18]. This strand magnetization strictly depends on the filament size, the superconductor amount and the strand cylindrical geometry. The scalar model intersecting ellipses of  $J_c$  generates a non-linear screening field, which depends on the level of penetration in the strand. When the applied field increases for the first energization, the superconducting material behaves like a perfect diamagnet until the full field penetration is reached, then the screening currents effect reduces and the  $J_c$  dependence on the field dominates decreasing the strand magnetization. When the applied field decreases, the persistent currents' flow changes direction enhancing the magnetic field like a paramagnet. Therefore, the superconducting magnetization due to the persistent currents is a hysteretic phenomenon. In Figure 16 (right) the hysteretic MB-curve is plotted for the Falcon Dipole strand after the second energization.

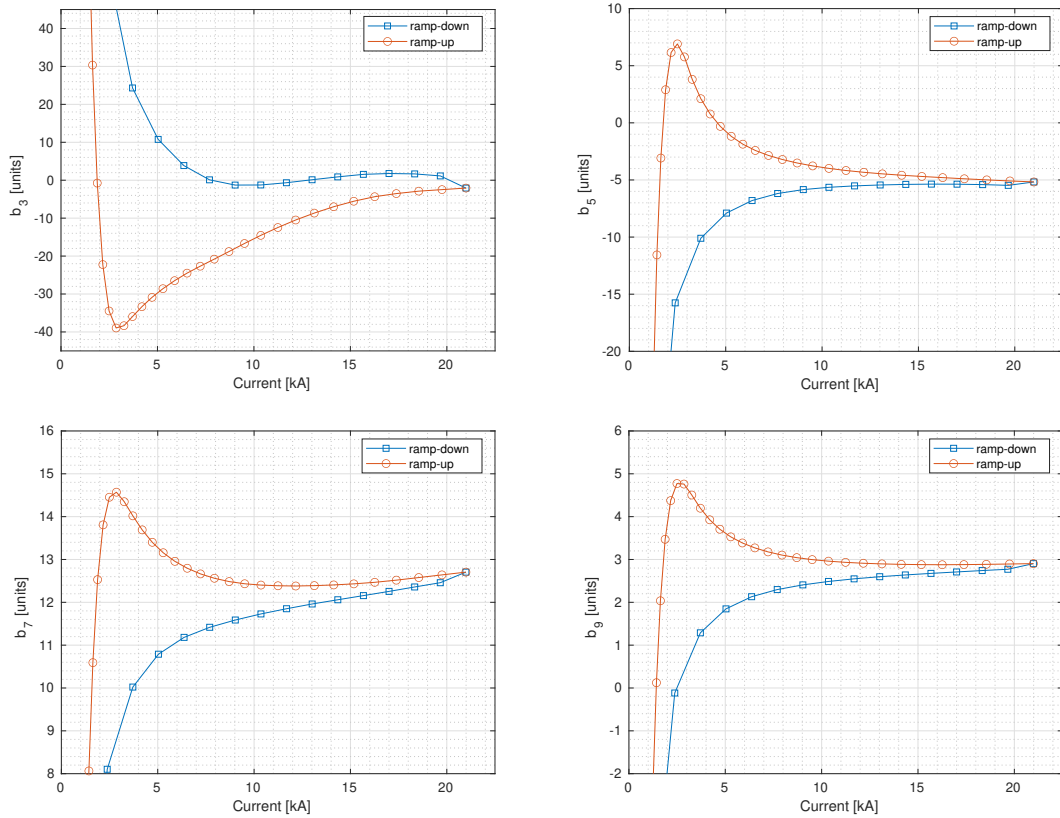


Figure 17: Harmonics with persistent current. Reset current 5% of the operational current.

Table 10: Field quality at operation with persistent current effect.

Parameter	Value
Bore field	12 T
Operational current	20991 A
Reference radius	16.667 mm
Reset current (5% operational current)	1049.6 A
Field rate	0.1 T/s
$b_n$ at operation (increment w.r.t. geo/sat)	units
$b_3$	2.07 (+1.79)
$b_5$	-5.17 (-0.13)
$b_7$	12.70 (+0.07)
$b_9$	2.90 (-0.05)
$b_{11}$	1.31 (-0.00)
$b_{13}$	-0.80 (+0.02)
$b_{15}$	-0.24 (+0.00)

The persistent current effect is evaluated considering the self-field contribution in the strand. The minimum current of the cycle is 1049.6 A (reset current, 5% operational current) and the maximum is the operational current of 20991 A, to reach a bore field of 12 T. The persistent currents affect the field quality at low temperature especially during the ramp-up. The harmonic mainly affected is the  $b_3$  reaching a minimum of about -38 units. Fortunately the field is less perturbed at operation because the superconducting magnetization is lower at higher current. The field quality is analyzed during a current transient for the first allowed harmonics (Figure 17). The field perturbation computed at operational current is reported in Table 10, specifying also the deviation in units with respect to the field quality computed considering the coil geometry and the iron saturation effect only.

### 3.1.6 Field Perturbation: Random Geometric Errors

Table 11: Definition of random displacement with rms  $d$ . The cable width is  $w_{cable}$ .

Degree of freedom	Displacement	Minimum value	Maximum value
Radial position $r$	$\Delta r = d$	$r_{min} = r - \Delta r$	$r_{max} = r + \Delta r$
Positioning angle $\phi$	$\Delta\phi = d/[r + (w_{cable}/2)]$	$\phi_{min} = \phi - \Delta\phi$	$\phi_{max} = \phi + \Delta\phi$
Inclination angle $\alpha$	$\Delta\alpha = 2d/w_{cable}$	$\alpha_{min} = \alpha - \Delta\alpha$	$\alpha_{max} = \alpha + \Delta\alpha$

The field errors due to coils' mispositioning is evaluated in ROXIE with a Monte Carlo simulation on the base of the model shown in [19]. The coil blocks are assumed

to be rigid bodies with three degrees of freedom: the radial displacement  $r$ , the angular displacement  $\phi$  and the coil block rotation  $\alpha$ . Each of these block degrees of freedom have a random displacement with zero average and a rms of  $d/\sqrt{3}$ . The resulting rms amplitude of the coil block is  $\sigma_{tot} = \sqrt{\sigma_r^2 + \sigma_\phi^2 + \sigma_\alpha^2} = d$ . Table 11 summarizes for each degree of freedom the displacement definition and the lower/upper boundaries for a rms coil block displacement of  $d$ .

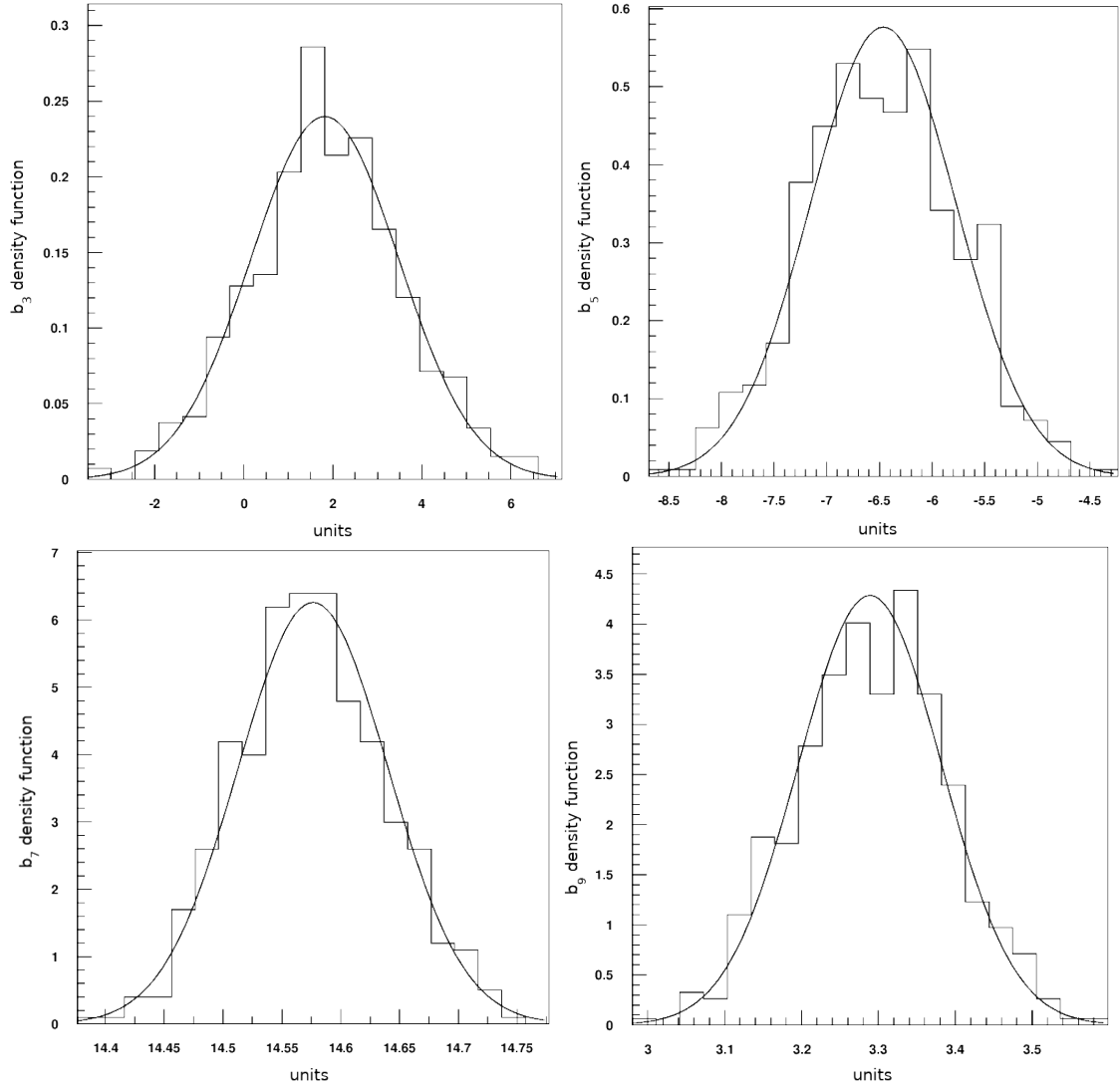


Figure 18: Histograms of 1000 values, normalized for a total surface of 1, and density functions of the  $b_3$ ,  $b_5$ ,  $b_7$  and  $b_9$  field component for 1000 identically distributed random displacements between  $d = \pm 0.05$  mm from the nominal coil-block positions. The harmonics are computed at the reference radius of 16.667 mm at nominal current 20991 A.

Random multipole errors are computed with a sampling technique using 1000 uniformly distributed random errors on the radial position  $r$ , the positioning angle  $\phi$  and the inclination angle  $\alpha$  of each block. The range of these coil-block displacements is  $\pm 0.05$  mm. The multipole analysis after 1000 samples yields a normal distribution function, whose the mean value  $\mu$  and the standard deviation  $\sigma$  are defined as

$$\mu = \frac{1}{1000} \sum_{i=1}^{1000} x_i \quad (14)$$

$$\sigma^2 = \frac{1}{1000} \sum_{i=1}^{1000} (x_i - \mu)^2 \quad (15)$$

where  $x_i$  are the computed relative field components  $b_n$  and  $a_n$  for the  $i$ -th sample. Figure 18 shows for  $b_3$ ,  $b_5$ ,  $b_7$  and  $b_9$  the density function, defined as

$$f(x) = \frac{1}{\sigma\sqrt{2\pi}} e^{-\frac{(x-\mu)^2}{2\sigma^2}} \quad (16)$$

Table 12: Mean and standard deviations for 1000 identically distributed random displacements between  $d = \pm 0.05$  mm relative to the nominal coil-block positions. The sum of the Taguchi loss functions for all the multipoles is 24.9378.

Harmonic	Mean (units)	Standard Deviation (units)
$b_2$	0.0968	1.8992
$b_3$	1.8178	1.6633
$b_4$	0.0669	1.1454
$b_5$	-6.4636	0.6921
$b_6$	0.0154	0.2553
$b_7$	14.5765	0.0637
$b_8$	-0.0055	0.1349
$b_9$	3.2890	0.0931
$b_{10}$	-0.0027	0.0370
$b_{11}$	1.5163	0.0266
$b_{12}$	-0.0004	0.0138
$b_{13}$	-0.9071	0.0058
$b_{14}$	-0.0001	0.0059
$b_{15}$	-0.2774	0.0024
$a_1$	0.0599	2.4660
$a_2$	-0.0069	2.4909
$a_3$	0.0359	1.5973
$a_4$	0.0235	0.9433
$a_5$	-0.0162	0.6864
$a_6$	0.0080	0.5368
$a_7$	-0.0093	0.3594
$a_8$	0.0019	0.1620
$a_9$	-0.0006	0.0800
$a_{10}$	0.0013	0.0572
$a_{11}$	0.0006	0.0281
$a_{12}$	-0.0005	0.0150
$a_{13}$	0.0001	0.0093
$a_{14}$	0.0000	0.0015
$a_{15}$	0.0000	0.0029

All the values computed for both normal and skew harmonics are reported in Table 12. The Taguchi's loss function is defined as

$$L_{a_i, b_i} = k [\sigma_{a_i, b_i}^2 + (\mu_{a_i, b_i} - T_i)^2] \quad (17)$$

where  $T_i$  is the  $i$ -th nominal value and  $k$  is a weighting factor set to 1. The sum computed in the Monte Carlo simulation is  $\sum_i L_{a_i} + L_{b_i} = 24.9378$ .

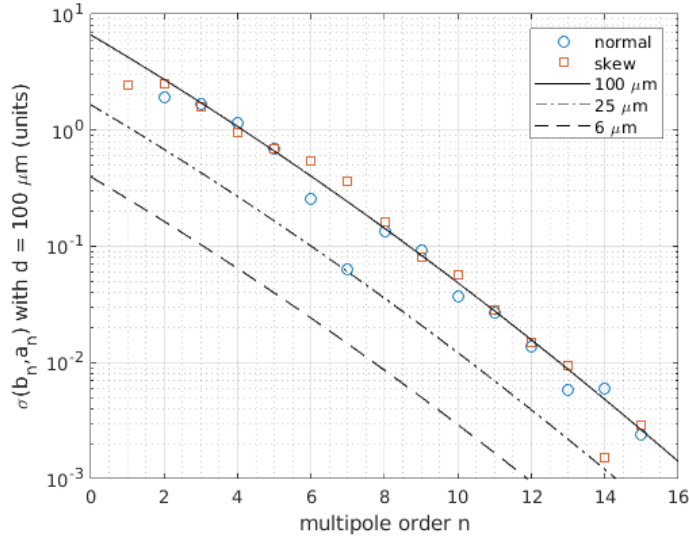


Figure 19: Parabolic fit of the random multipoles due to different random block displacements  $d$ . The numerical estimate is reported only for  $d = 100 \mu\text{m}$ .

Table 13: Fitting constants  $\alpha$ ,  $\beta$  and  $\gamma$  (see Eq. 18) for random multipoles generated by random block displacement for the Falcon Dipole.

$d (\mu\text{m})$	$\alpha (\text{mm}^{-1})$	$\beta$	$\gamma$
100	67.48395	0.64735	0.9942
25	67.06975	0.64915	0.9940
6	63.72045	0.6553	0.9934
Average	66.0914	0.6506	0.9939

The sensitivity analysis of the model is performed also with different values of the random displacement  $d$  in order to determine the rms scaling law fit of the multipoles and therefore provides the constructing tolerances of the coils. The rms of the random multipoles is proportional to the rms amplitude of the block displacement  $d$ , depends on the power law  $\beta^n$  which follows from the Biot-Savart law ( $\beta$  can be roughly estimated with the ratio between the reference radius at which the field quality analysis is performed and the mandrel radius), and finally to the quadratic power law  $\gamma^{n^2}$  that provides a correction to decrease faster the higher order harmonics (it's particularly effective for larger blocks):

$$\sigma_n(d) = d \alpha \beta^n \gamma^{n^2} \quad (18)$$

The fit coefficients for the different analyzed rms amplitudes, and their averages, are summarized in Table 13. Notice that the  $\beta$  constant is very close to the rough estimate

$R_{ref}/R_{aperture} = 16.667 \text{ mm}/25 \text{ mm} = 0.6667$  and  $\gamma < 0$  due to the large cable width. In Figure 19 the standard deviations of  $a_n$  and  $b_n$  for  $d = 100 \mu\text{m}$  are reported, with also the fit described in Eq. 18 and deduced by the averaged constants shown in Table 13.

## 3.2 3D Design

### 3.2.1 Coil Ends Geometry Mechanical Optimization

The coil ends are modelled with ROXIE using the differential-geometry method which is the most suitable for brittle conductors and Rutherford cables with a steel core. The parameters used to optimize the coil geometry are the ellipticity ratio  $f$  and the order of the hyperellipse  $H_{order}$  that defines the baseline of the winding of the inner-most turn on the mandrel, the natural inclination angle  $\beta$  in  $yz$ -plane of the inner-most turn of the block and four cable torsion TORS1-4 along the cable between the apex and the turn end (Figure 20).

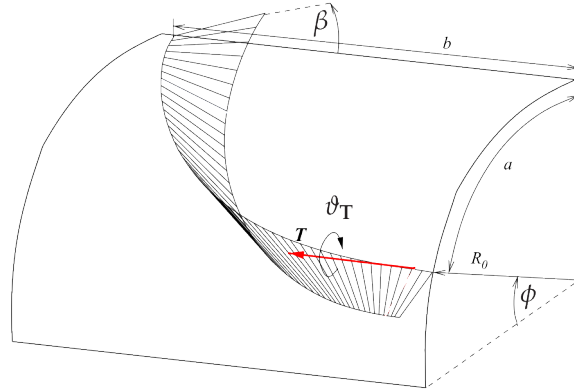


Figure 20: The 3D block is constructed on the basis of the inner-most turn, which follows a baseline on the cylindrical mandrel defined as an hyper-ellipse of the order  $H_{order}$  and ellipticity  $f = b/a$ . The baseline starts from the point defined by the 2D inclination angle  $\phi$  and the mandrel radius  $R_0$ . The natural inclination  $\beta$  is the angle between the  $z$ -axis and the internal surface of the inner-most conductor in the  $yz$ -plane. The additional torsion expressed in radians  $\vartheta_T$  can be defined for four tangent vectors  $T$  along the baseline.

The mechanical optimization is performed with the deterministic Extrem algorithm in order to minimize the maximum normal curvature, the maximum geodesic curvature and the integral of the geodesic curvature squared over the entire block, which is proportional to the strain energy in the block.

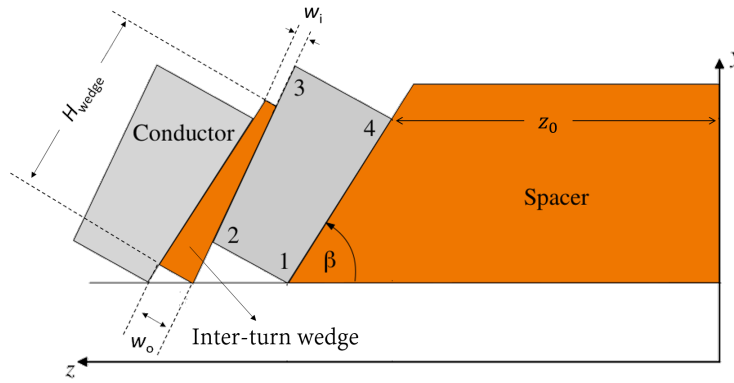


Figure 21: The inter-turn wedges are defined by the height  $H_{wedge}$ , the inner width  $w_i$  and the outer width  $w_o$ .

Table 14: Inter-turn wedge parameters.

$H_{wedge}$	$w_i$	$w_o$
21 mm	0.02 mm	0.2 mm

In ROXIE it is possible to adjust the position of each cable in the winding with virtual inter-turn wedges that compensate the cable keystoneing. They are defined by the height  $H_{wedge}$ , the inner width  $w_i$  and the outer width  $w_o$  (Figure 21). In this first design the inter-turn wedges are the same for each turn and must be investigated after coil winding trials (see Table 14). The  $z_0$  coordinate is defined as the distance between the  $xy$ -plane and the 4th corner of the inner-most cable insulated (Figure 21). The value of this parameter for each block is chosen in order to start the bending of the coil end approximately at the same point, or in other words, to have the same portion of straight part in both the two layers.

The end-spacer geometry is exported from ROXIE to ANSYS to implement some mechanical features to the end-spacers and draw the tooling needed to perform the winding trials. This procedure will be iterate until the final configuration of the end-spacers is obtained.

### 3.2.2 Return Ends

Table 15: Parameters of the return end 3D geometry.

Block number	1	2	3	4	5
$\beta$	74.7392°	75.8339°	72.645°	70°	85°
$f$	3.1029	2.9024	2.9711	2.6	2.45
$z_0$	683.2 mm	640.02 mm	619 mm	705.6 mm	635.26 mm
$H_{order}$	3.9187	4.1836	3.9997	3.8	4
TORS1	-0.015	0	0.4525	0	0
TORS2	0.0386	0	0.7925	0	0
TORS3	-0.1946	0	-1.0629	0	0
TORS4	2.6478	0	-0.8539	0	0

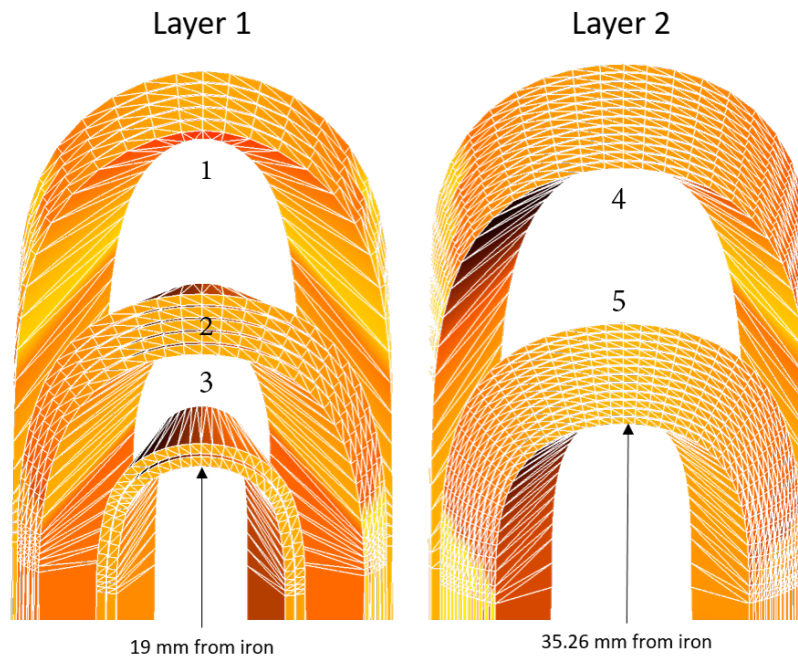


Figure 22: Return ends top view of the first layer (left) and second layer (right).

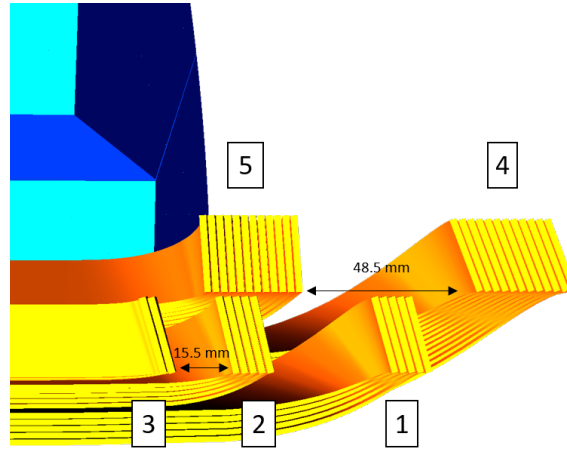


Figure 23: Return ends yz-section.

The main goal is to design the endspacers to make the technical feasibility of the coils as simple as possible. The guideline to be followed is to keep a safe distance between the blocks of conductor to facilitate the endspacers manufacturing and limit the peak field enhancement on the coil ends.

In Table 15 the differential geometry parameters used in ROXIE are reported. The  $z_0$  coordinate is zero in the magnet center, but for the sake of clarity, the relative distance from the iron yoke and the inner-most turn of the first layer pole block is 19 mm and 35.26 mm for the second layer pole block (Figure 22). The minimum thickness of the endspacers is 15.5 between block 2 and 3, and the maximum thickness is 48.5 mm between the block 4 and 5 in the second layer (Figure 23).

### 3.2.3 Exit Ends

Table 16: Parameters of the exit end 3D geometry: first layer lead side.

Block number	1	2	3	4	5
$\beta$	65.0609°	62.1906°	68.8049°	72.2327°	75.1337°
$f$	3.1996	2.9	2.1	2.9	2.4267
$z_0$	704.3 mm	665 mm	629 mm	617 mm	607 mm
$H_{order}$	4.2505	3.6	4	3.5	3.5
TORS1	0	0	0	0.5554	0.5554
TORS2	0	0	0	0.3205	0.3205
TORS3	0	0	0	-0.6406	-0.6406
TORS4	0	0	0	-0.301	-0.301

Table 17: Parameters of the exit end 3D geometry: first layer opposite to lead.

Block number	6	7	8	9	10
$\beta$	65.0609°	62.1906°	68.8049°	72.2327°	75.1337°
$f$	3.8675	2.9	2.75	3.9137	2.3792
$z_0$	704.3 mm	665 mm	629 mm	617 mm	607 mm
$H_{order}$	4.2925	3.9	4	6.4278	3.057
TORS1	0	0	0	-0.3187	0.66
TORS2	0	0	0	-0.1951	0.2626
TORS3	0	0	0	-0.1407	-0.48
TORS4	0	0	0	1.0088	-0.6061

Table 18: Parameters of the exit end 3D geometry: second layer lead side.

Block number	11	12	13	14
$\beta$	59.4174°	60.2458°	73.7024°	72.8039°
$f$	2.0078	2.9026	2.0159	3.5
$z_0$	720.6 mm	700 mm	625 mm	605.15 mm
$H_{order}$	3.81	3.5544	3.9672	5.7
TORS1	-0.3824	-0.4031	-0.5586	-0.015
TORS2	-0.9477	-1.0556	-0.5216	0.0386
TORS3	1.0118	-1.009	2.9639	-0.1946
TORS4	0.7958	0.2248	1.7184	2.6478

Table 19: Parameters of the exit end 3D geometry: second layer opposite to lead.

Block number	15	16	17	18
$\beta$	59.4174°	60.2458°	73.7024°	72.8039°
$f$	3.1457	3.1	2.1504	1.8598
$z_0$	720.6 mm	700 mm	625 mm	605.15 mm
$H_{order}$	3.7653	4.0148	3.8802	3.3362
TORS1	-0.3824	-0.8364	-0.2903	0.4525
TORS2	-0.9477	2.1623	1.0665	0.7925
TORS3	1.0118	9.6372	6.5322	-1.0629
TORS4	0.7958	4.8262	2.1731	-0.8539

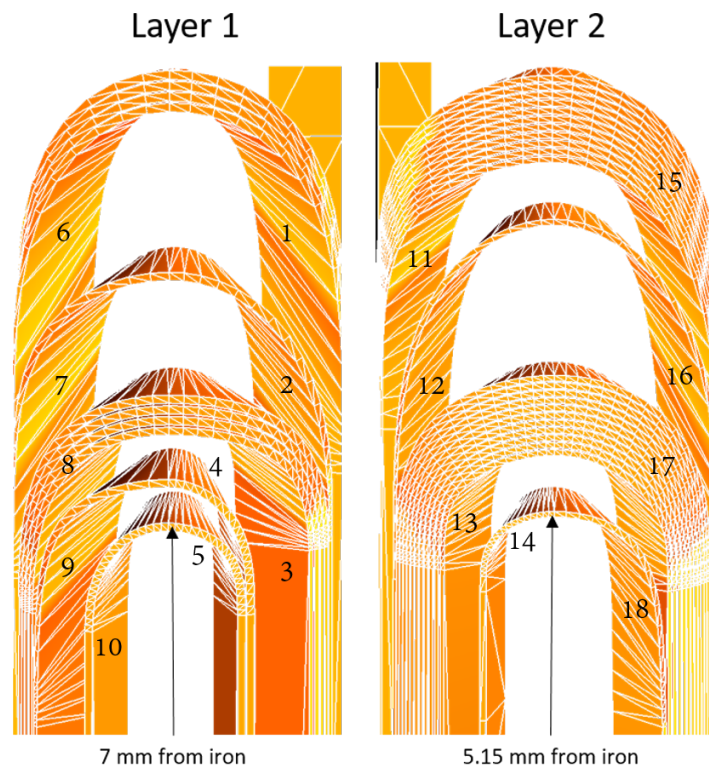


Figure 24: Exit ends top view of the first layer (left) and second layer (right).

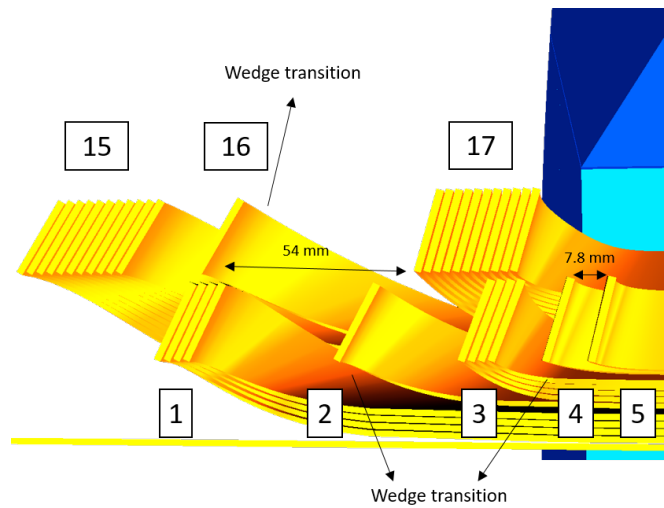


Figure 25: Exit ends yz-section.

In the exit ends there is no symmetry with respect to the y-axis because of the wedge transition between different blocks. For this reason each block geometry is optimized

separately imposing the same  $\beta$  and  $z_0$  for the linked blocks. In Table 16 and Table 17 the differential geometry parameters used in ROXIE for the first layer are reported, and those relating to the second layer are reported in Table 18 and Table 19. Since there is no left-right symmetry, the position of the lead is specified for both layers.

The  $z_0$  coordinate is zero in the magnet center, as with the return end, but in this case the relative distance from the iron yoke and the inner-most turn of the first layer pole block is 7 mm and 5.15 mm for the second layer pole block (Figure 24). The minimum thickness of the end-spacers is 7.8 between block 4 and 5, and the maximum thickness is 54 mm between the block 16 and 17 in the second layer (Figure 25).

### 3.2.4 Layer Jump

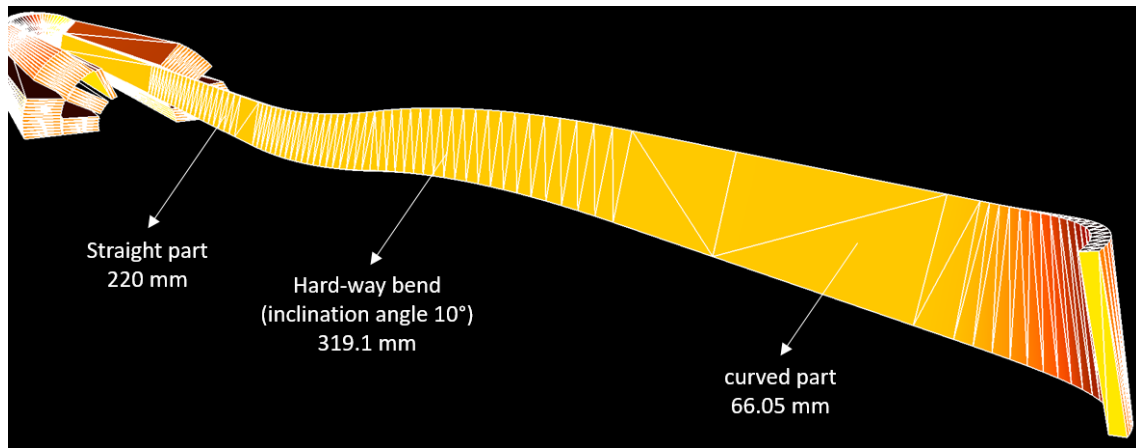


Figure 26: Layer jump.

The layer jump is one of the most critical aspect of the magnet, because the cable here is exposed to the risk of damage in different construction phases. The conductor is modelled using ROXIE with a straight part of 220 mm that starts from the magnet center, then the cable is hard-way bend with curvature radius of 746.1 mm in order to guide the conductor from the first layer to the second one within a distance of 319.1 mm, and finally the cable continues on the path along the second layer with a dummy turn 66.05 mm long (which is the block 18 in Table 19). In Figure 26 it is shown a sketch of the layer jump.

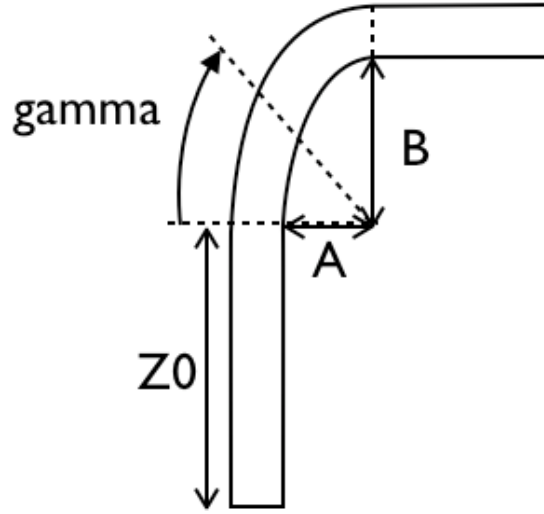


Figure 27: Hard-way bend conductor in ROXIE.

Table 20: Hard-way bend conductor parameters used in ROXIE for the layer jump.

Parameter	Value
$z_0$ [mm]	30
$A$ [mm]	723.6
$B$ [mm]	735.2
$\gamma$ [°]	10

The hard-way bend cable is modelled in ROXIE with a straight conductor  $z_0$  long, followed by a conductor curved on an elliptical trajectory ( $A$  minor semi-axis and  $B$  major semi-axis), truncated at  $\gamma$  angle. The parameters used in ROXIE to model the layer jump are summarized in Table 20. The curvature radius is computed with the following formula:

$$R(\gamma) = \sqrt{\left(A \cos \gamma - \frac{A^2 - B^2}{A} \cos^3 \gamma\right)^2 + \left(B \sin \gamma - \frac{B^2 - A^2}{B} \sin^3 \gamma\right)^2} \quad (19)$$

and in the layer jump center, i.e. when  $\gamma = 10^\circ$ , the curvature radius is 745.9 mm.

### 3.2.5 Peak Field

Table 21: Peak field in 3D ROXIE model.

Location	Peak field
straight part	12.70 T
return ends	12.45 T
exit ends	12.33 T

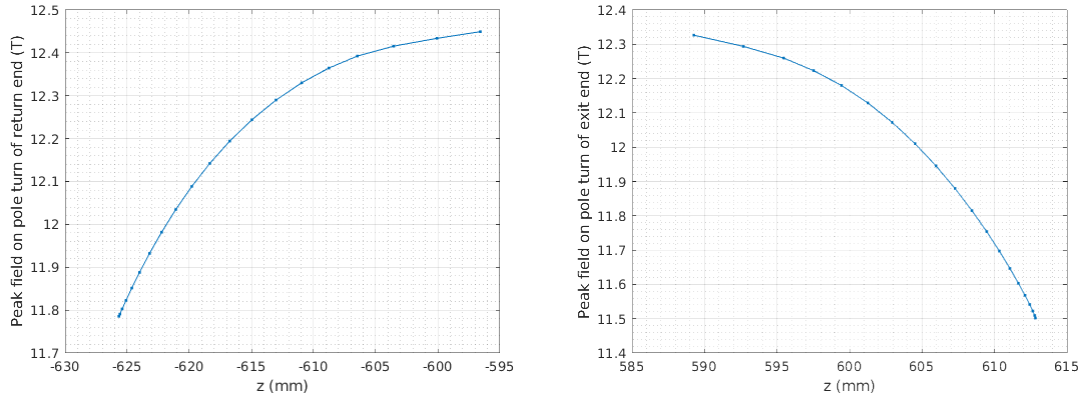


Figure 28: Peak field on the pole turn of the return end (left) and exit end (right).

The field analysis is performed with ROXIE taking into account the self-field in the strands. The whole model of the magnet is simulated with the exit ends in the positive direction of the longitudinal  $z$  coordinate, with the jump layer of the upper pole in the positive direction of the  $x$ -axis.

The peak field computation is focused mainly in the pole turn both in straight section and coil ends. The field in the center of the magnet is enhanced by the coil ends influence, therefore the peak field is 0.17 T higher than the one computed in 2D simulation (12.53 T). The field in the coil ends is evaluated along the strand of the inner-most pole turn (Figure 28) and the peak field is always located where ends the straight section. The peak field in the return end is 0.25 T lower than in the straight section and in the exit end is lower than 0.37 T (see Table 21).

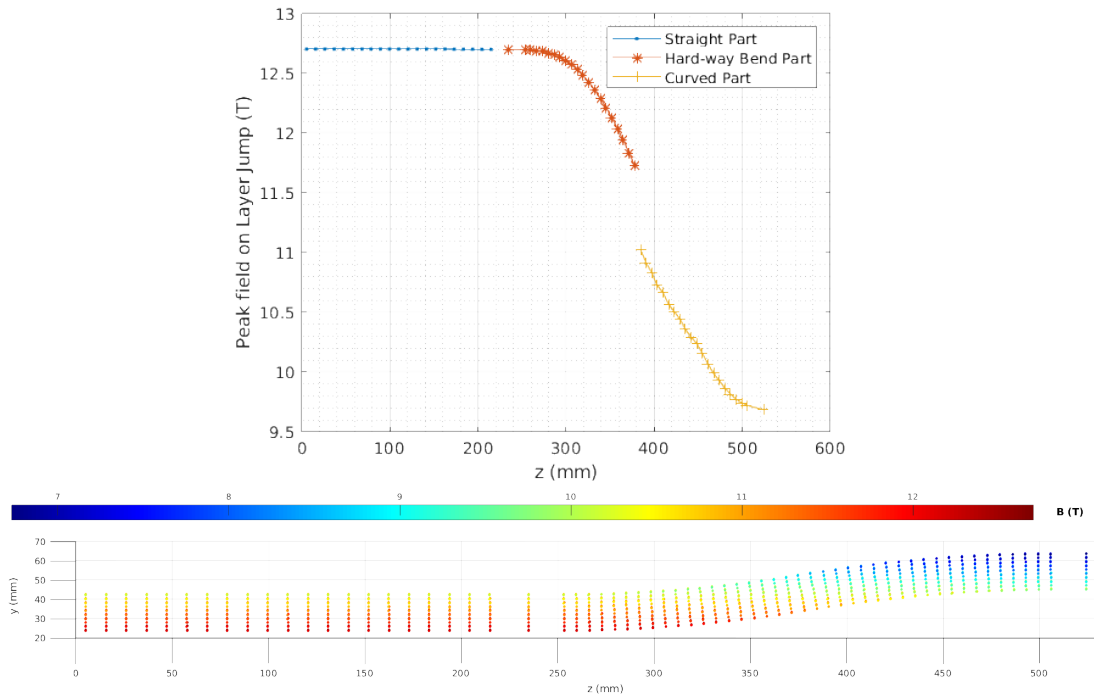


Figure 29: Peak field on the pole turn of the layer jump (top). Field along the layer jump (bottom).

The field in the layer jump is studied in detail because a quench in this region could be very dangerous. The layer jump starts 220 mm from the magnet center in the first layer and the peak field is 12.7 T. The field is still around 12.7 T in the first part of the hard-way bend, between 240 mm and 260 mm, and then it starts to decrease until 11.73 T. The peak field heavily reduced in the curved part of the layer jump because the conductor reaches the second layer. See Figure 29 for the detailed plots.

### 3.2.6 3D Field Quality

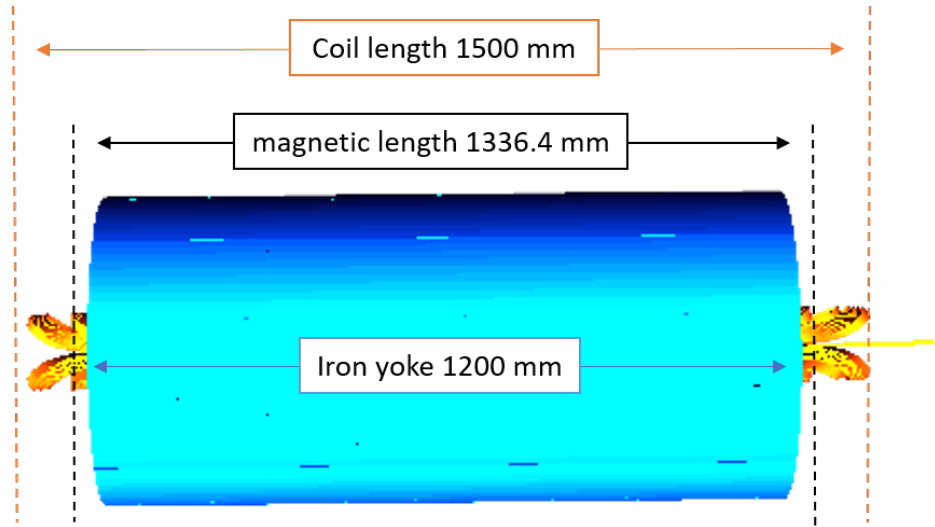


Figure 30: Magnet lengths.

Table 22: Falcon Dipole 3D model parameters.

Parameter	Value
Iron lamination packing factor	0.985
Cable length per pole	102.2 m
Superconductor amount	0.0296 m <sup>3</sup>
Copper amount	0.0329 m <sup>3</sup>
Coil length (end-to-end)	1500 mm
Magnetic length	1336.4 mm
Iron yoke length	1200 mm

The coil length end-to-end, i.e the distance between the most external edge of the cable on each side, is 1.5 m. The amount of cable needed to wind one pole is 102.2 m and therefore CERN provides 150 m of conductor per pole to have a sufficient margin. The simulation is performed using ROXIE with the iron yoke 1.2 m long assuming a packing factor of 0.985 for the lamination. In Figure 30 the magnet lengths are shown and in Table 22 the 3D model parameters are summarized.

The field quality analysis aims to provide the magnetic length  $L_m$  and the normalized 3D harmonics normal  $\bar{b}_n$  and skew  $\bar{a}_n$  integrated along the longitudinal coordinate  $z$  (expressed in units): considering that  $B_0 = 12$  T is the 2D reference field and  $B_1(z)$  is the main field component  $z$ -dependent, they are defined as [20]

$$L_m = \frac{1}{B_0} \int_{-\infty}^{+\infty} B_1(z) dz \quad (20)$$

$$\bar{b}_n = \frac{10^4}{L_m B_0} \int_{-\infty}^{+\infty} B_n(z) dz \quad (21)$$

$$\bar{a}_n = \frac{10^4}{L_m B_0} \int_{-\infty}^{+\infty} A_n(z) dz \quad (22)$$

Table 23: 3D Field quality at operation.

Parameter	Value
Operational current	20991 A
2D reference field	12 T
Reference radius	16.667 mm
Magnetic length	1336.4 mm
Normal integrated harmonic	units
$\bar{b}_3$	18.21
$\bar{b}_5$	-5.17
$\bar{b}_7$	12.01
$\bar{b}_9$	2.85
$\bar{b}_{11}$	1.02
$\bar{b}_{13}$	-0.70
$\bar{b}_{15}$	-0.20
Skew integrated harmonic	units
$\bar{a}_1$	20.04
$\bar{a}_3$	-0.10
$\bar{a}_5$	-0.81
$\bar{a}_7$	1.01
$\bar{a}_9$	-0.16
$\bar{a}_{11}$	0.03
$\bar{a}_{13}$	0.04
$\bar{a}_{15}$	-0.01

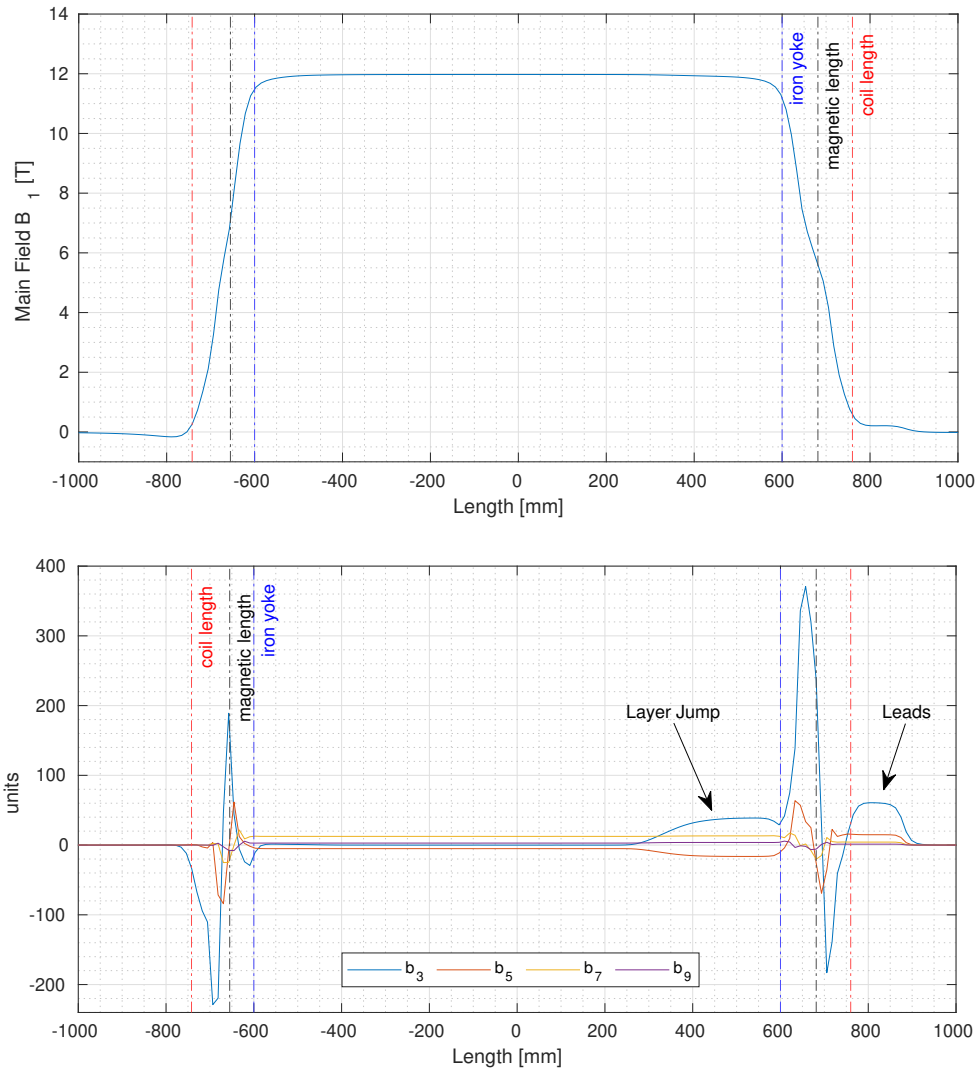


Figure 31: 3D main field  $B_1(z)$  along the magnet length (top). All the other  $b_n(z)$  along the magnet in units (bottom). The operational current is 20991 A (bore field 12 T).

The 3D field harmonics are plotted in Figure 31 as a function of the longitudinal coordinate  $z$ . The field perturbation due to the layer jump and the leads is definitely not negligible, but rather it's clear that there is no chance to effectively compensate them, even because the magnet is too short. The integrated harmonics are reported in Table 23. The integration path should be infinite, but in the simulation it is chosen such that the field is zero at the integration limits. Notice that in the 3D model there is no symmetry with respect to the vertical, horizontal and longitudinal axes because of the layer jump and coil lead end, therefore also the skew integrated harmonics are reported. The not allowed even harmonics (skew and normal) are always below  $10^{-4}$  units, hence they are not reported.

The leads terminates 280 mm from the iron yoke, but this length is chosen arbitrarily in the ROXIE model and could be different in the real magnet.

## 4 QUENCH PROTECTION ANALYSIS

The quench protection study for the Falcon Dipole is presented in this section. The analysis shown is mainly taken from the Andrea Mombelli's Master Thesis 'Study and optimization of the quench protection system for the FalconD magnet, a Nb<sub>3</sub>Sn model dipole for FCC-hh'. The goal of the analysis is to show that after a quench the magnet is discharged safely, limiting the maximum temperature and voltage-to-ground well below the limits of 350 K and 1.2 kV. The simulations are performed on a previous version of the model with a lower nominal and ultimate current, but the results are still valid and very close to the final configuration.

The simulations, performed using accurate multi-physics simulation tools, show that a protection scheme based on an energy extraction system is sufficient to limit the hot spot temperature well below the room temperature (300 K) both at nominal and ultimate current levels. This is an expected result for short model magnets.

Mechanical stress analysis during quench is not performed because the expected temperatures gradients are much lower than the ones calculated for the EuroCirCol 16 T four-layers cos- $\theta$  magnet for which the analysis did not find any potential criticalities [21].

## 4.1 Simulation Software and Adopted Assumptions

### 4.1.1 LEDET

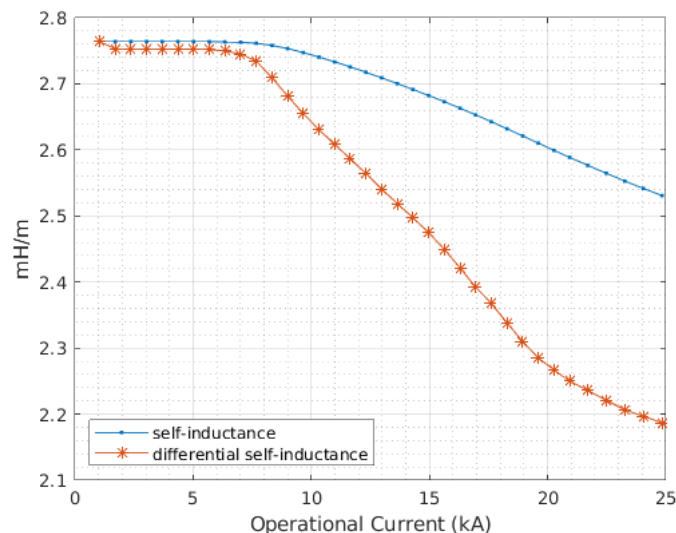


Figure 32: The differential self inductance, which depends on current  $I$ , is defined as  $L_d = L + I \frac{dL}{dI}$ , where  $L$  is the self-inductance, that breaks down in the nonlinear case for iron saturation. In the plot,  $L$  and  $L_d$  during the current transient are evaluated with ROXIE.

The LEDET (Lumped-Element Dynamic Electro-Thermal) [22] software is a tool for computing the transient effects after a magnet quench and the consequent temperature and resistance increase. The thermo-electric properties of the materials are taken from the NIST database [23]. The output of the simulation is the current decay profile, final temperature distribution, hot-spot temperature and the voltages in the windings. Inputs to the code are:

- Magnet and cable parameters (see Table 2 and Table 8);
- Magnetic field map (from ROXIE, see Figure 11 and Figure 12);
- Mutual inductance matrix (from ROXIE);
- Differential inductance vs. magnet current (from ROXIE, see Figure 32);
- Characteristic of the protection system circuit.

The LEDET code simulates the magnet at the strand level, importing the geometry from ROXIE, and the current discharge can be calculated taking into account the inter-filament coupling currents (IFCC) and the inter-strand coupling currents (ISCC). The heat transfer between cables is also computed during the transient simulation.

#### 4.1.2 QLASA

The QLASA [24] code is optimized to simulate the behaviour of solenoids after a quench with a semi-analytic approach. After a dedicated geometry transformation, it can be also applied to cos-theta magnets. The thermo-electric properties of the materials are taken from the MATPRO database [25]. Inputs to the code are:

- Coil geometry must be adapted to equivalent solenoids: a coils' block of a cos-theta dipole with  $N$  turns of width  $w$  and mid-thickness  $h$ , and longitudinal length  $L$ , can be transformed in an equivalent solenoid with inner radius  $R_{in}$ , outer radius  $R_{out}$  and height  $H$ , assuming the volume conservation [26]:

$$R_{in} = \frac{L}{\pi} - \frac{2}{w} \quad , \quad R_{out} = R_{in} + w \quad , \quad H = N h \quad (23)$$

- Magnetic field map (from ROXIE) is linearized starting from the field value at the solenoid corners;
- Differential inductance vs. magnet current (from ROXIE, see Figure 32);
- Characteristic of the protection system circuit.

The IFCC and ISCC effects on the discharge are not computed by QLASA and the heat transfer between the equivalent solenoids is not automatically simulated. The first instants after a quench are accurately simulated via analytic computations of the 3D ellipsoidal growth of the normal zone.

#### 4.1.3 Comparison between QLASA and LEDET

The comparison between QLASA and LEDET is performed starting from the same modelling assumptions:

- Inter-filament and inter-strand coupling losses are not taken into account in LEDET, because QLASA is not able to compute dynamic effects;
- The transverse heat propagation between blocks is suppressed in LEDET as it happens with QLASA;

- The quench starts in the same peak field region (Figure 36);
- The longitudinal propagation of the quench is analytically computed by QLASA, on the other hand in LEDET the quench propagates instantaneously along the magnet, i.e. infinite velocity. Therefore, in the simulations named LEDET 2D+1D it is imposed a finite longitudinal velocity, computed with QLASA, in order to reproduce a 2D+1D propagation;
- The dump resistor value is  $25 \text{ m}\Omega$  and the activation time is 30 ms, with a voltage threshold of 100 mV;
- The operational current is 20930 A (nominal current).

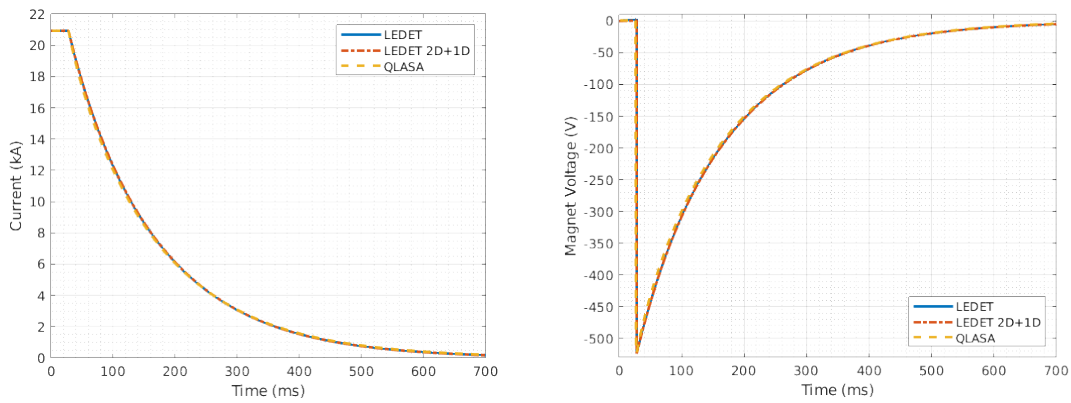


Figure 33: The current decay (left) and the magnet voltage drop (right) are evaluated with different software neglecting the IFCC effect.

The computations of the current and voltage after the energy extraction system activation are in good agreement and give confidence to the adopted simulation approaches (Figure 33). The discrepancy between the simulations performed with LEDET considering or not the longitudinal quench propagation is negligible.

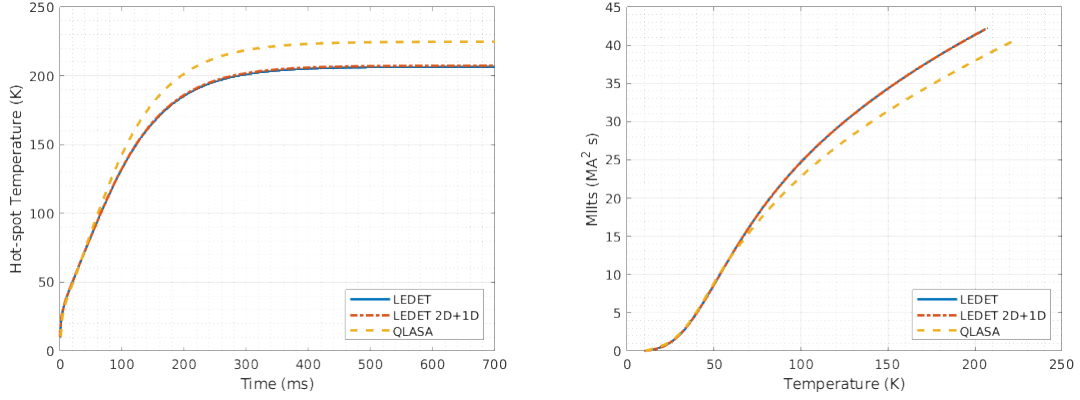


Figure 34: The hot-spot temperature (left) and the MIITs (right) are evaluated with different software neglecting the IFCC effect. The discrepancy between QLASA and LEDET is due to the different material libraries adopted in the computation. In general, QLASA leads to more conservative results than LEDET.

The difference between the two software is more evident in the hot-spot temperature and MIITs plots (Figure 34), and the reason is that QLASA and LEDET use different material libraries, MATPRO and NIST respectively. In fact, the MIITs, and consequently the hot-spot temperature, are strongly dependent on material properties, and in particular on the heat capacitance  $C_p(T)$ , the resistivity  $\rho(T)$  and the density  $\rho$  (see Table 24). Following the Maddock and James's technique (1968), i.e. heat balance in adiabatic approximation, the integral  $U(T_{hot-spot})$  is

$$U(T_{hot-spot}) = \int_0^\infty J^2(t) dt = \int_{T_{operation}}^{T_{hot-spot}} \frac{\gamma C_p(T)}{\rho(T)} dT \quad (24)$$

Table 24: Comparison between QLASA and LEDET computation.

Software	Hot-spot temperature (K)	MIITs ( $10^6 A^2 s$ )
QLASA	224	40.9
LEDET	209	41.9
LEDET (2D+1D)	210	42.1

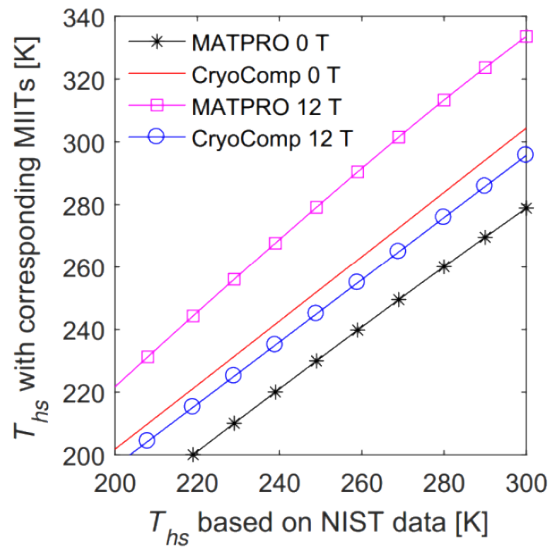


Figure 35: Hot-spot temperature comparison between NIST, MAPRO and CryoComp material libraries [28].

The discrepancy between the material libraries is already known [27,28] (Figure 35) and provides an estimation of the expected model uncertainty whose maximum value is  $\pm 20$  K.

#### 4.2 Energy Extraction System

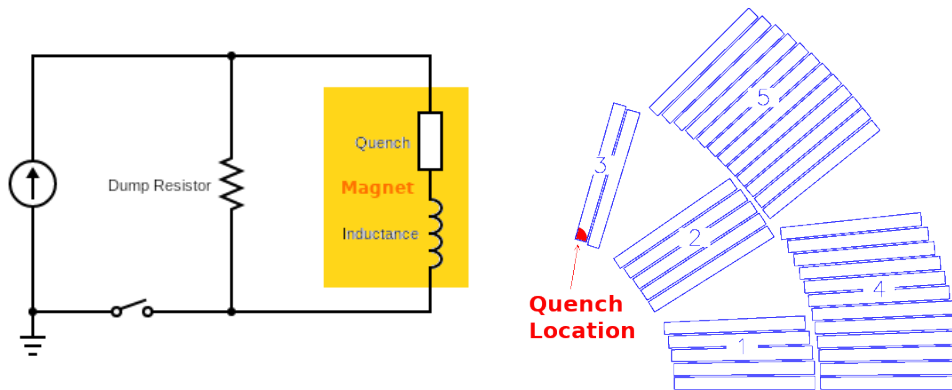


Figure 36: (Left) Sketch of the energy extraction circuit: when the quench is detected and validated the current is by-passed through the dump resistor in order to dissipate the stored energy of the magnet. (Right) The quench is supposed to start in the peak field location, where the enthalpy margin is lower.

The initial hypothesis is that a point-like quench starts in the peak field region (Fig 36, right) and propagates in the transverse direction with a finite velocity which locally depends on the magnetic field, temperature and critical current in each time-step. On the other hand, the longitudinal propagation is reasonably assumed instantaneous since the magnet is short, unless stated otherwise.

The activation time  $t_a$  of the protection system is defined as the sum of the detection, the validation and the switch opening times. The detection  $t_d$  is the time between when the resistive voltage starts to increase due to the quench and when it reaches the voltage threshold, which is set to 100 mV: the result of the QLASA computation is 8 ms. The validation  $t_v$  is defined as the maximum duration for the resistive voltage above the threshold 100 mV and it is set a priori to 20 ms. The trigger  $t_t$  is the time needed to switch-off the power supply and the typical values are 2 ms for solid-state electronic switch and tens of ms for electro-mechanical switch.

When a quench starts to propagate the resistive voltage across the magnet increase up to a point at which the quench is detected and validated by the protection system and the energy extraction system is activated in order to dissipate the stored energy in the dump resistor and reduce the hot-spot temperature in the magnet (Fig 36, left). The ground is located in one of the magnet leads for all the simulations, but it can be placed in the middle of the dump resistor to halve the ground voltage during the discharge.

#### 4.2.1 Parametric Studies of the Dump Resistor and the Activation Time

When the protection system is activated, the peak voltage toward ground  $U_{max}$  is determined by the current  $I_o$  flowing in the dump resistor  $R_{dump}$ . Since the requirement is  $U_{max} < 1.2$  kV, the dump resistor is limited to:

$$R_{dump} < \frac{U_{max}}{I_o} \quad (25)$$

Therefore when the magnet is energized at the nominal current (20930 A) the dump resistor should be less than 57 m $\Omega$  and at the ultimate current (24838 A) less than 48 m $\Omega$ .

Table 25: Detection system time window.

Time	Value
detection (from QLASA), $t_d$	8 ms
validation (threshold 100 mV), $t_v$	20 ms
switch trigger, $t_t$	2 ms
activation, $t_a = t_d + t_v + t_t$	30 ms

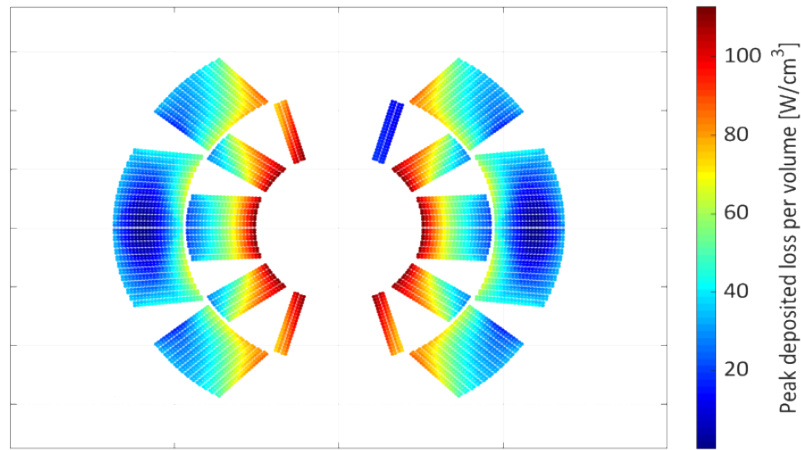


Figure 37: Peak inter-filament coupling loss per unit volume during the transient (dump resistor  $25\text{ m}\Omega$ , nominal current  $20930\text{ A}$ ). There is no power loss deposited in the block where the quench starts because it is at the resistive state and IFCC cannot occur.

A parametric study is performed with LEDET to determine the current discharge of the magnet and the hot-spot temperature (with adiabatic conditions) as a function of the dump resistor. The activation time for all the simulations is set to  $30\text{ ms}$  (see Table 25 for more details). During the transient the computation takes into account the effect of the IFCC, which deposit power losses mainly in the inner layer of the Falcon Dipole and help the magnet to discharge faster (Figure 37).

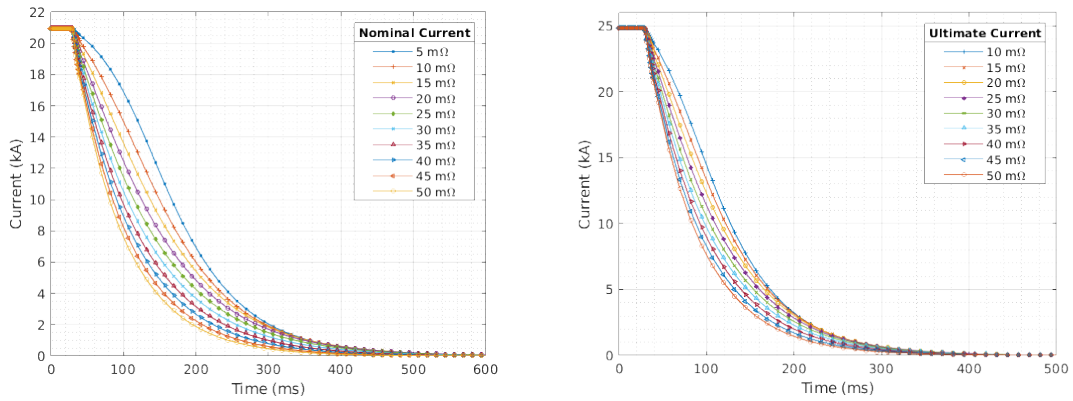


Figure 38: The magnet is safely discharged both at the nominal current of  $20930\text{ A}$  (left) and at the ultimate current of  $24838\text{ A}$  (right). The current decay follow approximately the exponential law for  $R_{quench} \ll R_{dump}$  and therefore the higher  $R_{dump}$ , the faster the magnet discharge.

The magnet is safely discharged both at nominal and at ultimate current, and as expected the higher the dump resistor, the faster the current decay (Figure 38).

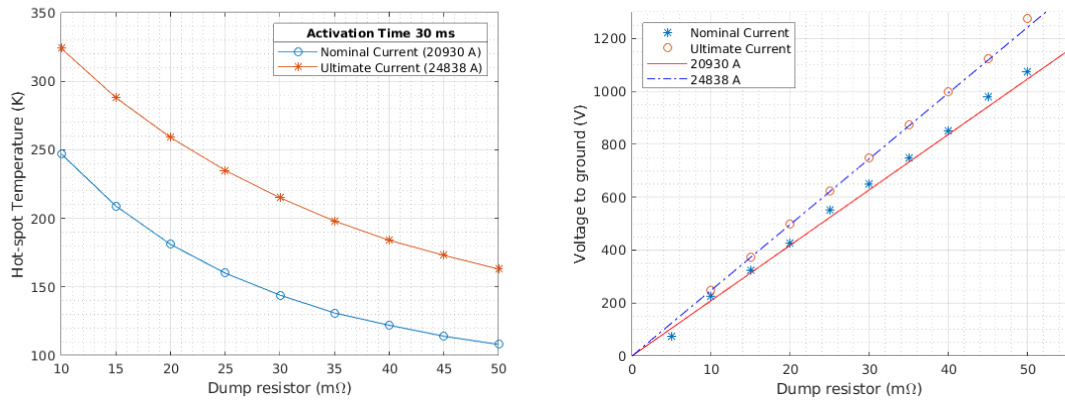


Figure 39: (Left) The hot-spot temperature for nominal and ultimate current is plotted as a function of the dump resistor. (Right) The voltage to ground is mainly determined by the dump resistor  $U_{max} \simeq R_{dump} I_o$ , because its value is higher than the resistive contribution of the quench and the other dissipative phenomena during the transient.

The energy extraction system allows to keep always the hot-spot temperature below the limit of 350 K, and, as shown in Figure 39 (left), a higher dump resistor allows to decrease significantly the hot-spot temperature. On the other hand, there is a limit on the resistance value imposed by the voltage to ground (Figure 39, right).

Another useful parametric study is the one to determine the maximum activation time  $t_a$  to reach the conservative limit of 350 K considering different dump resistor values (Figure 40). If the maximum voltage to ground is fixed to 1.2 kV, at nominal current the resulting dump resistor value is 57 mΩ that leads to a maximum activation time of 107 ms. At ultimate current, the dump resistor value for 1.2 kV is 48 mΩ that leads to a maximum activation time of 68 ms. These are the upper boundaries of the allowed time delays.

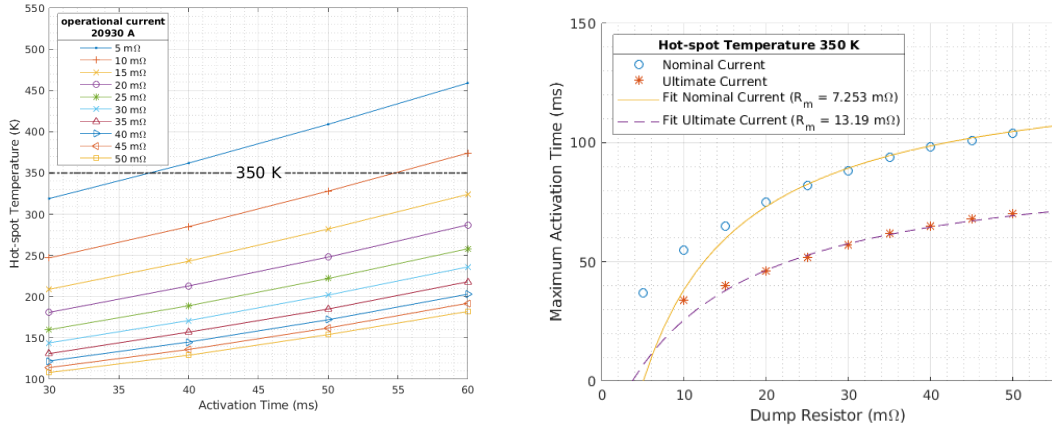


Figure 40: (Left) The hot-spot temperature is evaluated for different activation time of the energy extraction system at nominal current. (Right) Maximum activation time to reach 350 K plotted as a function of the dump resistor at nominal current 20930 A (bore field 12 T) and at ultimate current (bore field 14 T).

#### 4.2.2 Results of the Energy Extraction System Optimization

Table 26: Results of a feasible solution for the energy extraction system:  $R_{dump} = 25 \text{ m}\Omega$ ,  $t_a = 30 \text{ ms}$ .

Parameter	Nominal current 20930 A	Ultimate current 24838 A
Dump resistor	25 mΩ	25 mΩ
Activation time	30 ms	30 ms
Hot-spot temperature	160 K	235 K
Max. voltage to ground	525 V	625 V
Max. voltage between layer	263 V	313 V
Max. voltage between turns	10 V	14 V

From the parametric study results that the Falcon Dipole is easily protected with the energy extraction system. The best range for the dump resistor is  $20 \text{ m}\Omega < R_{dump} < 35 \text{ m}\Omega$ , when the activation time is set to 30 ms. The ground is located at the end of the winding, therefore the peak voltages can be halved with a symmetric grounding in the middle of the dump resistor. The hot-spot temperature and the peak voltages computed for this configuration are summarized in Table 26.

## 5 MECHANICAL DESIGN

The mechanical structure of the Falcon Dipole has to be designed in such a way to withstand the huge Lorentz forces which arise once the magnet is energized up to the nominal field of 12 T and the ultimate field of 14 T. The Lorentz forces acting on the magnet, calculated through the ANSYS model described in Section 5.1, are schematized in Figure 41. The horizontal and vertical resultants of each half coil are  $F_{tot,x} = 3575$  kN/m and  $F_{tot,y} = -1781$  kN/m at 12 T and  $F_{tot,x} = 4821$  kN/m and  $F_{tot,y} = -2509$  kN/m at 14 T.

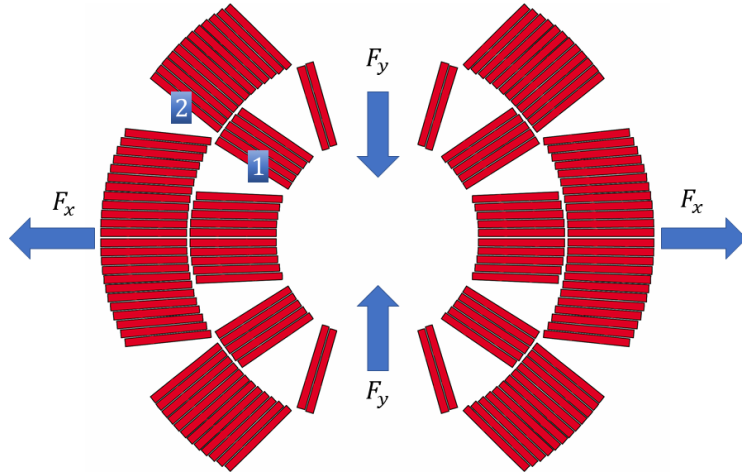


Figure 41: Lorentz forces sketch of FalconD magnet. At 12 T:  $F_{1,x} = 2208$  kN/m,  $F_{1,y} = -304$  kN/m,  $F_{2,x} = 1367$  kN/m,  $F_{2,y} = -1478$  kN/m,  $F_{tot,x} = 3575$  kN/m,  $F_{tot,y} = -1781$  kN/m. At 14 T:  $F_{1,x} = 3038$  kN/m,  $F_{1,y} = -428$  kN/m,  $F_{2,x} = 1783$  kN/m,  $F_{2,y} = -2081$  kN/m,  $F_{tot,x} = 4821$  kN/m,  $F_{tot,y} = -2509$  kN/m.

Due to these extremely high Lorentz forces acting on the windings, it is of primary importance to reduce any possible movement of the cables that, generating a local heating due to friction, could give rise to a quench. The aim of the mechanical design is to guarantee the proper pre-stress that avoid this kind of failure. Also, the optimized mechanical structure should prevent any irreversible degradation of the superconducting transport properties of the  $Nb_3Sn$  cable due to the applied pressure. For this reason, following recent works [29][30], it has been decided to conservatively set the upper stress limit of the cable to about 150 MPa independently of the temperature. Giving the proper pre-load while fulfilling the requirements on the stress limit is very challenging and demands an accurate study of the mechanical design. Collaring was discarded from the beginning, as in this case a larger fraction of the entire pre-load needs to be provided at room temperature. Instead, the natural choice is the “bladders&keys” technique, which already proved

its validity in supporting several Nb<sub>3</sub>Sn magnets [31][32][33][34]. The bladders&keys concept consists in pre-compressing the coils and iron yoke at room temperature using water-pressurized bladders and interference keys. The horizontal keys have to guarantee the mechanical continuity of the structure by aligning the SS pad and the iron yoke during the assembly. For this reason the horizontal interference is set to 0.1 mm in each configurations. The vertical keys, instead, are the one actually giving the preload to the coil by imposing a mild ovalization that counterbalance the effect of the Lorentz forces shown in Figure 41. This is achieved by bringing the two halves of the pad together, without deforming it. It is for this reason that, as shown in Figure 42, there is a 0.5 mm gap that allows to transfer the pre-load from the vertical keys to the coils. An outer Al alloy shell, shrinking more than the inner components, gives additional pre-stress to the coil at cryogenic temperature. Moreover, it has been designed a G11 key, which has the aim of preventing any unwanted rotation of the coil inside the SS pad, as represented in Figure 42.

To be noticed that this element has no mechanical impact on the system considering that there is a gap of 0.2 mm on the vertical side and a gap of 0.3 mm on the horizontal side between the key and the SS pad. By this way each component is free to shrink during the cool down without compressing all the other surrounding materials.

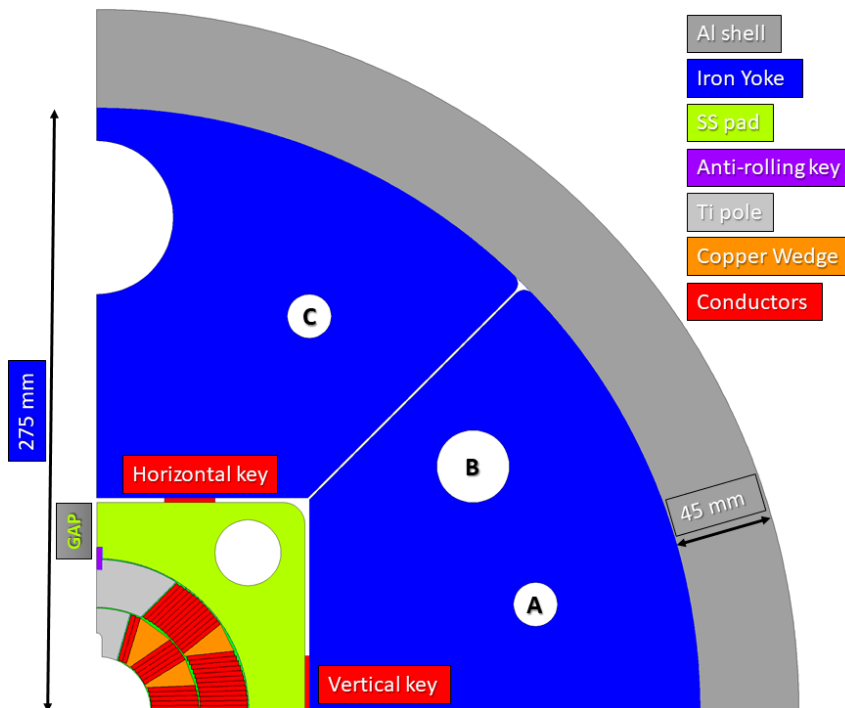


Figure 42: Layout of the 2D mechanical structure.

A complete 2D finite element analysis has been carried out to assess the validity of the bladders&keys technique and to study the stress distribution in the magnet in all the construction phases and operational condition. Due to the complexity of the system, a 3D mechanical analysis has been performed using average material properties for the coils, as illustrated in Section 5.2.1. Its goal was to assess the longitudinal pre-stress system described in Section 5.2.

### 5.1 2D Finite Element Analysis

The 2D finite element analyses have been carried out using the commercial code ANSYS [37], release 2020 R2. The adopted element is PLANE183, in plane stress configuration. Contact surfaces have been modeled between all the sliding parts using the ANSYS flexible-to-flexible contact technology, through CONTA172 and TARGE169 elements ( $\mu_r = 0.2$ ). In Figure 43 there is a schematic representation of the contacts defined in the model. The finite element mesh, containing 72 393 nodes and 24 651 elements, is shown in Figure 44.

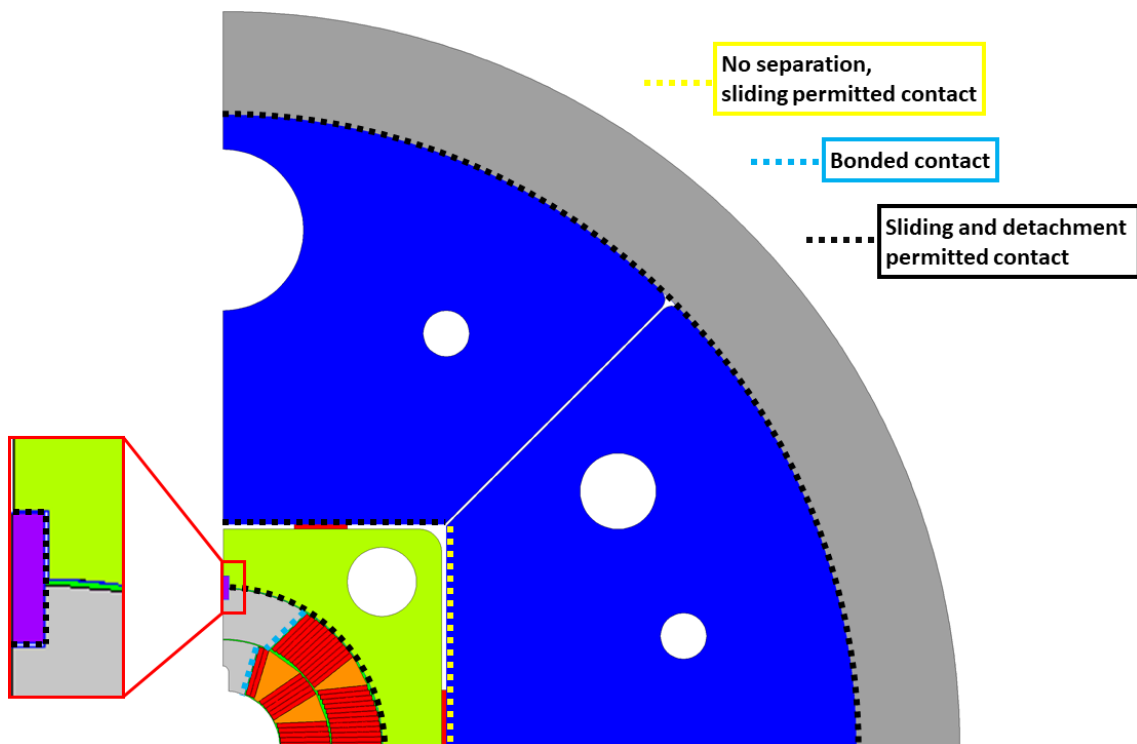


Figure 43: Scheme of the contacts definition.

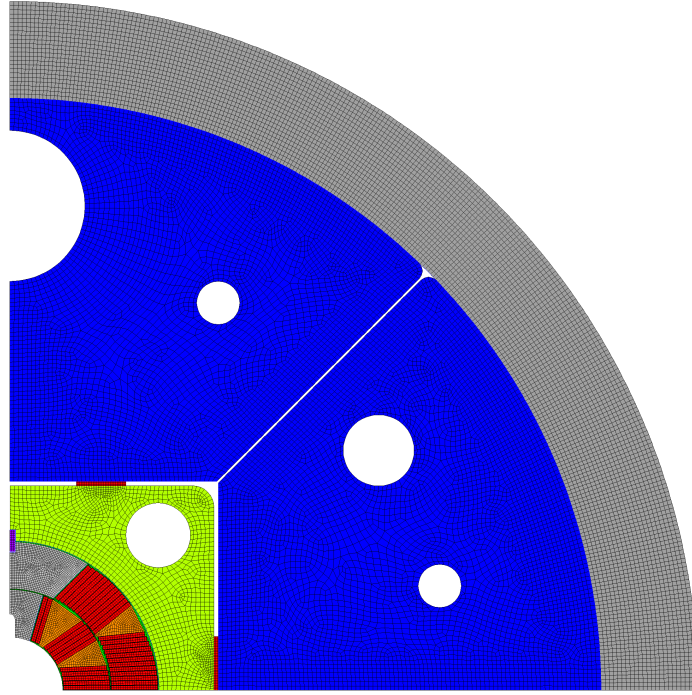


Figure 44: Finite element model for the 2D analysis.

The optimization of the mechanical design was performed with two main targets: keeping a positive contact pressure between the winding and the titanium pole during energization (i.e. a compression rather than a traction) and ensuring that all the materials involved stay within their stress limit during each step of the analysis. In Table 27 the stress limit and the material properties at room temperature and 1.9 K are listed [35] [36].

Table 27: Mechanical properties of the materials at 293 K (1.9 K)

Material	VM Stress limit [MPa]	E [GPa]	$\nu$	$\alpha \cdot 10^{-3}$
Conductors	150 (150)	25 (25)	0.3	3.8
Copper wedges	270 (>300)	100 (110)	0.3	3.37
SS pad	350 (1050)	191 (210)	0.28	2.8
Al7075 shell	480 (690)	72 (79)	0.3	4.2
Ferromagnetic iron	230 (720)	204 (225)	0.28	2.0
Ti6Al4V pole	800 (1650)	115 (127)	0.3	1.7
Fiberglass	150 (150)	25 (27.5)	0.2	2.5

The choice of making one by one trapezoidal cables is conservative. By modelling the coils as blocks you implicitly mediate the stress with the possibility of losing information on the peaks. Moreover, by this way, the calculation and distribution of Lorentz forces is much more precise considering that the force in each node is computed by an

electromagnetic ANSYS model with the same mesh in the conductors. The optimization took into account several parameters, namely, position, length and interference of the keys, thickness of the aluminum shell, the shape and the material of the pole, the 45° split in the iron yoke and the vertical division in the SS pad. Many other possibilities have been taken into account and it has been selected the one giving better results considering the targets of the optimization described before. One of the main features that required a fine optimization was the shape of the pole, more specifically the design of the notch in the lower half of the pole (i.e. its radius and its depth). It has been noticed that the notch had a major impact in lowering the peak stress in the conductors and in improving the contact pressure's distribution between the pole and the conductors. The hole identified as B in Figure 42, together with the other one in the SS pad, are provided for the longitudinal pre-load system. The two other holes, identified as A and C in Figure 42, host the tie-rods which are responsible for compacting the laminated iron yoke. The results for both the cases with the central field set to 12 T (target) and 14 T (ultimate) are reported below. While the horizontal key interference is set to 0.1 mm, the vertical one increases with the magnitude of the magnetic field, following the increase of the Lorentz forces. It has been set to 0.35 mm for the 12 T case and 0.6 mm for the 14 T one. To make enough room for the insertion of the keys it is necessary to apply a bladder pressure up to 30 MPa which generates a clearance of about 0.2 mm between the SS interference keys and the iron yoke. The 12 T configuration widely fulfills all the requirements regarding the contact pressure between winding and pole and the Von Mises stress distribution in the conductors, as shown in Figure 45 and in Figure 46.

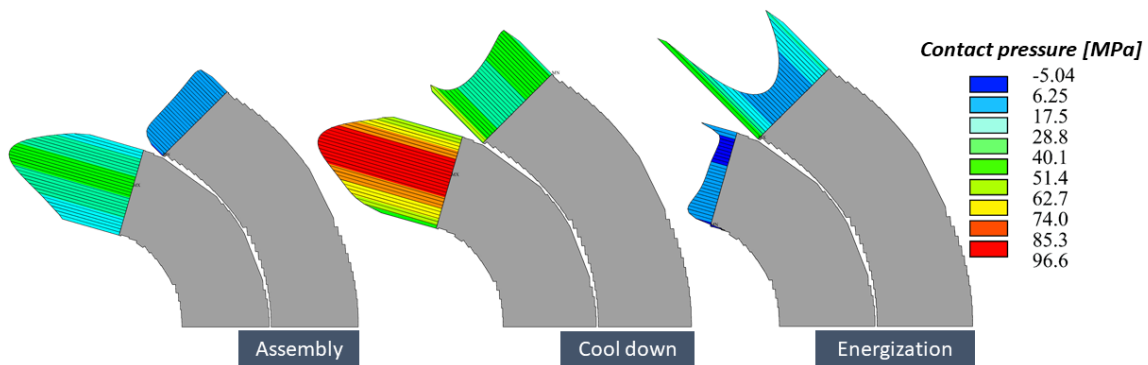


Figure 45: Contact pressure [MPa] between conductors and pole after assembly, cool down and energization at 12 T.

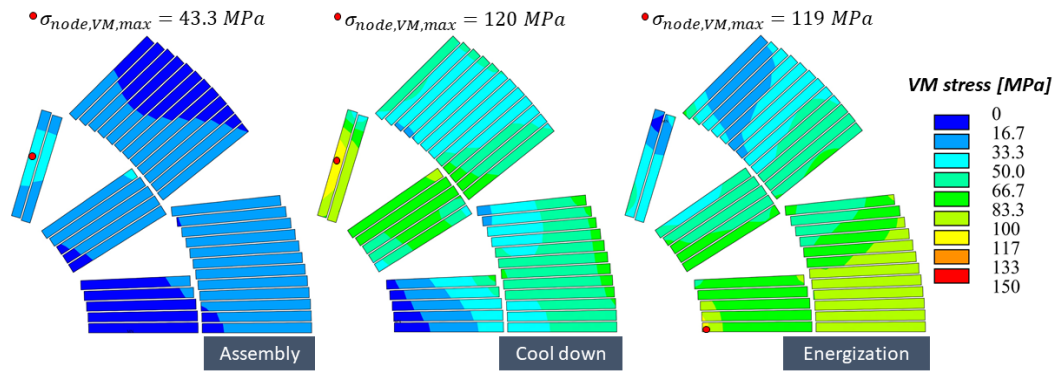


Figure 46: Von Mises stress distribution [MPa] on conductors, computed on the nodes, after assembly, cool down and energization at 12 T.

On the other hand, the 14 T configuration satisfies the contact pressure specification but the maximum stress in the conductors slightly exceed the 150 MPa limit as shown in Figure 47 and in Figure 48. To be noticed that the 150 MPa limit is fixed only for the target (nominal) operation, and the ultimate is meant to explore more stringent conditions in terms of margin and stress.

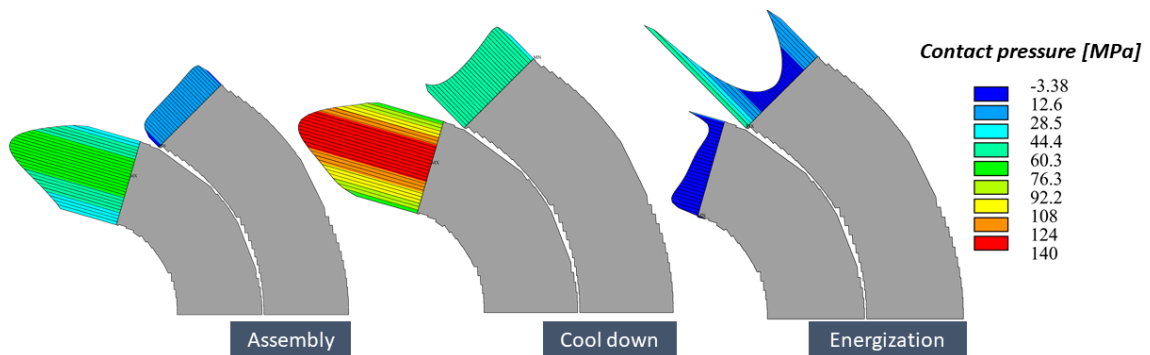


Figure 47: Contact pressure [MPa] between conductors and pole after assembly, cool down and energization at 14 T.

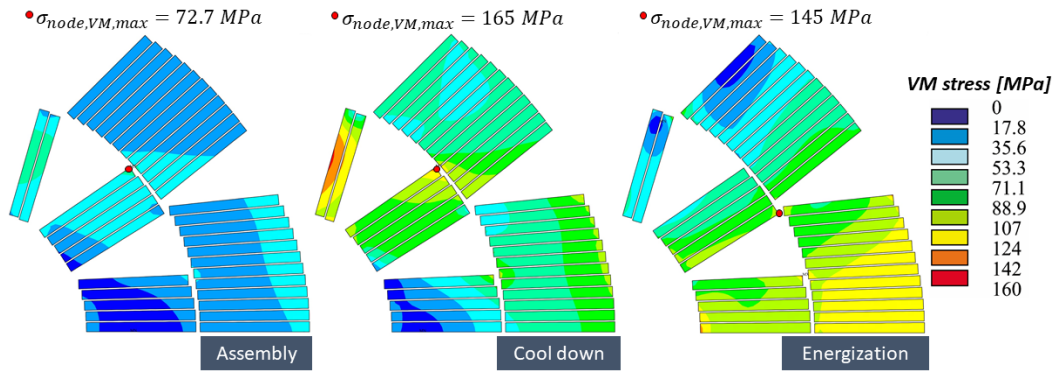


Figure 48: Von Mises stress distribution [MPa] on conductors, computed on the nodes, after assembly, cool down and energization at 14 T.

To have a better knowledge of the stress distribution in the coils it has been studied the Von Mises stress computed over the elements instead of the nodes, as shown in Figure 49 at 12 T and in Figure 50 at 14 T.

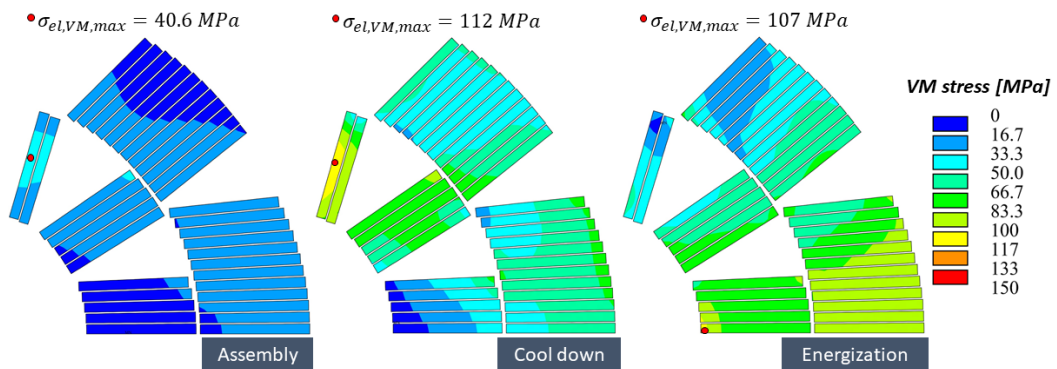


Figure 49: Von Mises stress distribution [MPa] on conductors, computed over the elements, after assembly, cool down and energization at 12 T.

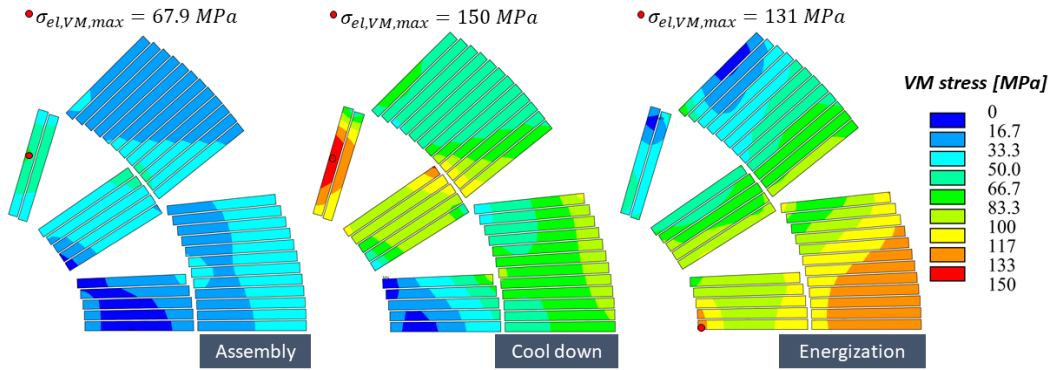


Figure 50: Von Mises stress distribution [MPa] on conductors, computed over the elements, after assembly, cool down and energization at 14 T.

For completeness are reported below, from Figure 51 to Figure 54, the displacements in the x and y directions of the conductors in the three calculation steps and it is also plotted the difference between the displacements at energization and cool down in order to better highlight the effect of the Lorentz forces in the winding. In the case of the 14 T configuration is shown in Figure 55 also the root sum square of the displacements in the x and y directions.

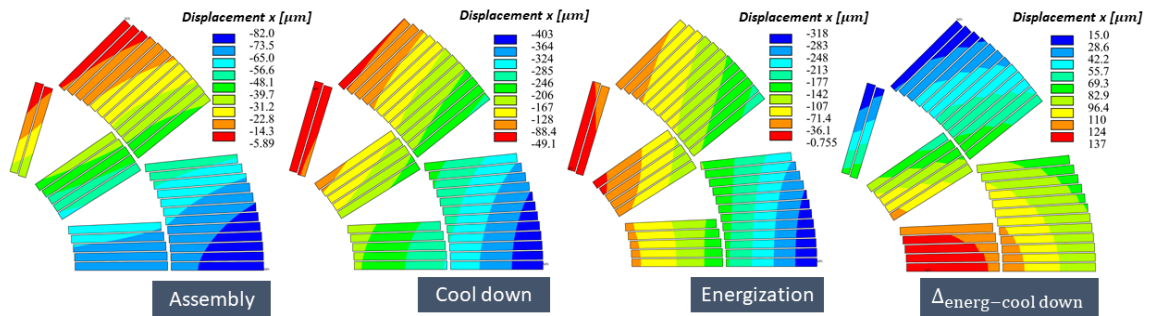


Figure 51: Displacements [ $\mu\text{m}$ ] in the x direction of the conductors at assembly, cool down, energization and the difference energization and cool down in the 12 T configuration.

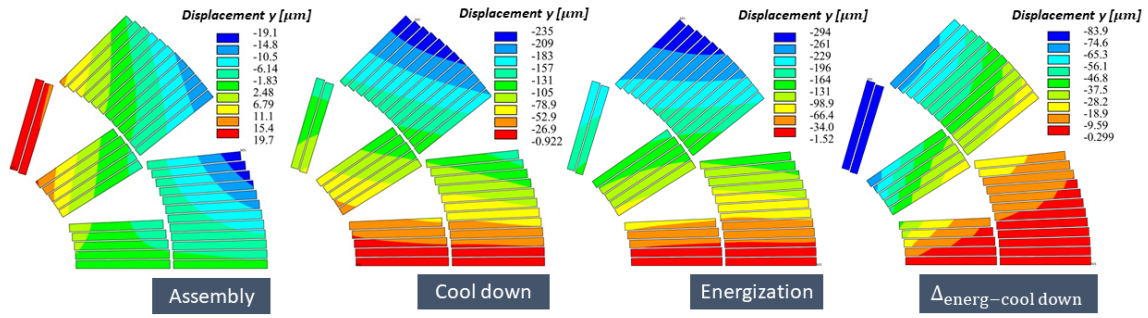


Figure 52: Displacements [ $\mu\text{m}$ ] in the y direction of the conductors at assembly, cool down, energization and the difference energization and cool down in the 12 T configuration.

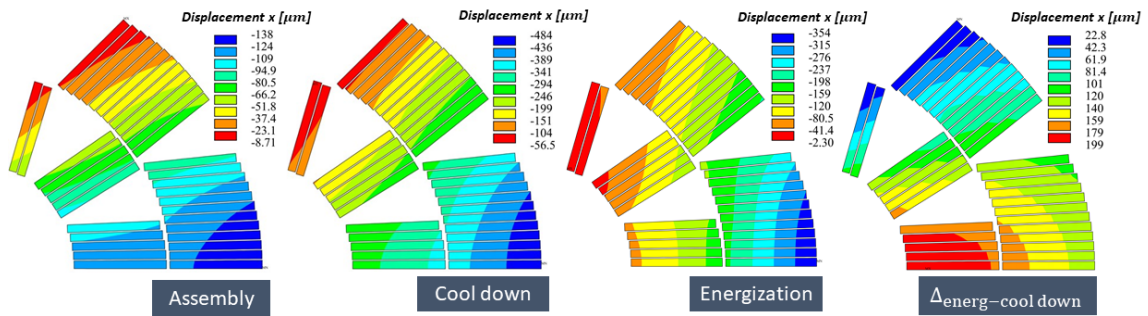


Figure 53: Displacements [ $\mu\text{m}$ ] in the x direction of the conductors at assembly, cool down, energization and the difference energization and cool down in the 14 T configuration.

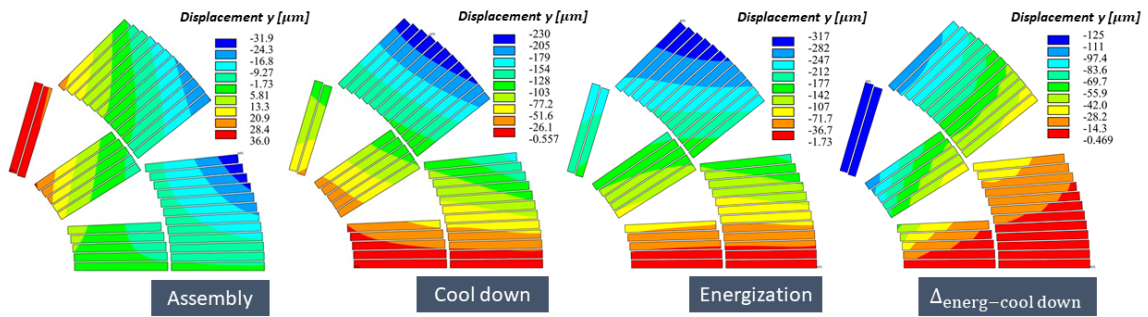


Figure 54: Displacements [ $\mu\text{m}$ ] in the y direction of the conductors at assembly, cool down, energization and the difference energization and cool down in the 14 T configuration.

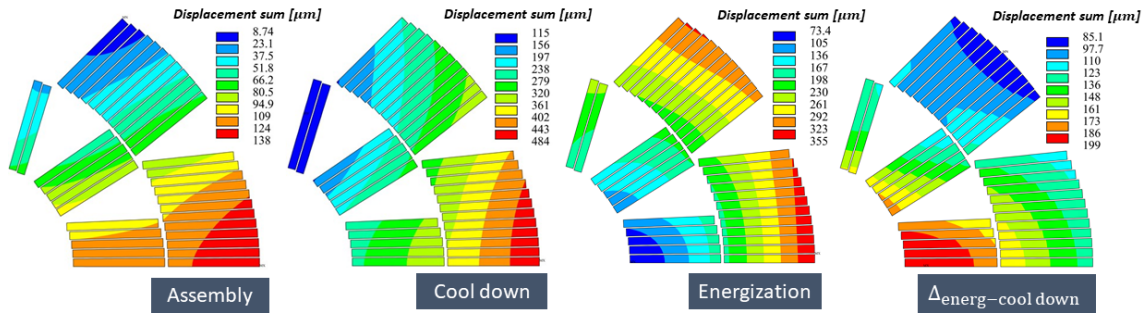


Figure 55: Root sum square of the displacements [ $\mu\text{m}$ ] in the x and y directions of the conductors at assembly, cool down, energization and the difference energization and cool down in the 14 T configuration.

A study of the Von Mises stress distribution at 14 T follows, being the most mechanically challenging configuration, for each component of the mechanical structure supporting the magnet, see from Figure 56 to Figure 60. Notice that in most of the cases the stress limit is easily satisfied except for very localised hot-spot in the stainless steel pad and in the iron yoke during assembly and cool down, in which these materials undergo plasticization. This does not involve any structural issues, it is quite common in the bladders&keys systems.

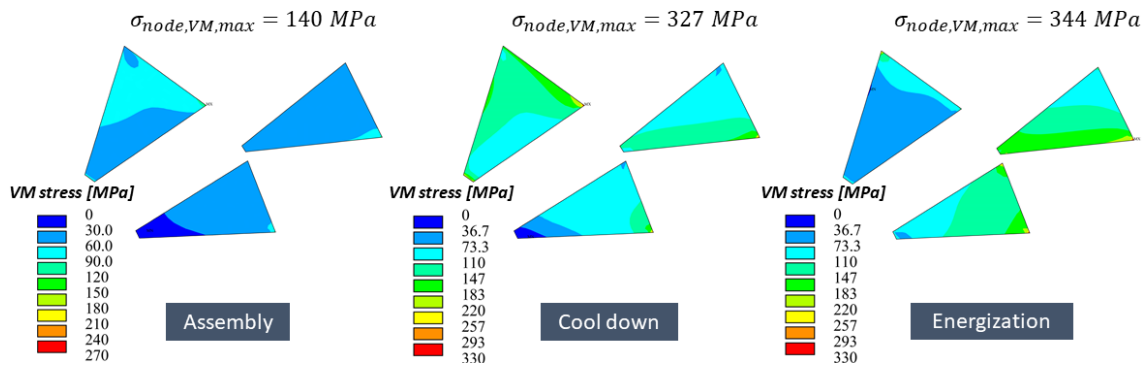


Figure 56: Von Mises stress distribution [MPa] on the copper wedges, computed on the nodes, after assembly, cool down and energization at 14 T.

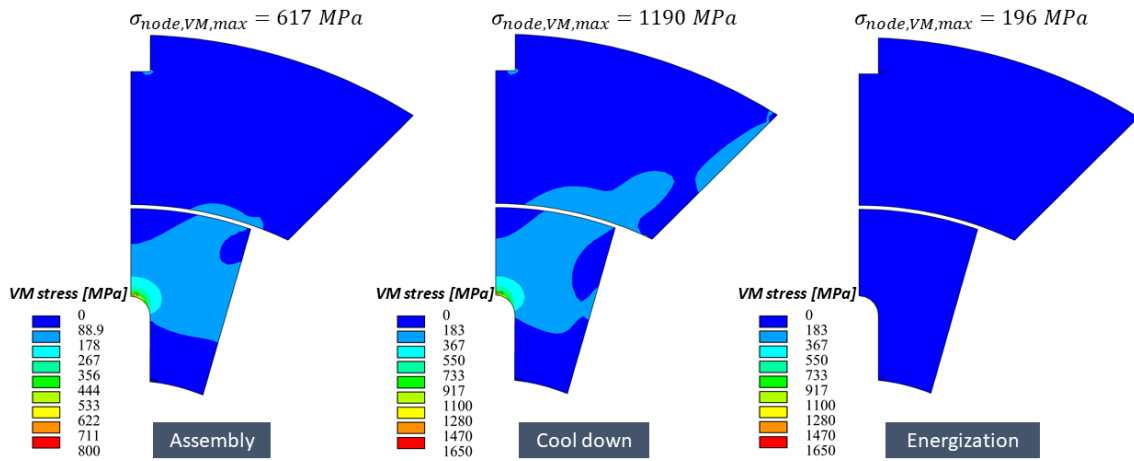


Figure 57: Von Mises stress distribution [MPa] on the titanium pole, computed on the nodes, after assembly, cool down and energization at 14 T.

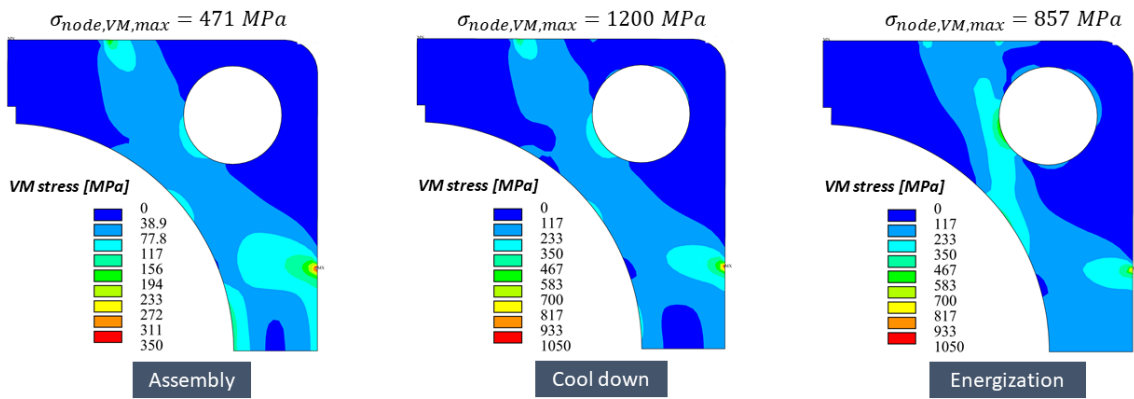


Figure 58: Von Mises stress distribution [MPa] on the SS pad, computed on the nodes, after assembly, cool down and energization at 14 T.

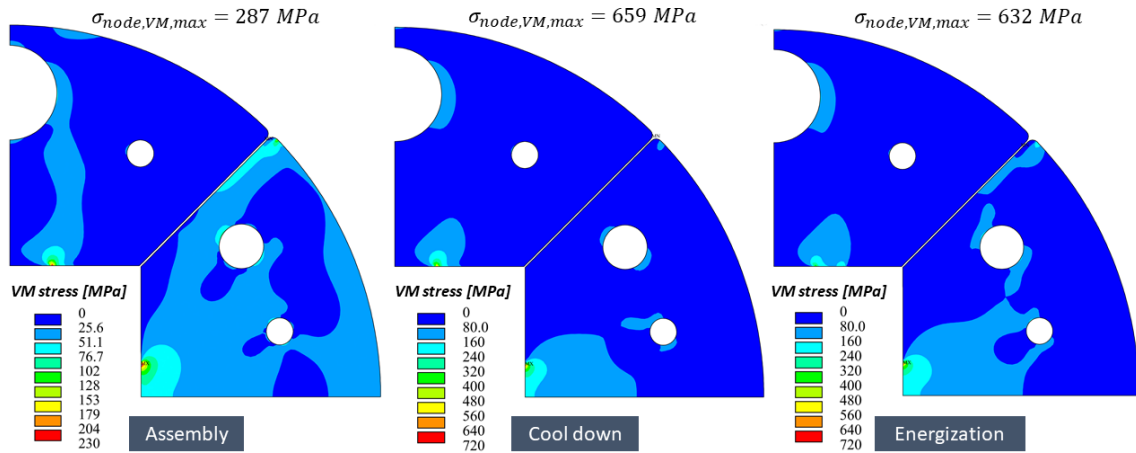


Figure 59: Von Mises stress distribution [MPa] on the iron yoke, computed on the nodes, after assembly, cool down and energization at 14 T.

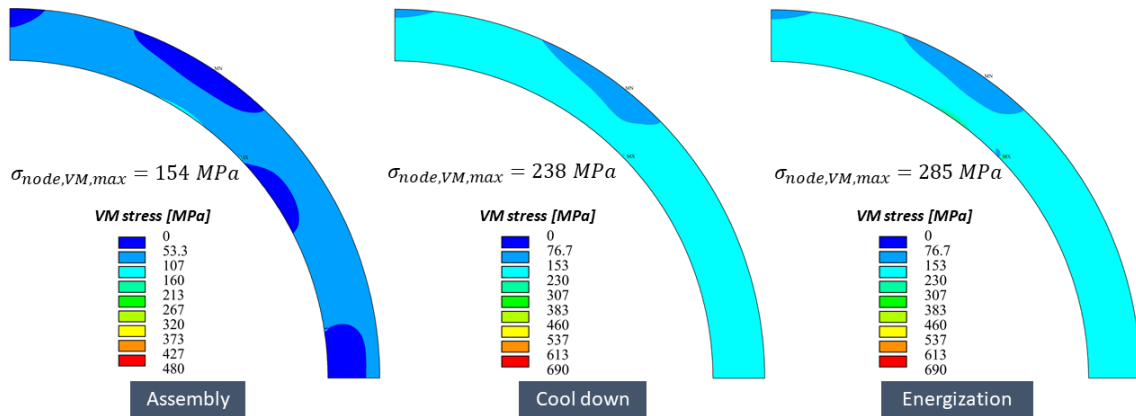


Figure 60: Von Mises stress distribution [MPa] on the aluminum alloy shell, computed on the nodes, after assembly, cool down and energization at 14 T.

Finally, the Von Mises stress distribution in the overall cold mass after energization at 14 T is shown in Figure 61.

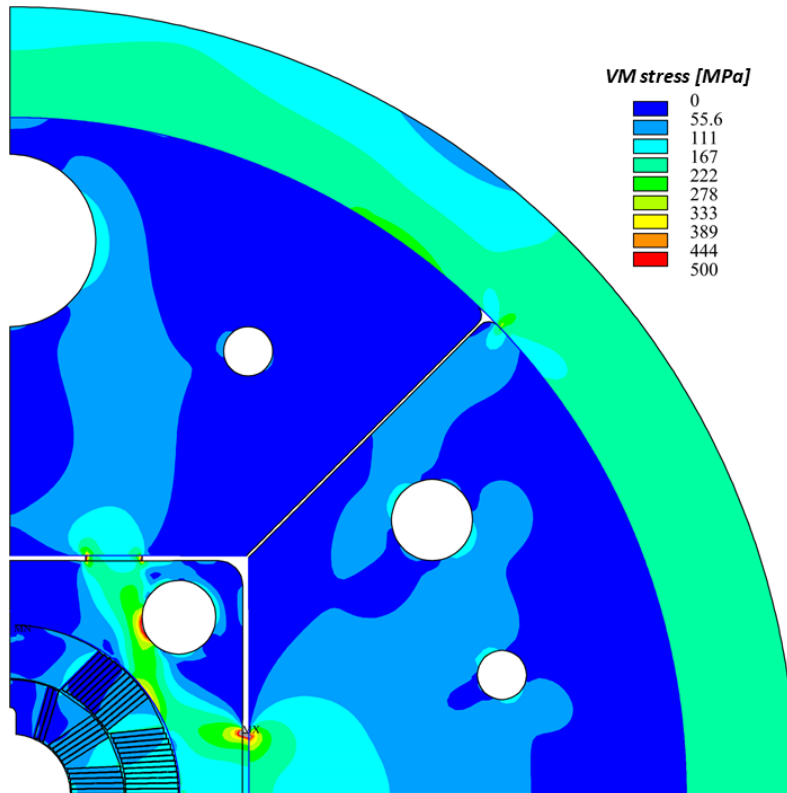


Figure 61: Von Mises stress distribution [MPa] in the cross section after energization at 14 T.

## 5.2 3D Finite Element Analysis

The main goals of the 3D analysis are to get confirmations of the results of the 2D analysis and to explore the longitudinal behavior of the magnet system. Due to the intrinsic complexity of the 3D design, the finite element model necessarily contains several simplifications. Views of the 3D model in 1/8 symmetry are shown in Figure 62 and in Figure 64, whilst an exploded view of the finite element mesh is shown in Figure 63.

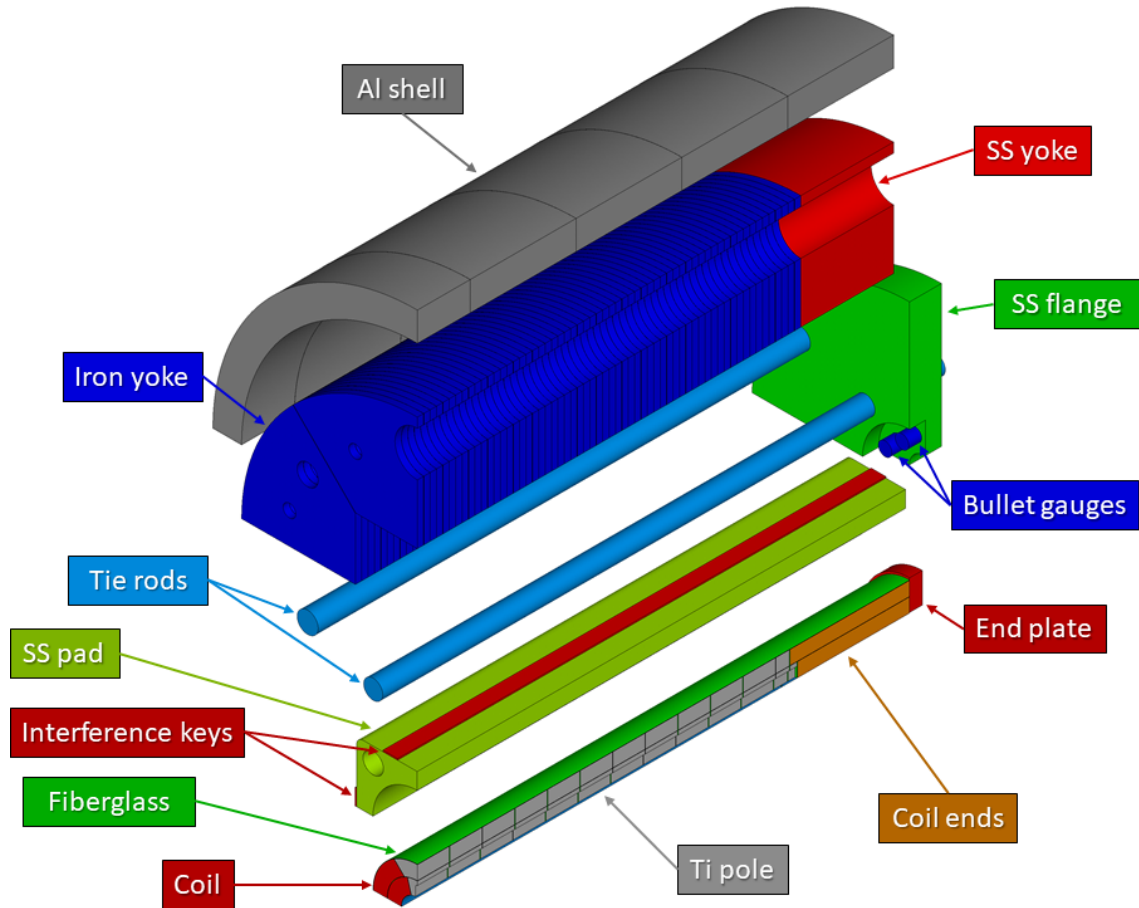


Figure 62: Layout of the 3D mechanical structure.

Main simplifications are the following:

- The coil is modeled in two parts, as shown in Figure 64, straight part in red and coil end in orange. For symmetry reasons, only half length of the magnet, 770 mm, is modeled: the coil end of the first layer is 175.2 mm long with a straight part of 594.8 mm long, while for the second layer the coil end is 187 mm long with a straight part of 583 mm. Average material properties are derived as described in 5.2.1.
- All mechanically negligible shapes are removed. Details like small holes, fillets and particular machining increase significantly the number of nodes/elements without giving a quantitative contribution to the final results.
- The thread of tie-rods is not modeled. A perfectly glued contact surface is created between tie-rods and SS flange.

- M12 fine thread pitch screws pressing on the bullet gauges are not modeled. Only the bullet gauges, which transfer the longitudinal load from the tie roads to the winding, are modeled with flat contact surfaces.

The 3D finite element analyses have been carried out using the commercial code ANSYS, release 2020 R2. The adopted element is SOLID185. Contact surfaces have been modeled between all the sliding parts using the ANSYS flexible-to-flexible contact technology, through CONTA174 and TARGE170 elements ( $\mu_r = 0.2$ ). All materials are supposed to be elastic, with Young moduli as listed in 27.

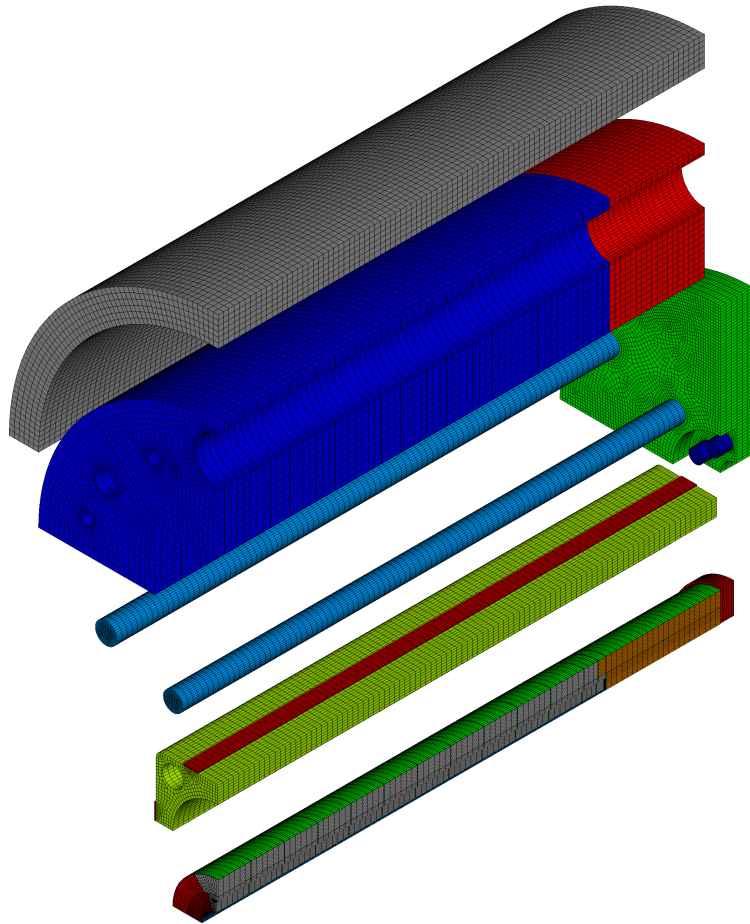


Figure 63: Exploded view of the 3D finite element mesh.

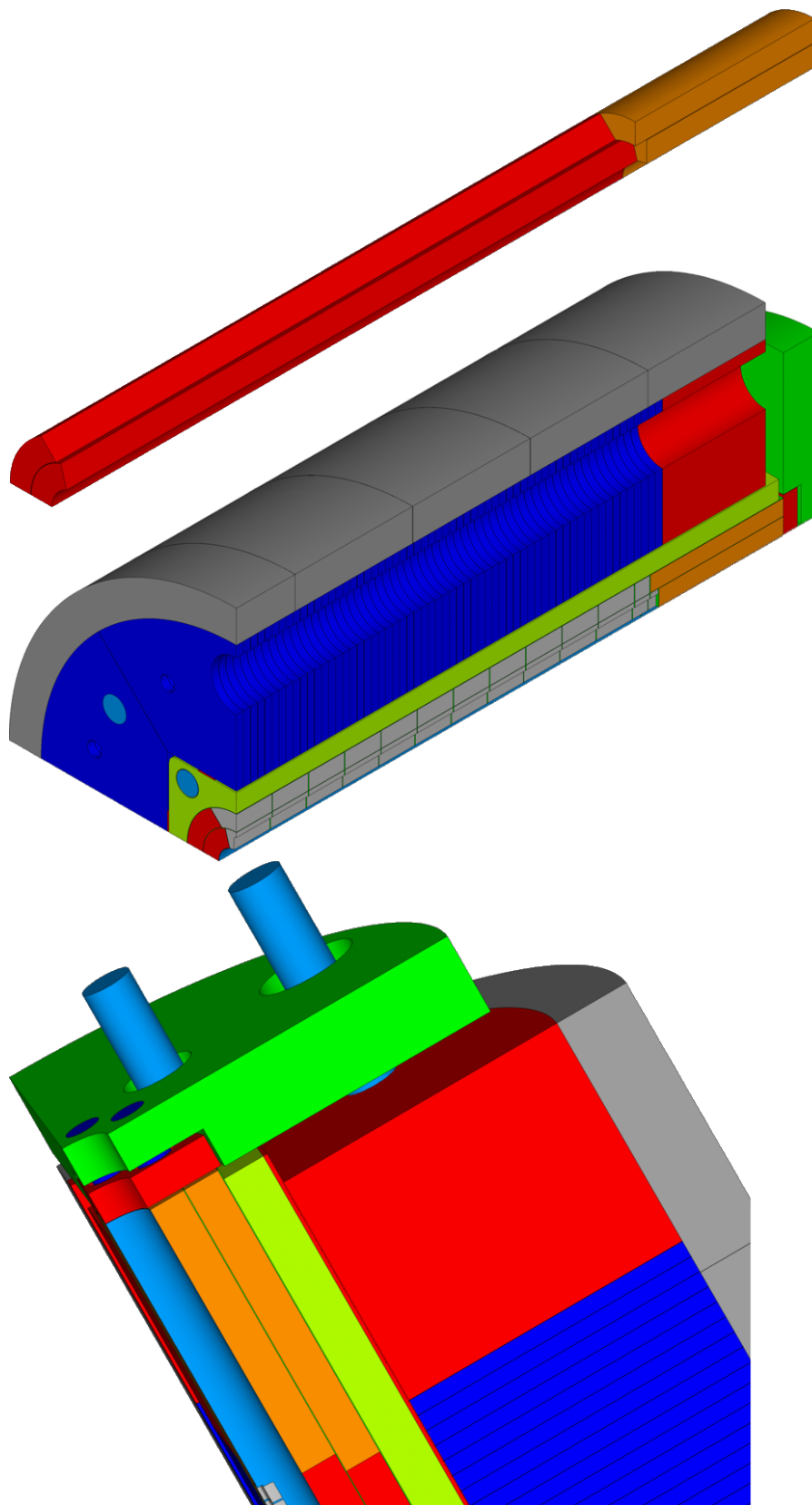


Figure 64: Views of the 3D finite element model.

### 5.2.1 Coil material properties

Average material properties of coil's straight part (Young modulus, shear modulus and thermal expansion coefficient) have been determined by exploiting the rules of composition of materials in series and parallel in the three directions: radial, azimuthal and longitudinal. In the radial direction the coil turns out to be a mechanical parallel, so the effective properties are calculated as:

$$\langle E_r \rangle = \frac{E_{cond}L_{\perp r,cond} + E_{Cu}L_{\perp r,Cu}}{L_{\perp r,cond} + L_{\perp r,Cu}} \quad (26)$$

$$\langle \alpha_r \rangle = \frac{\alpha_{cond}E_{cond}L_{\perp r,cond} + \alpha_{Cu}E_{Cu}L_{\perp r,Cu}}{E_{cond}L_{\perp r,cond} + E_{Cu}L_{\perp r,Cu}} \quad (27)$$

In the azimuthal direction the coil turns out to be a mechanical series, so the average properties are computed as:

$$\langle E_{\theta} \rangle = \frac{E_{cond}E_{Cu}(L_{\perp \theta,cond} + L_{\perp \theta,Cu})}{E_{cond}L_{\perp \theta,Cu} + E_{Cu}L_{\perp \theta,cond}} \quad (28)$$

$$\langle \alpha_{\theta} \rangle = \frac{\alpha_{cond}L_{\perp \theta,cond} + \alpha_{Cu}L_{\perp \theta,Cu}}{L_{\perp \theta,cond} + L_{\perp \theta,Cu}} \quad (29)$$

Finally, in the longitudinal direction the coil turns out to be a mechanical parallel, so the average properties are obtained as:

$$\langle E_z \rangle = \frac{E_{cond}A_{\perp z,cond} + E_{Cu}A_{\perp z,Cu}}{A_{\perp z,cond} + A_{\perp z,Cu}} \quad (30)$$

$$\langle \alpha_z \rangle = \frac{\alpha_{cond}E_{cond}A_{\perp z,cond} + \alpha_{Cu}E_{Cu}A_{\perp z,Cu}}{E_{cond}A_{\perp z,cond} + E_{Cu}A_{\perp z,Cu}} \quad (31)$$

where  $L_{\perp r}$ ,  $L_{\perp \theta}$  and  $A_{\perp z}$  are defined as represented in the Figure 65.

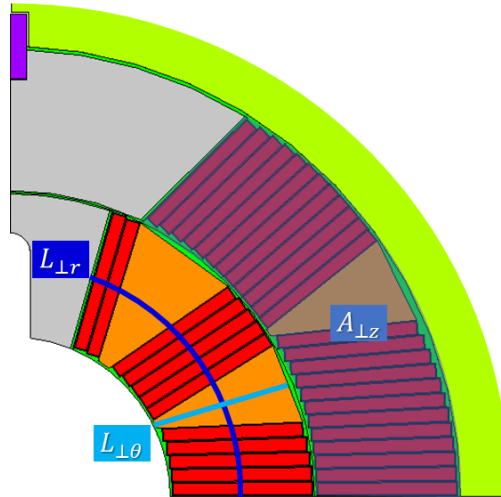


Figure 65: Schematic representation of the  $L_{\perp r}$ ,  $L_{\perp \theta}$  and  $A_{\perp z}$  parameters.

The results are summarized in Table 28 and in Table 29 for both room and cryogenic temperature. The properties used to compute the following ones are reported in Table 27.

Table 28: Average Young and shear moduli of coil's straight part in cylindrical coordinate at room temperature and (at 1.9K). Where there is just number reported it is intended as independent from temperature.

Coil	$E_r$ [GPa]	$E_\theta$ [GPa]	$E_z$ [GPa]	$G_{\theta z}$ [GPa]	$G_{rz}$ [GPa]	$G_{r\theta}$ [GPa]
Layer 1	53.7(57.5)	39.7(40.4)	53.2(57.0)	21.4	15.4	21.2
Layer 2	34.3(35.6)	39.8(40.5)	34.1(35.3)	13.4	15.5	13.4

Table 29: Average thermal expansion coefficient of coil's straight part in cylindrical coordinate.

Coil	$\alpha_r$ [mm/m]	$\alpha_\theta$ [mm/m]	$\alpha_z$ [mm/m]
Layer 1	3.49	3.59	3.49
Layer 2	3.64	3.59	3.57

Analogously to the straight part it has been carry out an approximation to compute the average mechanical properties for the coil ends. Considering the complexity of the geometry of these parts it has been decided to treat them as isotropic. More specifically it has been used the same approach and the same formulas described before for the straight part (equations from 26 to 31) but, instead of the mechanical properties of the copper, for the end spacer they have been used the SS ones. In the end, to obtain an isotropic material, it has been computed the average of the three directions' value. The results for both room and cryogenic temperature are summarized in Table 30.

Table 30: Average Young and thermal expansion coefficient of the coil ends in cylindrical coordinate at room temperature and at 1.9K.

Coil ends	E [GPa] @ RT	E [GPa] @ 1.9K	$\alpha$ [mm/m]
Layer 1	73.3	78.2	3.08
Layer 2	44.9	46.6	3.23

### 5.2.2 Magnetic forces

The 3D Lorentz forces acting in the magnet have been calculated through a 2D and 3D ANSYS magnetic model and a 3D OPERA [17] model. In Table 31 the Lorentz forces per unit length for each block of conductors in the straight part of one eighth of the magnet are reported at the nominal current for both the 12 T and the 14 T configurations. From the

OPERA 3D model the total Lorentz forces acting on each layer, discriminating straight parts and coil ends, are calculated on one eighth of the magnet system and they are listed in Table 32. These calculated Lorentz forces are introduced into the 3D ANSYS mechanical model to simulate the energization of the magnet. They are uniformly distributed in each interested volume.

Table 31: The Lorentz forces per unit length for each block of conductors in the straight part of one eighth of the magnet at 12 T and at 14 T.

12 T					
Layer	# of block (from midplane to pole)	2D ANSYS model		3D OPERA model	
		$F_x$ [kN/m]	$F_y$ [kN/m]	$F_x$ [kN/m]	$F_y$ [kN/m]
1	1	829	-104	857	-76
	2	934	-140	950	-156
	3	445	-59	399	-69
total		2208	-303	2206	-301
2	1	217	-535	687	-710
	2	1150	-942	671	-765
total		1367	-1477	1358	-1475
<b>grand total</b>		<b>3575</b>	<b>-1780</b>	<b>3564</b>	<b>-1776</b>

14 T					
Layer	# of block (from midplane to pole)	2D ANSYS model		3D OPERA model	
		$F_x$ [kN/m]	$F_y$ [kN/m]	$F_x$ [kN/m]	$F_y$ [kN/m]
1	1	1138	-146	1140	-147
	2	1286	-198	1286	-198
	3	615	-84	615	-84
total		3038	-428	3041	-429
2	1	232	-751	232	-753
	2	1550	-1329	1551	-1329
total		1783	-2081	1784	-2082
<b>grand total</b>		<b>4821</b>	<b>-2509</b>	<b>4825</b>	<b>-2511</b>

Table 32: The Lorentz forces for first and second layer in the straight part and in the coil end of one eighth of the magnet at 12 T and 14 T.

12 T							
Layer	Straight part			Coil end			
	L [mm]	$F_x$ [kN]	$F_y$ [kN]	L [mm]	$F_x$ [kN]	$F_y$ [kN]	$F_z$ [kN]
1	594.8	1312	-179	175.2	122	-6	48
2	583	792	-860	187	102	-109	81

14 T							
Layer	Straight part			Coil end			
	L [mm]	$F_x$ [kN]	$F_y$ [kN]	L [mm]	$F_x$ [kN]	$F_y$ [kN]	$F_z$ [kN]
1	594.8	1809	-255	175.2	169	-9	66
2	583	1040	-1214	187	136	-154	112

The 3D ANSYS magnetic model has been used as a corroboration for the OPERA 3D model. In the Table 33 is reported the comparison between these two models.

Table 33: The Lorentz forces for first and second layer of one eighth of the magnet at 12 T and 14 T computed by the 3D OPERA and ANSYS models and the difference between them.

		12 T			14 T		
		$F_x$ [kN]	$F_y$ [kN]	$F_z$ [kN]	$F_x$ [kN]	$F_y$ [kN]	$F_z$ [kN]
OPERA	Layer 1	1434	-185	48	1978	-264	66
	Layer 2	894	-969	81	1176	-1368	112
ANSYS	Layer 1	1436	-185	47	1978	-261	66
	Layer 2	898	-971	82	1177	-1368	113
Differences	Layer 1	-2	0	1	0	-3	0
	Layer 2	0	-4	-1	-1	0	-1

### 5.2.3 Longitudinal preloading system

Longitudinal pre-stress is provided by eight tie-rods, four of which are 30 mm thick acting on the SS pad, while the other four are 36 mm in diameter, as shown in Figure 62. The maximum applicable load on the tie-rods has been set to 200 MPa. Load is applied by screwing the rods, which is quite complicated in a finite element analysis. Since the effect of the screwing is reducing the length of the active part of the rod, this effect has been simulated by pulling the face of the rod opposite to the thread, which is not connected to other parts of the finite element model and is then available to apply a displacement. Cooling-down increases the pre-load on the tie-rods because of the differential thermal

contractions of the magnet's system components. Basically, the idea is that the longitudinal pre-load should limit the coil end movements between cool down and powering within a safe limit. Generally, the pre-load corresponds to a fraction of around 50% of the longitudinal Lorentz force. More specifically, it is required that the pre-load is large enough to ensure that the coil end is held under compression during powering, i.e. that the coil end never elongates during powering relative to its value at cold under free conditions. In Table 34 and in Table 35 absolute displacements after cool down and powering are shown together with the values referred to the system in free conditions (i.e. without tie-rods) at 12 T and 14 T respectively. It is evident that if the magnet system were left without any longitudinal preloading system, it would lengthen of about 1 tenth of a mm in the 12 T configuration and of 0.13 mm in the 14 T one, potentially creating severe problems in the end region.

Table 34: Absolute coil end elongations at cool down and powering on the left and the same values referred to the cold system in free conditions on the right at 12 T.

	<b>12 T</b>			
	Cool down [mm]	Powering [mm]	Cool down WRT free condition [mm]	Powering WRT free condition [mm]
No rods	-1.98	-1.88	0	+0.1
0% $F_L$	-2.00	-1.92	-0.02	+0.06
25% $F_L$	-2.05	-1.97	-0.07	+0.01
50% $F_L$	-2.09	-2.01	-0.11	-0.03

Table 35: Absolute coil end elongations at cool down and powering on the left and the same values referred to the cold system in free conditions on the right at 14 T.

	<b>14 T</b>			
	Cool down [mm]	Powering [mm]	Cool down WRT free condition [mm]	Powering WRT free condition [mm]
No rods	-1.95	-1.82	0	+0.13
0% $F_L$	-1.97	-1.86	-0.02	+0.09
25% $F_L$	-2.03	-1.92	-0.08	+0.03
50% $F_L$	-2.09	-1.99	-0.14	-0.04

Preloading the 12 T configuration up to 25% of the Lorentz force is enough to minimize the elongation of the coil end. On the other hand, for the 14 T configuration is necessary to provide a pre-load of 50% of the longitudinal Lorentz force. As can be seen from Table 34 and Table 35, the elongation of the coil end during powering with

respect to the system in free condition at cool down is very small. This is due to the high friction between the winding, the Ti pole and the SS pad. Usually this phenomenon would be mitigated by the lamination of the pad, but in this case it has been decided to have it as a single piece. To demonstrate this correlation it has been created a specific ANSYS model in which the friction coefficient between the winding, the pole and the pad as been set to zero instead of 0.2; at the same time it has been computed by hand with a rough calculation the foreseen elongation: both of these analysis gave as a result an elongation of about 0.4 mm. To complete the information, Table 36 and Table 37 resumes the longitudinal reaction forces in the magnet components at assembly, cool down and powering at both 12 T and 14 T.

Table 36: Longitudinal reaction forces in magnet components at 12 T in kN.

<b>12 T</b>						
loadstep	coils	SS pad + keys	iron yoke	Al shell	tie-rods	<b>total</b>
assembly	24.7	7.8	0.1	-0.6	-32.0	<b>0.0</b>
cool down	84.9	-28.4	4.6	-11.6	-49.5	<b>0.0</b>
powering	54.0	-110.2	4.2	-11.4	-64.9	<b>-128.3</b>

Table 37: Longitudinal reaction forces in magnet components at 14 T in kN.

<b>14 T</b>						
loadstep	coils	SS pad + keys	iron yoke	Al shell	tie-rods	<b>total</b>
assembly	44.2	45.1	0.3	-0.7	-88.9	<b>0.0</b>
cool down	112.3	6.7	5.4	-12.9	-111.5	<b>0.0</b>
powering	67.3	-104.5	5.2	-13.1	-132.7	<b>-177.8</b>

It is worth noting that at assembly and cool down, where there are no imposed forces, the sum of the longitudinal reaction forces is null; instead at energization, both for the 12 T configuration and the 14 T one, the total reaction force exactly corresponds to the Lorentz force, as expected.

#### 5.2.4 Results of the 3D mechanical analysis

In this section are reported the results from the 3D fem mechanical analysis for each one of the mechanical components, step by step from assembly to energization for bot the 12 T and 14 T configuration. Due to the approximations and the roughness of the 3D model with the equivalent mechanical properties of the conductors (see section 5.2.1) it

is not possible to compare the peak stress in the components. For these reasons in the following tables (Table 38, 39 and 40) are reported the mean Von Mises Stress for each material in the cross section of the 2D model and in a 20 mm thick slice in the center of the 3D model.

Table 38: Average stress in each component of the cross section at assembly, both at 12 and 14 T.

<b>Assembly</b>	<b>12 T [MPa]</b>			<b>14 T [MPa]</b>		
	<b>2D</b>	<b>3D straight</b>	<b>difference</b>	<b>2D</b>	<b>3D straight</b>	<b>difference</b>
$\sigma_{avg}$ Al shell	37.2	35.9	<b>-1.3</b>	58.6	56.3	<b>-2.3</b>
$\sigma_{avg}$ iron yoke	14.2	13.6	<b>-0.6</b>	22.9	22.0	<b>-0.9</b>
$\sigma_{avg}$ SS pad	27.5	25.0	<b>-2.5</b>	42.9	36.4	<b>-6.5</b>
$\sigma_{avg}$ Ti pole	35.9	28.2	<b>-7.7</b>	59.6	44.4	<b>-15.2</b>
$\sigma_{avg}$ layer 1	23.6	19.2	<b>-4.4</b>	39.5	32.2	<b>-7.3</b>
$\sigma_{avg}$ layer 2	21.0	28.7	<b>7.7</b>	34.9	44.1	<b>9.2</b>

Table 39: Average stress in each component of the cross section at cool down, both at 12 and 14 T.

<b>Cool down</b>	<b>12 T [MPa]</b>			<b>14 T [MPa]</b>		
	<b>2D</b>	<b>3D straight</b>	<b>difference</b>	<b>2D</b>	<b>3D straight</b>	<b>difference</b>
$\sigma_{avg}$ Al shell	152.0	144.3	<b>-7.7</b>	173.6	164.0	<b>-9.6</b>
$\sigma_{avg}$ iron yoke	41.0	40.5	<b>-0.5</b>	48.1	47.9	<b>-0.2</b>
$\sigma_{avg}$ SS pad	100.9	106.0	<b>5.1</b>	112.5	112.8	<b>0.3</b>
$\sigma_{avg}$ Ti pole	107.3	118.8	<b>11.5</b>	139.7	137.1	<b>-2.6</b>
$\sigma_{avg}$ layer 1	63.8	68.5	<b>4.7</b>	84.6	81.6	<b>-3</b>
$\sigma_{avg}$ layer 2	55.4	89.8	<b>34.4</b>	74.2	111.0	<b>36.8</b>

Table 40: Average stress in each component of the cross section at energization, both at 12 and 14 T.

<b>Energization</b>	<b>12 T [MPa]</b>			<b>14 T [MPa]</b>		
	<b>2D</b>	<b>3D straight</b>	<b>difference</b>	<b>2D</b>	<b>3D straight</b>	<b>difference</b>
$\sigma_{avg}$ Al shell	153.5	144.5	<b>-9.0</b>	177.4	167.0	<b>-10.4</b>
$\sigma_{avg}$ iron yoke	44.9	42.1	<b>-2.8</b>	53.2	50.6	<b>-2.6</b>
$\sigma_{avg}$ SS pad	101.9	114.2	<b>12.3</b>	114.0	125.5	<b>11.5</b>
$\sigma_{avg}$ Ti pole	48.0	145.7	<b>97.7</b>	53.7	172.2	<b>118.5</b>
$\sigma_{avg}$ layer 1	66.0	76.7	<b>10.7</b>	82.1	91.4	<b>9.3</b>
$\sigma_{avg}$ layer 2	68.1	107.7	<b>39.6</b>	88.8	132.5	<b>43.7</b>

As shown by the previous tables the differences between the calculation of the 2D and 3D models, except for Ti pole and layer 2, are within a range of 15 MPa in each

simulated step, which is an acceptable agreement considering the different approximation that differentiate the two models. To be noticed that at cool down and energization the difference between the average Von Mises stress in the Ti pole and in the second layer of the winding is pretty large. To study these discrepancies, a 3D model was made, obtained by extruding the 2D model: by extruding it by 1 mm the differences with the 2D model were negligible, by extruding it by 1 m the results were much closer to the 3D model. This means that these discrepancies are not due to some kind of modeling error in the 3D model but they are linked to the approximation done in considering the 2D model as infinitely thin (i.e. working in *plane stress* approximation).

Figure 66 to Figure 71 report the comparison between the Von Mises Stress distribution at assembly, cool down and energization in the 2D and 3D models in both the 12 T and 14 T configuration, respectively.

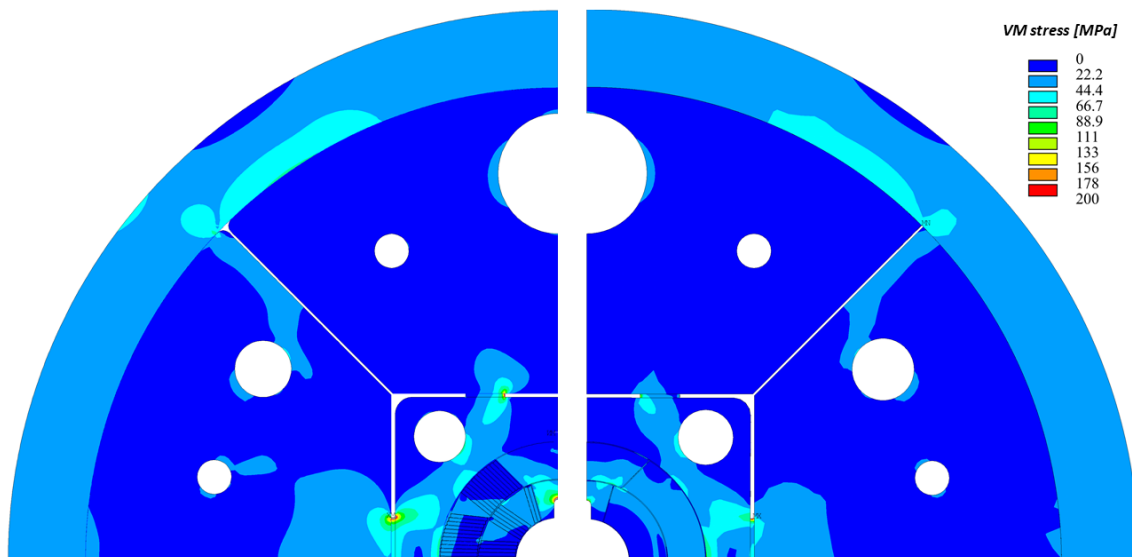


Figure 66: Von Mises stress distribution [MPa] in the cross section at assembly in the 12 T configuration. On the left there is the 2D model and on the right the 3D one.

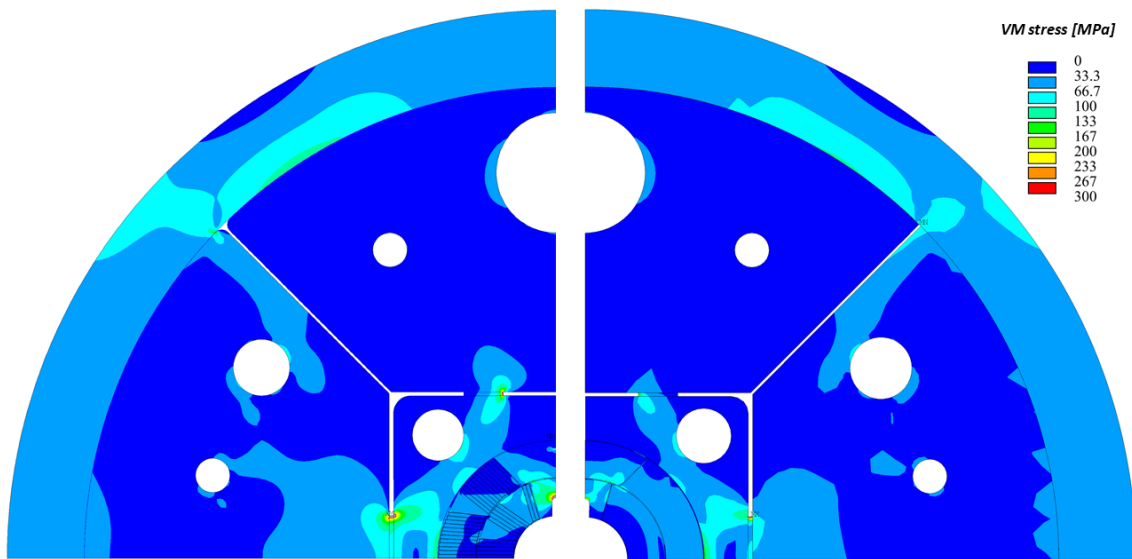


Figure 67: Von Mises stress distribution [MPa] in the cross section at assembly in the 14 T configuration. On the left there is the 2D model and on the right the 3D one.

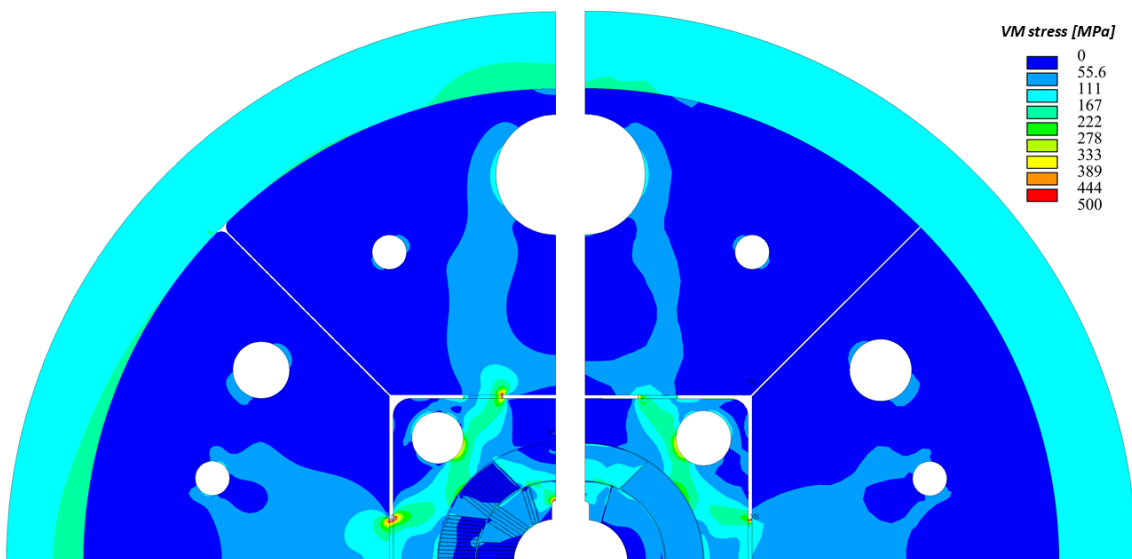


Figure 68: Von Mises stress distribution [MPa] in the cross section at cool down in the 12 T configuration. On the left there is the 2D model and on the right the 3D one.

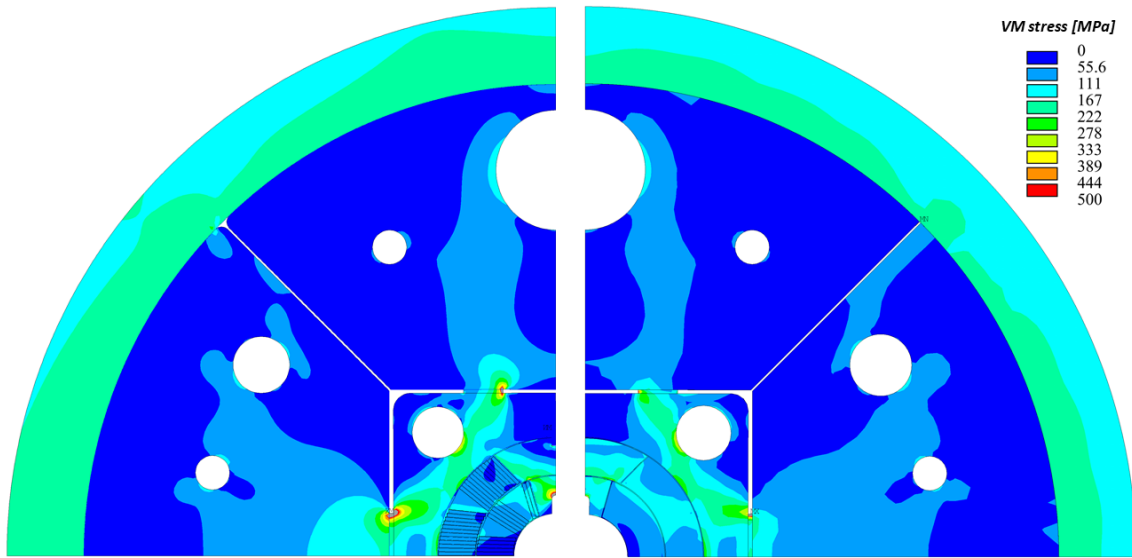


Figure 69: Von Mises stress distribution [MPa] in the cross section at cool down in the 14 T configuration. On the left there is the 2D model and on the right the 3D one.

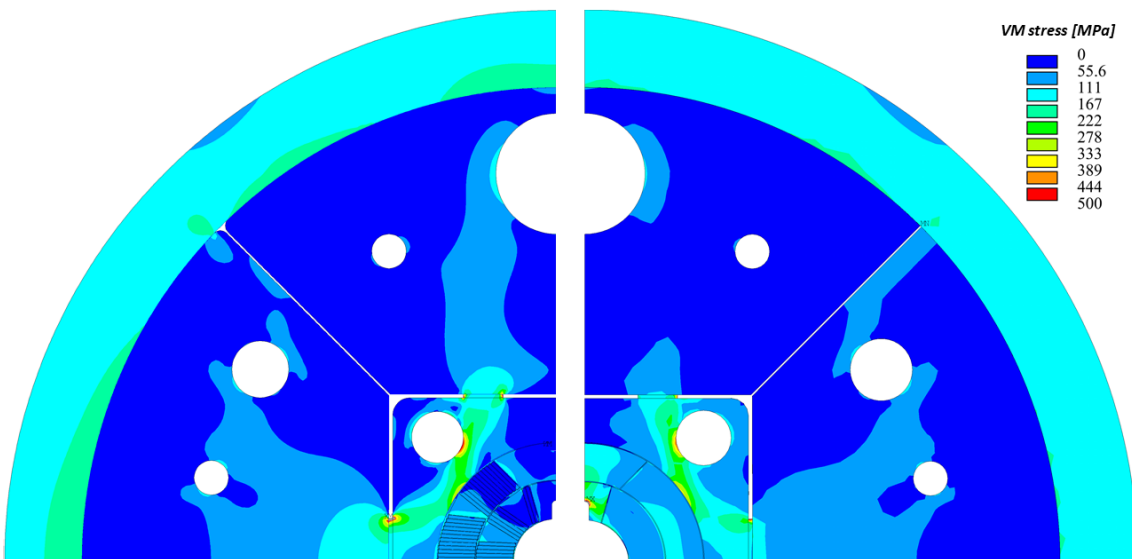


Figure 70: Von Mises stress distribution [MPa] in the cross section at energization in the 12 T configuration. On the left there is the 2D model and on the right the 3D one.

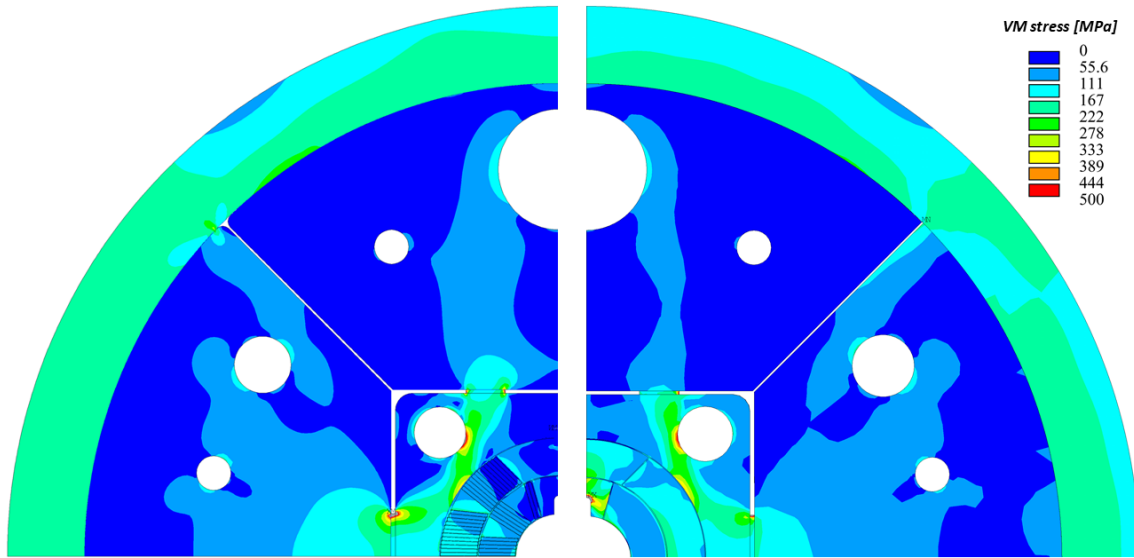


Figure 71: Von Mises stress distribution [MPa] in the cross section at energization in the 14 T configuration. On the left there is the 2D model and on the right the 3D one.

The following figures (from Figure 72 to Figure 75) present the Von Mises stress distribution in the components of the longitudinal preloading system at assembly, cool down and energization in the 14 T configuration, considering that it is the most mechanically challenging configuration.

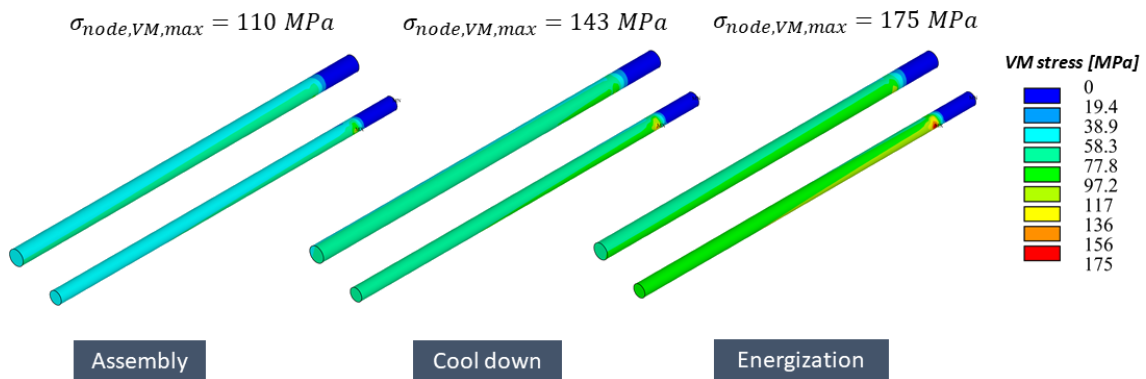


Figure 72: Von Mises stress distribution [MPa] in the tie-rods at assembly, cool down and energization in the 14 T configuration.

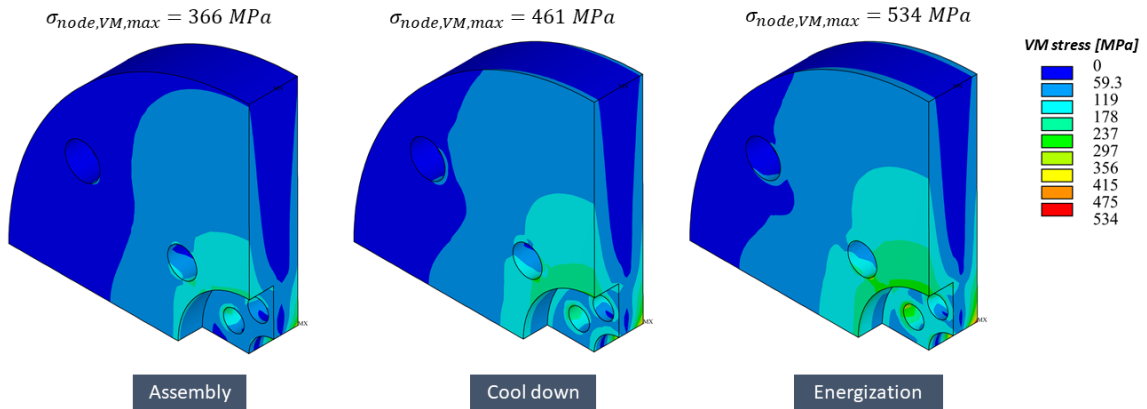


Figure 73: Von Mises stress distribution [MPa] in the SS flange at assembly, cool down and energization in the 14 T configuration.

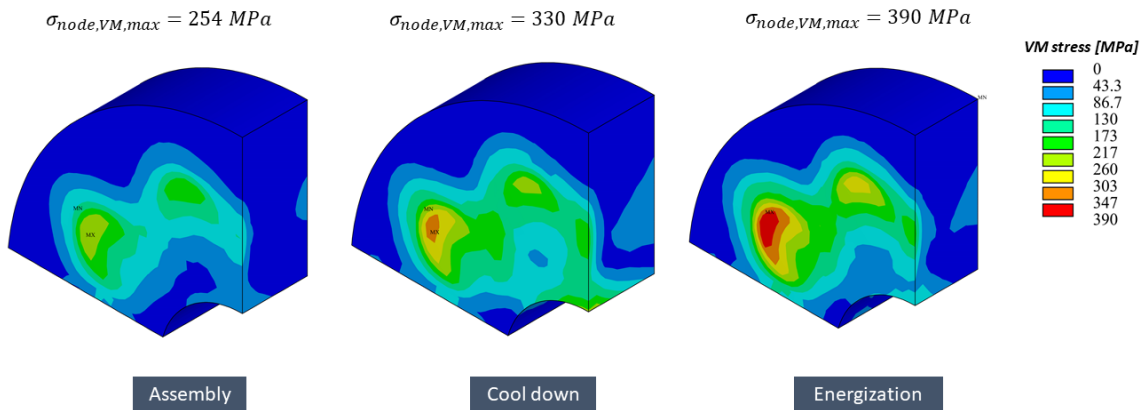


Figure 74: Von Mises stress distribution [MPa] in the end plate at assembly, cool down and energization in the 14 T configuration.

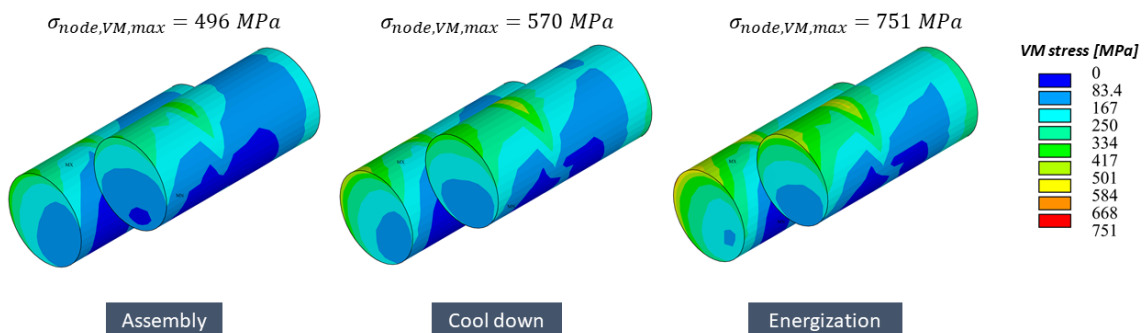


Figure 75: Von Mises stress distribution [MPa] in the bullet gauges at assembly, cool down and energization in the 14 T configuration.

## 6 MAGNET MAIN FEATURES

This section presents a description of the cold mass, supported by basic technical drawings and information regarding the intended manufacturing methods. The coils will be produced by ASG Superconductors. The mechanical assembly will be performed at INFN Milano-LASA Laboratory.

### 6.1 Turn distribution

The conductor is described in detail in the dedicated chapter 2. It is important to note that at this time the conductor has never been cabled from the strands, so its dimensions were estimated only from geometric considerations. This may require a second design iteration when the actual dimensions of the conductor are known. Insulation is made of S2 sleeves, 0.15 mm thick, suitable for both heat treatment and impregnation. The distribution of turns in two layers was achieved through a process of field quality optimization, performed before any winding tests were done on the conductor. Again, this could lead to an iteration of the design if it is discovered that the conductor does not naturally follow the designed curvature in the ends of the coil.

Figure 76 shows the distribution of the turns in 1/4 symmetry. Optimization was performed by prioritizing technical feasibility rather than absolute field quality. Therefore, the minimum bending radius of the cable is fixed at about 10 mm, the minimum size of the copper wedge is fixed at 1 mm, and the inclination of the turns is rather natural, avoiding extreme angles.

Properly shaped Glidcop copper wedges are placed between the conductor blocks: these parts will be insulated using the same technique and materials used for the conductor (S2 sleeves).

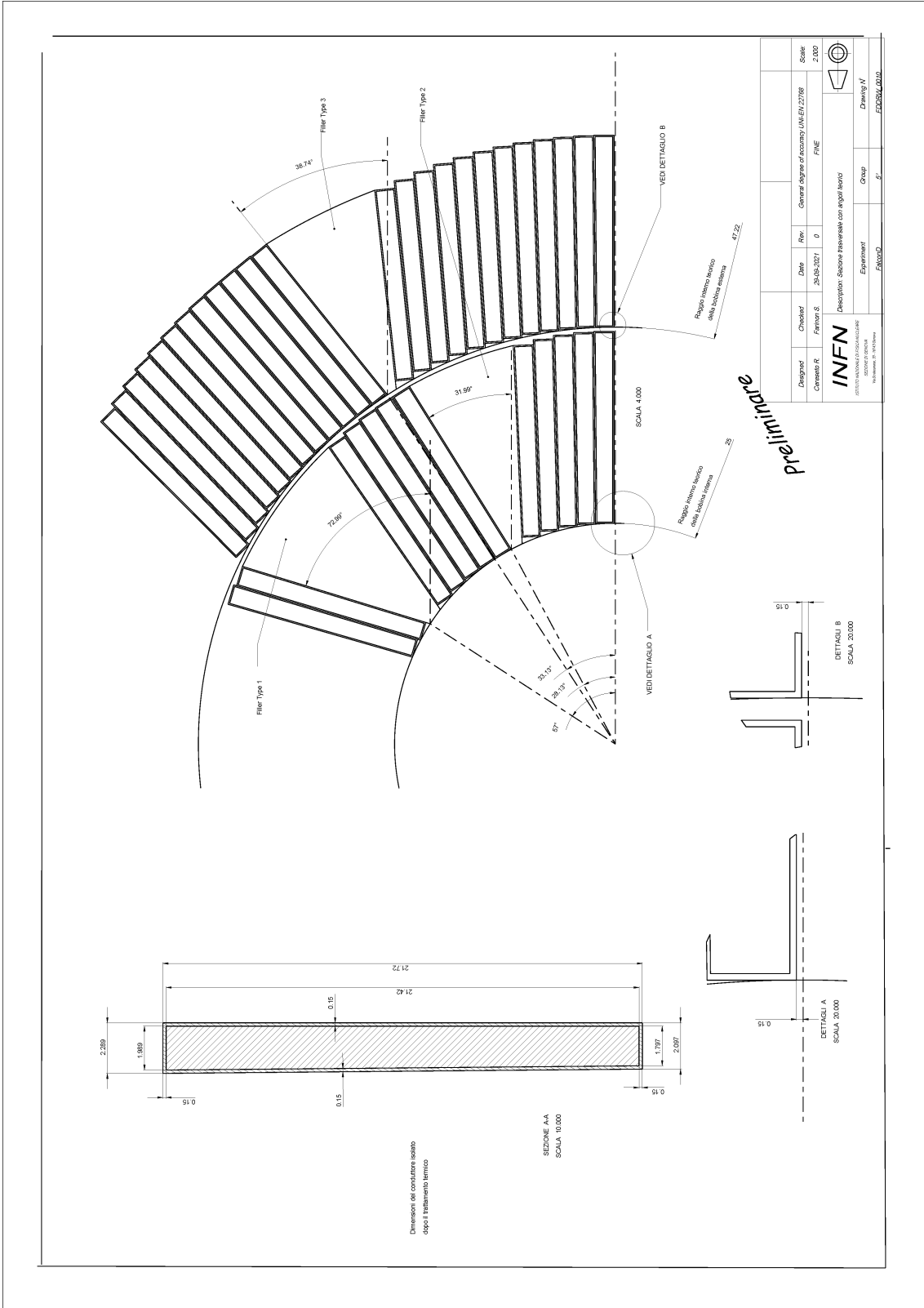


Figure 76: Turn distribution and conductor details.

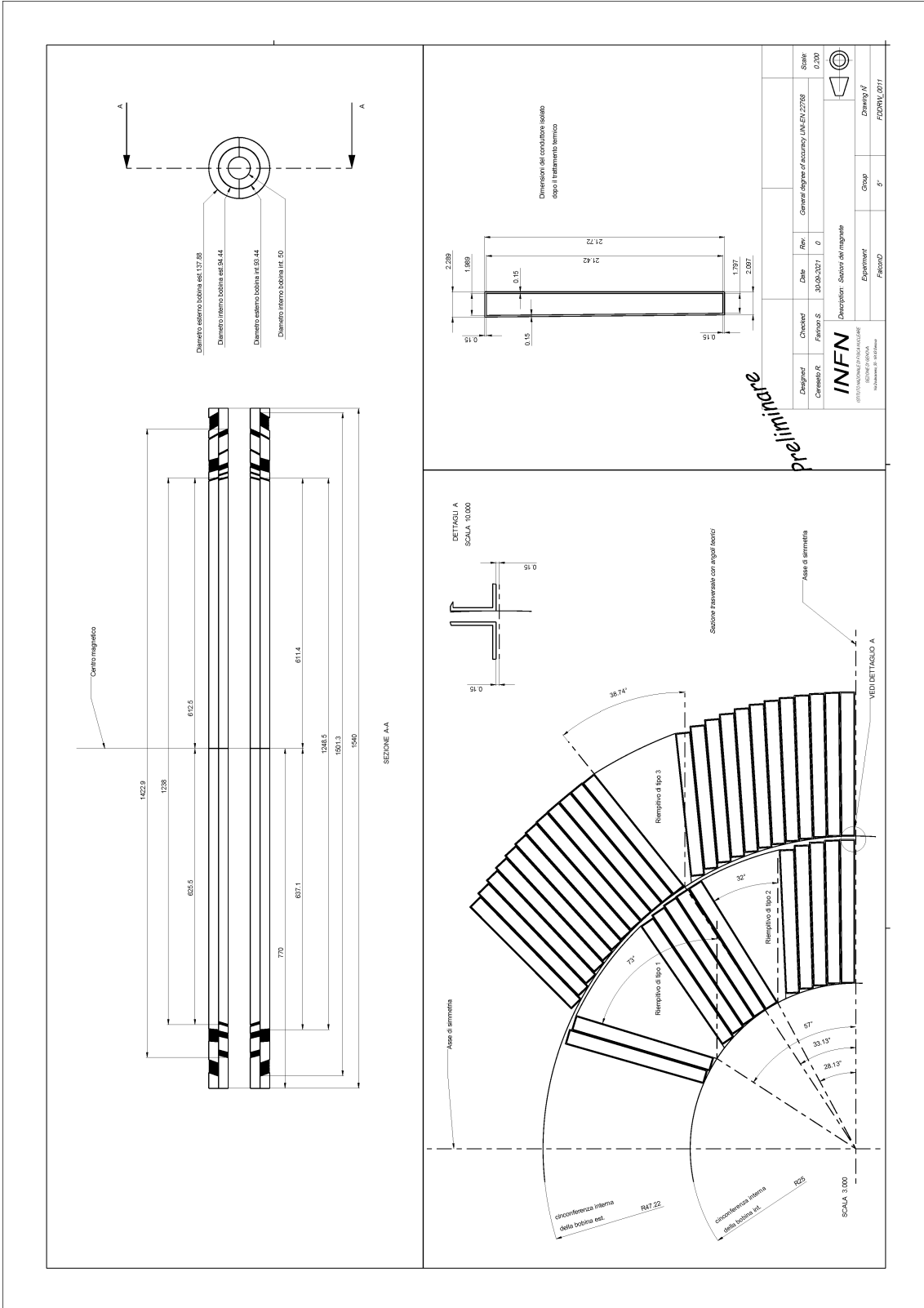


Figure 77: Coil overall dimensions.

## 6.2 End spacers

The end-spacer conceptual model is shown in Fig. 78. They are made of stainless steel AISI 316LN and will be machined according to the drawings that will be provided to the manufacturer.

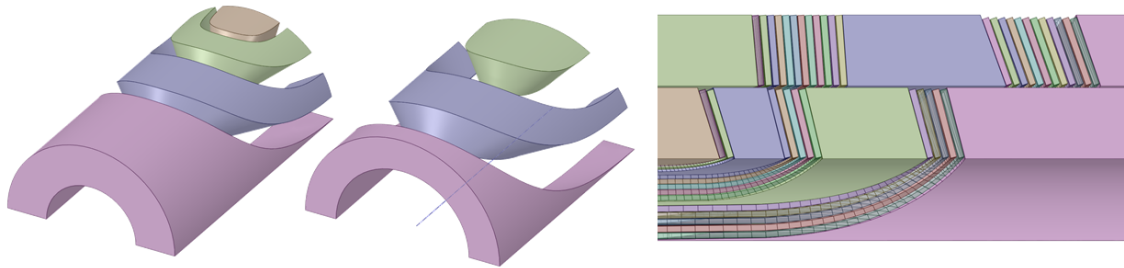


Figure 78: Conceptual design of the end spacers.

## 6.3 Winding

The winding must allow for a compact coil geometry without compromising the shape of the conductor. There shall be no internal splice, i.e., the same conductor length shall be used for both the inner and outer layers. The design of the winding mandrel shall allow transfer for the inner layer curing operation and then the outer layer. Thermal reaction requires that poles and wedges be in fairly short pieces with gaps between them so that no mechanical constraints arise during expansion/contraction. The gap distance may require iterative optimization. Inter-layer insulation is fabricated by placing several layers of S2 sheets with a defined amount of binder on a hollow tube and wrapping them with shrink foils to be cured in an oven up to a temperature of 160°C. The coils overall dimensions are shown in Figure 77.

## 6.4 Curing

Curing allows the geometry of the coil to be maintained during handling and consists of applying a ceramic binder (ceramic matrix CTD-1202-X) to be cured under pressure into a curing mold. The amount of binder per unit length shall be well defined.

## 6.5 Heat treatment

Reaction heat treatment (RHT) transforms the conductor into  $\text{Nb}_3\text{Sn}$ . Since  $\text{Nb}_3\text{Sn}$  occupies a larger volume than its precursors, it is common practice to design the cavity volume larger than the theoretical one. For FalconD, it was decided to adopt the cross-

section oversize of the MQXF quadrupoles, i.e., 4.5% in the azimuthal direction and 2% in the radial direction. An example of reaction cycle is shown in Fig. 2.

## **6.6 Impregnation**

Reacted coils must be vacuum impregnated. The resin used in all HL-LHC fabrications is CDT101K. Mold design must take into account the increased volume of the coils after heat treatment and the additional layers of S2 fiber. Quench heaters, if any, will not be impregnated.

## **6.7 Assembly of the mechanical structure**

The assembly procedure is described in detail in Section 5.1. The main components of the Bladder&Key system are pad, yoke lamination and outer shell.

### *6.7.1 Pad*

Pad (AISI 316LN) is made of two pieces as long as the coils which must never come into contact during magnet assembly, cooling and powering. It has four holes to accommodate longitudinal tie rods and special components (masters) will be designed to accommodate interference key and, temporarily, inflated bladders.

### *6.7.2 Yoke lamination*

The return yoke will be made of MAGNETIL steel along the magnetic length of the coil (1200 mm out of 1500 mm) and of AISI 316LN stainless steel on the coil ends. The steel will be laminated to a thickness of 5.8 mm, shaped as shown in 3. The yoke will consist of four symmetrical parts, with different design features aimed at meeting the construction requirements.

### *6.7.3 Outer shell*

The outer shell will be made of 7000 series aluminum alloy. Its purpose is to provide additional compression during cooling compared to the bladder&key system. No less than five cylinders will make up the outer shells, which will be fabricated in single pieces, without welding. Depending on the manufacturing technique, the total number of cylinders could be increased.

#### 6.7.4 Axial pre-loading system

The axial pre-loading system is described in details in Section 5.2. The assembly of coils, pads and yokes will be axially pre-loaded and held in position by two shaped plates in AISI 316LN on which four tie rods in the same material will be screwed. A system of grains acting on the ends of the coils, suitably instrumented with strain gauges, will ensure that the force applied on the screws is homogeneous.

### 7 MOCK-UP ACTIVITY

A mock-up activity has begun to verify the robustness and reliability of the mechanical bladder&key system. In particular the mock-up is intended to:

- consolidate the mechanical FE analysis to predict the magnet stress/strain conditions (straight part only) during the B&K assembly and cooling (at 77 K)
- study the influence of mechanical tolerances on the mechanical system
- determine the most convenient assembly sequence
- optimize the number and location of strain gauges to gather comprehensive information about the mechanical behavior of the system

The mock-up is a model 500 mm long of the central part of the FalconD magnet, as shown in Fig. 79. Compared to the conceptual design, several features have been added: 8 tie rods to assemble the iron laminations, 4 masters at the interface between pad and yoke to accommodate interference keys and, temporarily, inflated bladders, alignment pins between yoke and outer shells. The coils are represented by Al alloy simulacra. No insulation is present to avoid the presence of nonlinear behavior that could prevent interpretation of the results. The outer shell cylinders are 100 mm thick since for the mock-up it is planned to build them from 100 mm thick plates by spark erosion. Testing at liquid nitrogen temperature is also planned. The mock-up will be carefully instrumented by strain gauges, and Fuji paper testing is also planned.

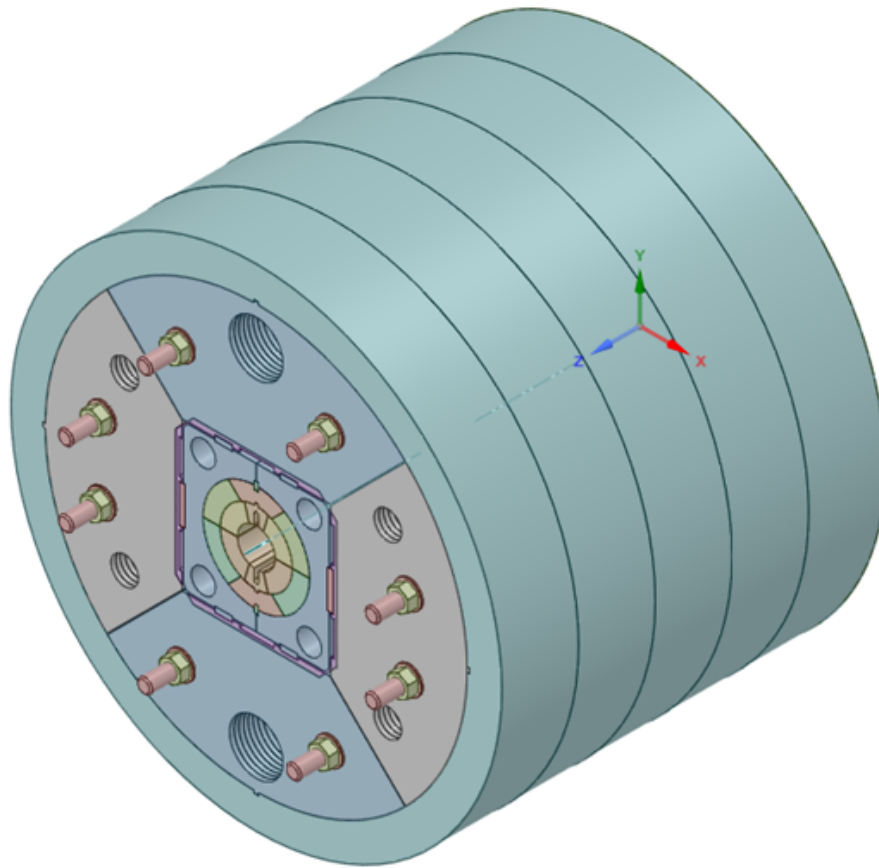


Figure 79: Design of the mock-up of the FalconD bladder&key mechanical system.

## 8 References

### References

- [1] FCC collaboration. "FCC Physics Opportunities: Future Circular Collider Conceptual Design Report Volume 1." *European Physical Journal C* 79.6 (2019): 474.
- [2] FCC collaboration. "FCC-ee: The Lepton Collider: Future Circular Collider Conceptual Design Report Volume 2." *European Physical Journal: Special Topics* 228.2 (2019): 261-623.
- [3] FCC collaboration. "FCC-hh: The Hadron Collider: Future Circular Collider Conceptual Design Report Volume 3." *European Physical Journal: Special Topics* 228.4 (2019): 755-1107.
- [4] FCC collaboration. "HE-LHC: The High-Energy Large Hadron Collider: Future Circular Collider Conceptual Design Report Volume 4." *European Physical Journal: Special Topics* 228.5 (2019): 1109-1382.
- [5] S. Hopkins, FCC Magnets Collaboration Meeting: Status of Conductor Procurement. [Online]. Available: <https://indico.cern.ch/event/860937/contributions/3668944/>, Accessed on Dec 2019.
- [6] Lackner, F., et al. "Analysis of temperature uniformity during heat treatment of Nb 3 Sn coils for the high-luminosity LHC superconducting magnets." *IEEE Transactions on Applied Superconductivity* 26.4 (2016): 1-5.
- [7] E. Todesco's Masterclass, Unit 7: Strand layouts, cable and insulation [Online]. Available: <https://indico.cern.ch/event/925559/>
- [8] E. Nilsson et al., "Design Optimization of the Nb<sub>3</sub>Sn 11 T Dipole for the High Luminosity LHC," in *IEEE Transactions on Applied Superconductivity*, vol. 27, no. 4, pp. 1-5, June 2017, Art no. 4001005, doi: 10.1109/TASC.2016.2635121.
- [9] S. Izquierdo Bermudez et al., "Second-Generation Coil Design of the Nb<sub>3</sub>Sn low- $\beta$  Quadrupole for the High Luminosity LHC," in *IEEE Transactions on Applied Superconductivity*, vol. 26, no. 4, pp. 1-5, June 2016, Art no. 4001105, doi: 10.1109/TASC.2016.2519002.
- [10] Bottura, Luca, and Arno Godeke. "Superconducting materials and conductors: fabrication and limiting parameters." *Reviews of accelerator science and technology* 5 (2012): 25-50.

- [11] Schoerling, Daniel, and Alexander V. Zlobin. Nb3Sn Accelerator Magnets: Designs, Technologies and Performance. Springer Nature, 2019.
- [12] S. Russenschuck, *ROXIE -A Computer Code for the Integrated Design of Accelerator Magnets*, CERN- LHC Project Report 276, 1999.
- [13] LHC ROXIE Magnets Repository. [Online]. Available: <https://roxie-lhc-magnets.web.cern.ch/roxie-LHC-magnets/HiLumi/DS11T/roxie.bhdata>
- [14] S. Caspi et al., The use of pressurized bladders for stress control of superconducting magnets, IEEE Trans. Appl. Supercond., vol. 11, no. 1, pp. 2272-2275, Mar. 2001.
- [15] S. Russenschuck, *ROXIE -A Computer Code for the Integrated Design of Accelerator Magnets*, CERN- LHC Project Report 276, 1999.
- [16] FEMM website. [Online]. Available: <http://www.femm.info/wiki/HomePage>
- [17] OPERA website. [Online]. Available: <https://www.3ds.com/products-services/simulia/products/opera>
- [18] Aleksa, Martin, Stephan Russenschuck, and Christine Vollinger. "Magnetic field calculations including the impact of persistent currents in superconducting filaments. IEEE transactions on magnetics 38.2 (2002): 825-828.
- [19] Ferracin, P., et al. "Modeling of random geometric errors in superconducting magnets with applications to the CERN Large Hadron Collider." Physical Review Special Topics-Accelerators and Beams 3.12 (2000): 122403.
- [20] Russenschuck, Stephan. Field computation for accelerator magnets: analytical and numerical methods for electromagnetic design and optimization. John Wiley & Sons, 2011.
- [21] M. Prioli et al., "The CLIQ Quench Protection System Applied to the 16 T FCC-hh Dipole Magnets," in IEEE Transactions on Applied Superconductivity, vol. 29, no. 8, pp. 1-9, Dec. 2019.
- [22] Ravaioli, E., et al. "Lumped-element dynamic electro-thermal model of a superconducting magnet." Cryogenics 80 (2016): 346-356.
- [23] NIST, National Institute of Standards and Technology, USA.

- [24] Rossi, Lucio, and Massimo Sorbi. "QLASA: A computer code for quench simulation in adiabatic multicoil superconducting windings." Nat. Inst. of Nucl. Phys.(INFN), Rome, Italy, Tech. Rep. TC-04-13 (2004).
- [25] Rossi, Lucio, and Massimo Sorbi. MATPRO: a computer library of material property at cryogenic temperature. No. CARE-NOTE-2005-018-HHH. 2005.
- [26] Marinozzi, V. "Guidelines for the quench analysis of Nb<sub>3</sub>Sn accelerator magnets using QLASA." Fermilab Tech. Div., Batavia, IL, USA, Tech. Rep. TD-13-008 (2013).
- [27] Manfreda, Giulio. "Review of ROXIEs material properties database for quench simulation." TE Technology department internal note 35 (2011).
- [28] Stenvall, Antti, and Valtteri Lahtinen. "Open Material Property Library With Native Simulation Tool IntegrationsMASTO." IEEE Transactions on Applied Superconductivity 28.3 (2018): 1-5.
- [29] J. Duvauchelle, B. Bordini, J. Fleiter and A. Ballarino, "Critical Current Measurements Under Transverse Pressure of a Nb<sub>3</sub>Sn Rutherford Cable Based on 1 mm RRP Wires," in IEEE Transactions on Applied Superconductivity, vol. 28, no. 4, pp. 1-5, June 2018, Art no. 4802305, doi: 10.1109/TASC.2018.2805158.
- [30] Gao, Peng. "Transverse pressure effect on superconducting Nb<sub>3</sub>Sn Rutherford and ReBCO Roebel cables for accelerator magnets." (2019), PhD Thesis, <https://doi.org/10.3990/1.9789402816587>.
- [31] P. Ferracin et al., "Fabrication and Test of a 3.7 m Long Support Structure for the LARP Nb<sub>3</sub>Sn Quadrupole Magnet LQS01," in IEEE Transactions on Applied Superconductivity, vol. 19, no. 3, pp. 1106-1111, June 2009, doi: 10.1109/TASC.2009.2019544.
- [32] P. Ferracin et al., "The HL-LHC Low- $\beta$  Quadrupole Magnet MQXF: From Short Models to Long Prototypes," in IEEE Transactions on Applied Superconductivity, vol. 29, no. 5, pp. 1-9, Aug. 2019, Art no. 4001309, doi: 10.1109/TASC.2019.2895908.
- [33] G. Willering et al., "Tests of the FRESCA2 100 mm Bore Nb<sub>3</sub>Sn Block-Coil Magnet to a Record Field of 14.6 T," in IEEE Transactions on Applied Superconductivity, vol. 29, no. 5, pp. 1-6, Aug. 2019, Art no. 4004906, doi: 10.1109/TASC.2019.2907280.

- [34] P. Ferracin et al., "Mechanical analysis of the Nb<sub>3</sub>Sn dipole magnet HD1," in IEEE Transactions on Applied Superconductivity, vol. 15, no. 2, pp. 1119-1122, June 2005, doi: 10.1109/TASC.2005.849508.
- [35] Data presented in EuroCirCol-P1-WP5, 24/06/2016  
*[https://fcc.web.cern.ch/eurocircol/\\_layouts/15/WopiFrame.aspx?sourcedoc=/eurocircol/Documents/WP5/Data%20Sets/EuroCirCol-P1-WP5-Note-160624.docx&action=default](https://fcc.web.cern.ch/eurocircol/_layouts/15/WopiFrame.aspx?sourcedoc=/eurocircol/Documents/WP5/Data%20Sets/EuroCirCol-P1-WP5-Note-160624.docx&action=default)*.
- [36] G. Vallone et al., "Magnetic and Mechanical Analysis of a Large Aperture 15T Cable Test Facility Dipole Magnet," in IEEE Transactions on Applied Superconductivity, vol. 31, no. 5, pp. 1-6, Aug. 2021, Art no. 9500406, doi: 10.1109/TASC.2021.3065882.
- [37] ANSYS website. [Online]. Available: <https://www.ansys.com/>